2

SAR Imaging using Coherent Modes of Diversity: SAR Polarimetry, Interferometry and Tomography

2.1. Introduction

Spectral and spatial diversity measurements, Synthetic Aperture Radar (SAR) imaging uses modes to focus 2D images of electromagnetic reflectivity of environments. Even though this information is very useful for detecting objects or to evaluate some of their geophysical properties, it has some limitations for further applications or characterizations. In fact, very diverse objects, such as a vehicle or a forest parcel, may provide responses with a similar energetic level. As a result their differentiation must necessarily involve additional information, among which polarization diversity is often considered. Classic SAR imaging uses a system of antennas polarized in the same way, and so measures 2D scalar information. The use of antennas with different polarizations allows the measurement, for each image pixel, of a multi-variate polarimetric quantity which provides information on the intrinsic geophysical properties of the imaged objects. Another significant limitation of SAR imaging comes from the natural ambiguity linked to the 2D mapping of 3D environments. This dimension reduction causes a direct loss of height related information because of height and, in particular, mixes the contributions from scatterers located at different altitudes. The solution usually considered uses additional spatial diversity to determine, for each 2D SAR image pixel, either the elevation position of the

Chapter written by Laurent FERRO-FAMIL and Eric POTTIER.

main scatterer, or the vertical distribution of the imaged reflectivity, for tomographic applications. It should be noted that SAR interferometry (InSAR) requires the coherent combination of $N = 2$ SAR measurements, compared with $N \geq 3$ for tomography and $2 \leq N \leq 4$ for polarimetric measurements. These different measurement modes, which can be combined with each other, are illustrated in Figure 2.1. The use of wave polarization or the measurement of an object's position through interferometry are widely known techniques used since the post-war period in the field of optics. During the 1950s and 1960s, a group of researchers [DES 51, KEN 49, SIN 48, SIN 50] developed the theoretical tools necessary to handle coherent multi-variate data, using wave polarization to differentiate radar obstacles or to identify them from their unique polarimetric behaviors. In the 1970s, Huyen [HUY 70] deeply modified the approach of polarimetric data processing by combining a rigorous mathematical analysis with a phenomenological interpretation of electromagnetic scattering mechanisms, paving the way for sophisticated techniques such as the ones presented in this chapter. SAR interferometry, which can determine the elevation position of the different SAR image pixels, appeared in the 1970s–1980s [GRA 74] with airborne applications [ZEB 86], and then satellite applications with SEASAT-A measurements [GOL 88]. The introduction of a nearly uninterrupted series of satellite missions adapted to the InSAR mode since the ERS-1 launch in 1991 has resulted in a boom in SAR interferometry techniques, which have now reached a nearly industrial level of maturity and which provide, through differential SAR interferometry [FER 01a, FER 07, MAS 93, ZEB 94], a technique with unique performances. SAR tomography was born at the beginning of the 2000s [REI 01] and has made it possible to image a scene in 3D by combining several inSAR images [FER 15, GIN 05, HUA 11a, NAN 09, TEB 10]. To date, its application is limited to airborne data, but adjustments are currently being studied to extend this approach to satellite measurements.

The information gain brought by the use of coherent diversity modes is shown in Figure 2.1.

This chapter first presents a detailed introduction to SAR polarimetry, its formalism, the mathematical tools that it uses, and the phenomenological interpretation of responses that it fosters. It is then shown that the generalization of speckle filtering in both multidimensional cases requires the use of the covariance matrix concept and that filtering, while it helps to significantly reduce the variance of the estimated values, results in a serious

limitation of the possible interpretations. Polarimetric decomposition techniques, which aim to differentiate and estimate one or several prevailing scattering are introduced as a mechanism. Examples of applications of these concepts to automatically classify scenes or to further scattering mechanisms are given. We discuss another diversity mode, SAR interferometry, or InSAR, based on the use of measurements made from slightly different positions, and which, through interferometry, uses the link between the phase variations observed in different measurements and the scene topography. After describing SAR data processing chain used to build digital elevation models (DEM), we present an introduction to 3D imaging of volumetric environments through SAR tomography, and some applications mixing space and polarization diversities.

a) b) c) d)

Figure 2.1. *Illustration of coherent diversity modes for data acquired in L-band by the DLR/ESAR sensor on the Oberpfaffenhofen site in Germany: a) SAR intensity at VV polarization, b) RGB=|HH-VV|, HV, |HH+VV|, c) interferometric coherence for the VV channel, d) color-coded images of optimal polarimetric interferometric coherences* ($RGB = |\gamma_{opt_1}|, |\gamma_{opt_2}|, |\gamma_{opt_3}|$*; defined in section 2.3)*

2.2. SAR polarimetry

2.2.1. *Introduction to radar polarimetry: formalism, descriptors and polarimetric operators*

2.2.1.1. *Wave polarization*

2.2.1.1.1. Polarization ellipse

We consider a progressive electromagnetic (EM) wave model, adapted to the representation of the electric field transmitted by a radar located at the center of a 3D coordinate system, taking the general form of a modulated quasi-spherical wave, whose expression is, in complex notations and in spherical coordinates, $\vec{E}(\boldsymbol{r},t) = u(t)\vec{E}_0(\theta,\phi)\frac{e^{j(\omega_c t-\kappa_c r)}}{r}$, with $\boldsymbol{r} = (r,\theta,\phi)$,

a position in space shown in Figure 2.2(a), f_c, the carrier frequency $\omega_c = 2\pi f_c = v_{Kc}$, and $\Im$, the wave propagation velocity. As discussed in Chapter 1 of this volume, the modulating signal $u(t)$ represents the base band waveform transmitted by the radar and has a spectrum, $U(f)$, which covers a spectral range with a bandwidth B_f. That signal may be directly defined in the time domain, as in the case of simple unmodulated pulses or chirp-like pulses linearly modulated in frequency, or generated in the spectral domain, like continuous wave signals, CW. For a non-dispersive environment, i.e. when the electrical, ϵ, and magnetic, μ, permittivities of the environment do not change on the covered spectral band, the propagation characteristics of that wave are identical to those of a monochromatic EM signal, and the transmitted signal is not distorted during the propagation. The angular dependence of $\vec{E}_0$, i.e. with respect to the θ and ϕ coordinates, represents the potentially anisotropic gain of the antenna that transmitted the electrical field. As was presented in Chapter 1, such a wave can be locally approximated by a plane wave, that is a wave propagating according to a direction orthogonal to a plane with a normal $\hat{\boldsymbol{\kappa}}$, and whose electrical field is given by $\vec{E}(\boldsymbol{r}, t) = \vec{E}_0 e^{j(\omega_c t - \kappa_c \hat{\boldsymbol{\kappa}}.\boldsymbol{r})}$, with $\vec{E}_0$ such as $\vec{E}_0.\hat{\boldsymbol{\kappa}} = 0$ and with components that vary according to the position $\boldsymbol{r}$ considered. That approximation is given by is illustrated in Figure 2.2, with a size D virtual object illuminated by a spherical wave at a r_0 distance from the transmitter, which is large compared to the size of the object. The spherical wave front can be locally approximated by a plane wave defined by the tangent plane to the r_0 radius sphere, and propagating in the direction orthogonal to that plane. The validity of that approximation, which considers that the field has constant amplitudes and phases on the tangent plane, around the central position of the object, is generally evaluated by means of an empirical criterion, called far-field criterion, given by $r_0 > \frac{2\,D^2}{\lambda_c}$, with $r_0, D \gg \lambda_c$, and D, the sphere radius including the measured object [KNO 74]. This criterion corresponds to an arbitrary phase walk error, $|\Delta\phi| = \frac{2\pi}{\lambda_c}\Delta d < \frac{\pi}{8}$, where Δd corresponds, as is shown in Figure 2.2(b), to the error term on the distance actually traveled by a spherical wave, during its approximation by a plane wave. When that criterion is verified, the object EM radiation can be approximated with high precision by its response to a plane wave. On Figure 2.2(c), it can be noted that the tangent plane definition varies with the position r to which the approximation is applied. The wave polarization is generally defined by means of a direct orthonormal coordinate system, $(\hat{\boldsymbol{x}}, \hat{\boldsymbol{y}}, \hat{\boldsymbol{z}})$, with, locally, $\hat{\boldsymbol{z}} = \hat{\boldsymbol{r}}$ and $\hat{\boldsymbol{x}} = \hat{\boldsymbol{\phi}}$.

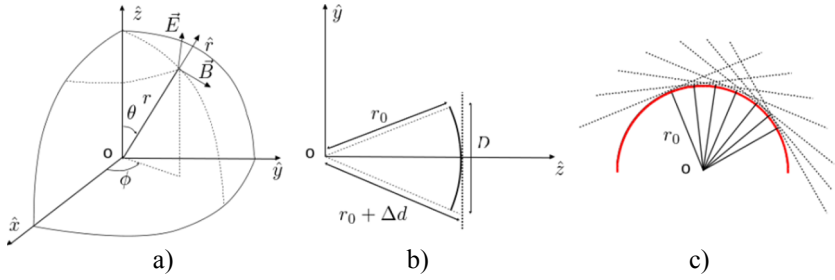

Figure 2.2. *a) Representation of the EM field of a spherical wave at the coordinates (r, θ, ϕ), b) local approximation of a spherical wave by a plane wave, c) decomposition of a spherical wave in a sum of plane waves*

The electrical field expression of a plane wave is then given, in complex, $\vec{E}(z,t)$, or real, $\vec{E}_{\mathcal{R}}(z,t)$, notation by:

$$\vec{E}(z,t) = \begin{bmatrix} E_x e^{j(\omega_c t - \kappa_c z + \alpha)} \\ E_y e^{j(\omega_c t - \kappa_c z + \alpha)} \\ 0 \end{bmatrix};$$
$$\vec{E}_{\mathcal{R}}(z,t) = \begin{bmatrix} E_{0_x} cos\,(\omega_c t - \kappa_c z + \delta_x + \xi) \\ E_{0_y} cos\,(\omega_c t - \kappa_c z + \delta_y + \xi) \\ 0 \end{bmatrix} \quad [2.1]$$

where $E_q = E_{0_q} e^{j\delta_q}$, $E_{0_q} \in \mathbb{R}$, and α represents an absolute phase shift that is dependent on the arbitrary position of the space–time coordinate system used. The plane wave polarization establishes the type of trajectory followed by its electrical field over time, or similarly, through space. Two examples of trajectories are described in Figure 2.3, which correspond to a horizontal, with $E_{0_y} = 0$, or circular, with $E_{0_x} = E_{0_y}$ and $|\delta_y - \delta_x| = \frac{\pi}{2}$, polarization. It should be noted that the components of $\vec{E}_{\mathcal{R}}(z,t)$ verify the equation of an ellipse, given by:

$$\left(\frac{E_{\mathcal{R}_x}(z,t)}{E_{0_x}}\right)^2 - 2\frac{E_{\mathcal{R}_x}(z,t)E_{\mathcal{R}_x}(z,t)}{E_{0_x}E_{0_y}} cos(\delta_y - \delta_x) + \left(\frac{E_{\mathcal{R}_y}(z,t)}{E_{0_y}}\right)^2 = \sin(\delta_y - \delta_x) \quad [2.2]$$

The evaluation of [2.2] at an arbitrary abscissa z_0 helps to assess the elliptical trajectory or polarization ellipse, followed by $\vec{E}_{\mathcal{R}}(z,t)$ in the plane orthogonal to the propagation axis, as shown in Figure 2.4(a). A polarization ellipse, and so the polarization of a plane wave, can be described by means

of three actual parameters represented in Figure 2.4(b) [KOS 86, LUE 95, LUE 96]:

– ellipse amplitude, $A = \sqrt{E_{0_x}^2 + E_{0_y}^2}$, which is fixed by the electrical field amplitude;

– ellipticity, τ, defined by $|sin\,2\,\tau| = 2\frac{E_{0x}E_{0y}}{E_{0x}^2+E_{0y}^2}\left|sin\left(\delta_y - \delta_x\right)\right|$, which sets the ellipse opening. When $\tau = 0$, the ellipse degenerates into a segment and the polarization is linear, whereas $|\tau| = \frac{\pi}{4}$ indicates a circular polarization. In a general case, $0 < \tau < \frac{\pi}{4}$, and the polarization is elliptic. The sign of τ is arbitrarily determined by the rotation direction of the field covering the ellipse over time, with $\tau \geq 0$ for a "left hand" polarization and $\tau \leq 0$ for a "right hand" polarisation. The ellipticity definition domain is then $\tau \in \left[-\frac{\pi}{4}, \frac{\pi}{4}\right]$;

– ellipse orientation calculated with respect to the axis $\hat{\boldsymbol{x}}$, ϕ, linked to the field components by $\tan 2\phi = 2\frac{E_{0x}E_{0y}}{E_{0x}^2+E_{0y}^2}\cos\left(\delta_y - \delta_x\right)$, with $\phi \in \left[-\frac{\pi}{2}, \frac{\pi}{2}\right]$.

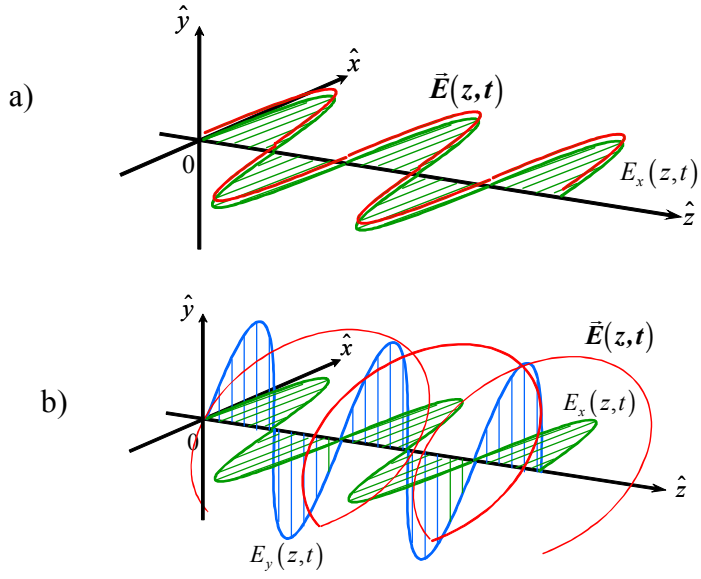

Figure 2.3. *Examples of spatial trajectories described by the electrical field of a wave with: a) horizontal, b) circular polarization*

The three types of polarization that can be encountered are:

– linear polarization, characterized by $\delta_y - \delta_x = 0 + k\,\pi \implies \tau = 0$ and by its orientation ϕ;

– circular polarization, with $\delta_y - \delta_x = \frac{\pi}{2} + k\,\pi, E_{0_x} = E_{0_y} \implies \tau = \pm\frac{\pi}{4}$;

– elliptical polarization, for which τ and ϕ take any values.

It should be noted that there are numerous other ways to configure the polarization ellipse. The angular variables presented here are widely used in radar or optical polarimetry due to their close link with the elementary transformations of a plane wave, which have an immediate physical interpretation.

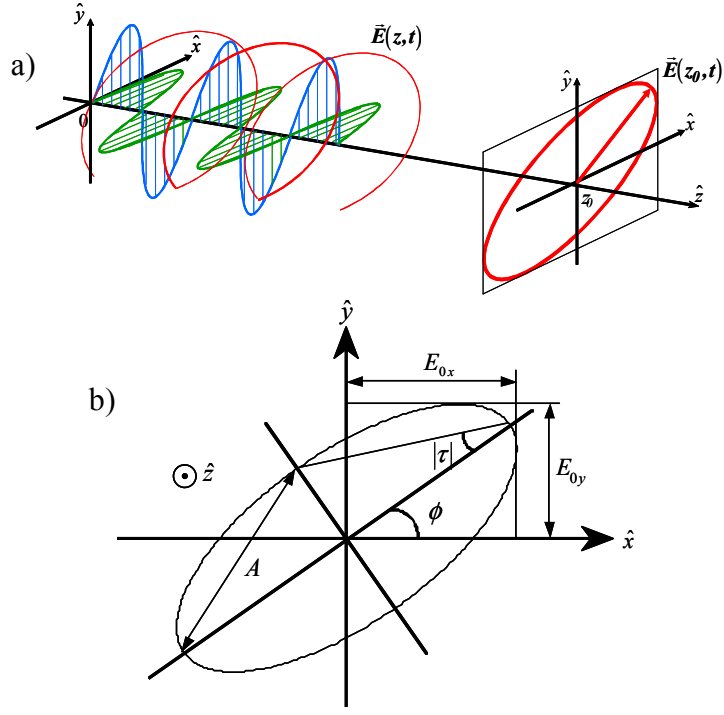

Figure 2.4. *a) elliptical trajectory described by the electrical field at the coordinate z_o, b) representation and configuration of the polarization ellipse*

2.2.1.1.2. Jones vector

Definitions and formalism SU(2)

The Jones vector, $\boldsymbol{E} \in \mathbb{C}^{2\times 1}$, is determined from the electrical field complex envelope as:

$$\mathbf{E} = \mathrm{e}^{j\alpha}\begin{bmatrix} E_{0_x}\mathrm{e}^{j\delta_x} \\ E_{0_y}\mathrm{e}^{j\delta_y} \end{bmatrix} = A\mathrm{e}^{j\xi}\frac{1}{\sqrt{1+|\rho|^2}}\begin{bmatrix} 1 \\ \rho \end{bmatrix} \text{ with } \rho = \frac{E_{0y}}{E_{0x}}\mathrm{e}^{j(\delta_y-\delta_x)} \qquad [2.3]$$

where ρ is the polarization ratio, which specifies a polarization state. A linear polarization is characterized by $\rho \in \mathbb{R}$, whereas for a circular polarization, $\rho = \pm j$. The Jones vector and the polarization ratio can also be derived from the polarization ellipse parameters as [KOS 86, LEE 08]:

$$\mathbf{E} = Ae^{j\alpha}\begin{bmatrix} cos\,\phi\,cos\,\tau - j\,sin\,\phi\,sin\,\tau \\ sin\,\phi\,cos\,\tau + j\,cos\,\phi\,sin\,\tau \end{bmatrix} \text{ and } \rho = \frac{tan\,\phi + j\,tan\,\tau}{1 - j\,tan\,\phi\,tan\,\tau} \qquad [2.4]$$

Jones vectors for the most commonly used polarization states are given in Table 2.1.

Polarization	Unit Jones vector	ϕ [rad]	τ [rad]
Horizontal (H)	$\boldsymbol{u}_h = \begin{bmatrix} 1 \\ 0 \end{bmatrix}$	0	0
Vertical (V)	$\boldsymbol{u}_v = \begin{bmatrix} 0 \\ 1 \end{bmatrix}$	$\frac{\pi}{2}$	0
Linear +45°	$\boldsymbol{u}_{+45} = \frac{1}{\sqrt{2}}\begin{bmatrix} 1 \\ 1 \end{bmatrix}$	$\frac{\pi}{4}$	0
Linear -45°	$\boldsymbol{u}_{-45} = \frac{1}{\sqrt{2}}\begin{bmatrix} 1 \\ -1 \end{bmatrix}$	$-\frac{\pi}{4}$	0
Left circular	$\boldsymbol{u}_l = \frac{1}{\sqrt{2}}\begin{bmatrix} 1 \\ j \end{bmatrix}$	$\left[-\frac{\pi}{2} \quad \cdots \quad \frac{\pi}{2}\right]$	$\frac{\pi}{4}$
Right circular	$\boldsymbol{u}_r = \frac{1}{\sqrt{2}}\begin{bmatrix} 1 \\ -j \end{bmatrix}$	$\left[-\frac{\pi}{2} \quad \cdots \quad \frac{\pi}{2}\right]$	$-\frac{\pi}{4}$

Table 2.1. *Parameters of commonly used polarization states*

The expression of [2.4] makes it possible to formulate a Jones vector by means of matrix operators derived from the special complex unit matrix

group (2×2) $SU(2)$ [CLO 86a, CLO 92, CLO 09], which is the basis for the modern polarimetric formalism:

$$\mathbf{E} = A\mathrm{e}^{j\alpha}\begin{bmatrix} cos\,\phi & -sin\,\phi \\ sin\,\phi & cos\,\phi \end{bmatrix}\begin{bmatrix} cos\,\tau \\ j\,sin\,\tau \end{bmatrix} = A\mathbf{U}_2(\phi)\mathbf{U}_2(\tau)\mathbf{U}_2(\alpha)\mathbf{x} \equiv \mathbf{U}_2(\phi,\tau,\alpha) \quad [2.5]$$

with $\boldsymbol{x} = \boldsymbol{u}_H = [1\ 0]^T$. A (2×2) matrix $\boldsymbol{U}_2 \in SU(2)$ verifies $\boldsymbol{U}_2\boldsymbol{U}_2^H = \boldsymbol{I}$ and $|\boldsymbol{U}_2| = +1$, with $\boldsymbol{I}$ the identity matrix, $\boldsymbol{U}_2^H = \boldsymbol{U}_2^{*T}$, the transpose and conjugate matrix $\boldsymbol{U}_2$, and $|\boldsymbol{U}_2|$ its determinant. The basis of $SU(2)$ adapted to the description of a Jones vector given by [2.4] and [2.5] is:

$$\mathbf{U}_2(\phi) = \begin{bmatrix} cos\,\phi & -sin\,\phi \\ sin\,\phi & cos\,\phi \end{bmatrix},\ \mathbf{U}_2(\tau) = \begin{bmatrix} cos\,\tau & j\,sin\,\tau \\ j\,sin\,\tau & cos\,\tau \end{bmatrix},$$
$$\mathbf{U}_2(\alpha) = \begin{bmatrix} \mathrm{e}^{+j\alpha} & 0 \\ 0 & \mathrm{e}^{-j\alpha} \end{bmatrix} \quad [2.6]$$

SU(2) matrices can be associated with rotations in complex spaces, and the expression of any Jones vector using the one associated with a horizontal polarization *x*, as shown in [2.5], has a highly physical interpretation: an arbitrary polarization wave can be considered as a horizontal polarization wave, phase shifted by an angle α, with a polarization ellipse open by an angle τ and orientated by an angle ϕ with respect to the horizontal.

Change of polarization basis

One of the main characteristics of radar polarimetry, linked to the multidimensional nature of polarization information, lies in the fact that the object response acquired in a polarization basis can be expressed in any basis by means of a simple mathematical transformation, that is without having to measure that response with a set of antennas with different polarization properties. A polarization orthonormal basis is composed of two unitary Jones vectors, $\boldsymbol{u}$ and $\boldsymbol{u}_\perp$, verifying $\boldsymbol{u}^H\boldsymbol{u}_\perp = 0$ and $\boldsymbol{u}^H\boldsymbol{u} = \boldsymbol{u}_\perp^H\boldsymbol{u}_\perp = 1$. These normalized orthogonality conditions do not allow us to uniquely determine $\boldsymbol{u}_\perp$ from $\boldsymbol{u}$. To address this indeterminacy, we then use the formalism $SU(2)$ to define a basis from the same transformation of the two elements of the reference polarization basis $(\boldsymbol{u}_h, \boldsymbol{u}_v)$:

$$\mathbf{u} = \mathbf{U}_2(\phi,\tau,\alpha)\mathbf{u}_\mathrm{h} \text{ and } \mathbf{u}_\perp = \mathbf{U}_2(\phi,\tau,\alpha)\mathbf{u}_v = \mathbf{U}_2(\phi_\perp,\tau_\perp,\alpha_\perp)\mathbf{u}_h \quad [2.7]$$

Thus, the two Jones vectors, defining a polarization orthogonal basis, can be associated with polarization ellipses with parameters verifying $\phi_\perp = \phi + \frac{\pi}{2}$, $\tau_\perp = -\tau$, $\alpha_\perp = -\alpha$. From the expression of a vector its coordinates in an arbitrary basis, $\boldsymbol{E}_{(\boldsymbol{a},\boldsymbol{a}_\perp)} = E_{\boldsymbol{a}}\boldsymbol{a} + E_{\boldsymbol{a}_\perp}\boldsymbol{a}_\perp$, and using [2.7], we can define of matrix operator associated with a change of polarization basis as:

$$\boldsymbol{E}_{(\boldsymbol{u},\boldsymbol{u}_\perp)} = \mathbf{U}_{2_{(\boldsymbol{u}_h,\boldsymbol{u}_v)\to(\mathbf{u},\boldsymbol{u}_\perp)}}\boldsymbol{E}_{(\boldsymbol{u}_h,\boldsymbol{u}_v)} = \mathbf{U}_2^{-1}(\phi,\tau,\alpha)\boldsymbol{E}_{(\boldsymbol{u}_h,\boldsymbol{u}_v)} \quad [2.8]$$

We can thus extend the principle of this change to any-two-orthonomal basis, $(\boldsymbol{a},\boldsymbol{a}_\perp)$ and $(\boldsymbol{b},\boldsymbol{b}_\perp)$, as $\boldsymbol{E}_{(\boldsymbol{b},\boldsymbol{b}_\perp)} = \boldsymbol{U}_{2_{(\boldsymbol{u}_H,\boldsymbol{u}_V)\to(\boldsymbol{b},\boldsymbol{b}_\perp)}}\boldsymbol{U}^{-1}_{2_{(\boldsymbol{u}_H,\boldsymbol{u}_V)\to(\boldsymbol{a},\boldsymbol{a}_\perp)}}\boldsymbol{E}_{(\boldsymbol{a},\boldsymbol{a}_\perp)}$ [LUE 95].

2.2.1.2. *Polarimetric radar response of an object*

2.2.1.2.1. Radar measurements with full polarimetric diversity

Receiving polarization diversity

The synoptic representation of a radar acquisition involving a diversity of received polarizations is given in Figure 2.5(a). An electrical field with a polarization state $\boldsymbol{E}_T \propto \boldsymbol{u}$ is transmitted, and the observed scene response is simultaneously measured by means of two receiving channels, corresponding to the two elements of the polarization basis $(\boldsymbol{u},\boldsymbol{u}_\perp)$, $\boldsymbol{E}_R = E_{(\boldsymbol{u},\boldsymbol{u})}\boldsymbol{u} + E_{(\boldsymbol{u}_\perp,\boldsymbol{u})}\boldsymbol{u}_\perp$, where $(\boldsymbol{u}_\perp,\boldsymbol{u})$ indicates an incident polarization colinear to $\boldsymbol{u}$ and a scattered polarization aligned with $\boldsymbol{u}_\perp$. The selection of a polarization state during the transmission and reception of signals is provided by the antenna system used. In comparison with a radar system operating over a single polarization channel, a radar having a diversity of polarization at the reception is either more complex and hence more costly, as two receiving channels are needed, or results into a reduction of performance with a single channel at the reception and a commutation between the two diversely polarized antennas. This option implies a doubling of the Pulse Repetition Frequency (PRF) system, defined as the inverse of the period at which radar signals are transmitted and measured. Most of the radar systems having a diversity of polarization use two receiving channels.

Full polarization diversity

While the use of a receiving polarimetric diversity helps to better characterize an environment response or to detect particular objects, that

type of measurement is limited by the use of a single transmitting polarization state. Thus, we can give the example of a vertical dipole, which is extremely difficult to detect with radars, transmitting horizontal polarized waves. A fully polarimetric radar measurement, requires the transmission of two signals over orthogonal polarization states.

$$\boldsymbol{E}_T \propto \mathbf{u} \rightarrow \mathbf{E}_{\mathrm{R}_\mathbf{u}} = E_{(\mathbf{u},\mathbf{u})}\mathbf{u} + E_{(\mathbf{u}_\perp,\mathbf{u})}\mathbf{u}_\perp \text{and}$$

$$\boldsymbol{E}_T \propto \boldsymbol{u}_\perp \rightarrow \mathbf{E}_{\mathrm{R}_{\mathbf{u}_\perp}} = E_{(\mathbf{u},\mathbf{u}_\perp)}\mathbf{u} + E_{(\mathbf{u}_\perp,\mathbf{u}_\perp)}\mathbf{u}_\perp \qquad [2.9]$$

The full polarimetric information is generally represented under the form of a polarimetric scattering matrix, $\boldsymbol{S} \in \mathbb{C}^{2\times 2}$, obtained from Jones vectors measured for orthogonal transmitted polarization states:

$$\mathbf{S} = \left[\mathbf{E}_{\mathrm{R}_\mathbf{u}}, \mathbf{E}_{\mathrm{R}_{\mathbf{u}_\perp}}\right] = \begin{bmatrix} E_{(\boldsymbol{u},\boldsymbol{u})} & E_{(\boldsymbol{u}_\perp,\boldsymbol{u})} \\ E_{(\boldsymbol{u},\boldsymbol{u}_\perp)} & E_{(\boldsymbol{u}_\perp,\boldsymbol{u}_\perp)} \end{bmatrix} \equiv \begin{bmatrix} S_{11} & S_{12} \\ S_{21} & S_{22} \end{bmatrix} \qquad [2.10]$$

The diagonal elements of the scattering matrix, measured for similar receiving and transmitting polarization states, are called co-polar elements, or co-pols, whereas the off-diagonal elements represent terms measured in cross-polarization, or cross-pol. As shown in Figure 2.5(b), a fully polarimetric information measurement requires a doubling of the transmitted information, and so of the PRF, which can result, as was shown in Chapter 1 of this volume, in an increase of the azimuth ambiguity phenomena and a significant decrease of the range swath.

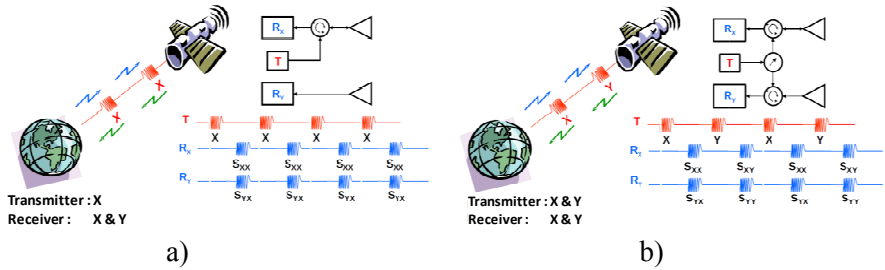

a) b)

Figure 2.5. *Synoptic representation of a radar measurement: a) with polarization diversity, b) with full polarization diversity*

2.2.1.2.2. Polarimetric scattering matrix and target vector

Polarimetric scattering matrix

From the expression of the scattering matrix given in [2.10] and the Jones vector decomposition on a polarization basis, we see that the polarimetric scattering matrix associated with an object measured in an arbitrary basis $(\boldsymbol{u}, \boldsymbol{u}_\perp)$ makes it possible to calculate the object response for an arbitrary polarization state, expressed in the basis $(\boldsymbol{u}, \boldsymbol{u}_\perp)$:

$$\mathbf{E}^s = \mathbf{S}\mathbf{E}^i = \begin{bmatrix} S_{11} & S_{12} \\ S_{21} & S_{22} \end{bmatrix} \mathbf{E}^i \qquad [2.11]$$

with $\boldsymbol{E}^i$, a Jones vector associated with an arbitrary polarization state. Thus, for a $\boldsymbol{S}$ matrix measured in the basis $(\boldsymbol{u}_h, \boldsymbol{u}_v)$, that is from two measurements for $\boldsymbol{E}^i = \boldsymbol{u}_h = \begin{bmatrix} 1 \\ 0 \end{bmatrix}$ and then $\boldsymbol{E}^i = \boldsymbol{u}_v = \begin{bmatrix} 0 \\ 1 \end{bmatrix}$, the object's response to a left circular polarization can be obtained, without any additional measurement, like $\boldsymbol{E}^s \propto \boldsymbol{S}\boldsymbol{u}_L$, or for a linear incident polarization orientated at $+45°$ like $\boldsymbol{E}^s \propto \boldsymbol{S}\boldsymbol{u}_{+45}$.

Back scatter alignment convention, reciprocity and relative scattering matrix

Two conventions for the representation of fully polarimetric information, based on the use of a Cartesian coordinate system and as a reference for defining the electrical field amplitudes and phases according to each axis, can be found in the literature. The *Forward Scatter Alignment* (FSA) convention, illustrated in Figure 2.6, is generally used in electromagnetism and considers a Cartesian coordinate system with an axis $\hat{z}$ aligned with the direction of propagation of the considered plane wave. During a monostatic measurement, that is when the radar transmitting and receiving systems are co-localized, the coordinate systems used to represent the transmitted and received signals have $\hat{z}$ axes orientated in opposite directions. The community of users of monostatic radar polarimetry generally prefers to use the *Back Scatter Alignment* (BSA) convention, which considers the same coordinate system to represent the transmitted and received waves. The scattering matrices expressed according to the FSA or BSA convention are linked by a diagonal transformation matrix, as shown in [2.12].

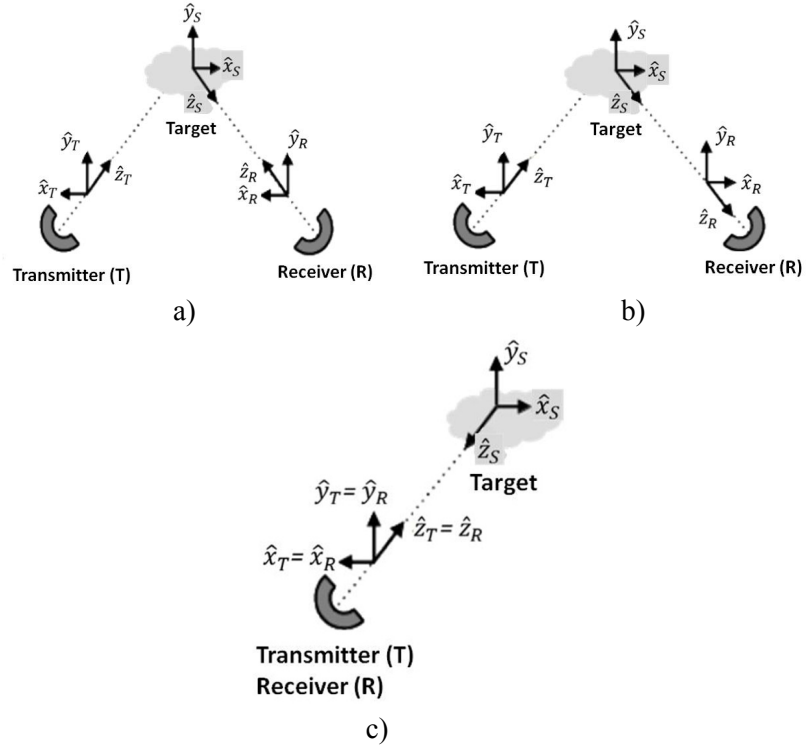

Figure 2.6. *Geometrical configurations of the representation conventions: a) general FSA, b) bi-static BSA, c) monostatic BSA*

As nearly all the environments measured by radars have a reciprocal EM behavior, that is to say that their response remains unchanged when the transmitting and receiving antennas are switched, we see that the scattering matrix, measured in a monostatic configuration and expressed according to the BSA convention, shows a symmetry property illustrated in [2.12] [CLO 09, LEE 08, LUE 95]:

$$\mathbf{S}_{BSA} = \begin{bmatrix} -1 & 0 \\ 0 & 1 \end{bmatrix} = \mathbf{S}_{FSA} \quad \mathbf{S}_{BSA} = \begin{bmatrix} S_{11} & S_{12} \\ S_{12} & S_{22} \end{bmatrix} = \boldsymbol{S}^{T}_{BSA} \qquad [2.12]$$

As shown in [2.13], the scattering matrix can be characterized, in a monostatic configuration, by three complex values or similarly by six real numbers. This structure can be slightly simplified by noting that the polarimetric properties, that is the polarization ellipse parameters and the

amplitude, associated with the scattered Jones vector, $\boldsymbol{E}^s$, remain invariant by multiplication by an arbitrary phase term, $e^{j\xi}$. We can therefore, without losing any polarimetric information or any amplitude modification of the scattered signal, use a relative scattering matrix, $\boldsymbol{S}_{rel}$, obtained through the factorization of an arbitrary phase term, as shown in the example below:

$$\mathbf{S} = \begin{bmatrix} S_{11} & S_{12} \\ S_{12} & S_{22} \end{bmatrix} = e^{j\phi_{11}}\mathbf{S}_{rel} \qquad [2.13]$$

$$\text{with } \boldsymbol{S}_{rel} = \begin{bmatrix} |S_{11}| & |S_{12}|e^{j(\phi_{12}-\phi_{11})} \\ |S_{12}|e^{j(\phi_{12}-\phi_{11})} & |S_{22}|e^{j(\phi_{22}-\phi_{11})} \end{bmatrix}$$

The scattering matrix and its relative version have the same trace value defined as $span(\boldsymbol{S}) = |S_{11}|^2 + 2|S_{12}|^2 + |S_{22}|^2$, which represents the total power of the wave scattered by a target for a unitary Jones vector incident wave. Figure 2.7 shows an example of SAR images acquired with a full polarization diversity on the site of the San Francisco Bay in L-band.

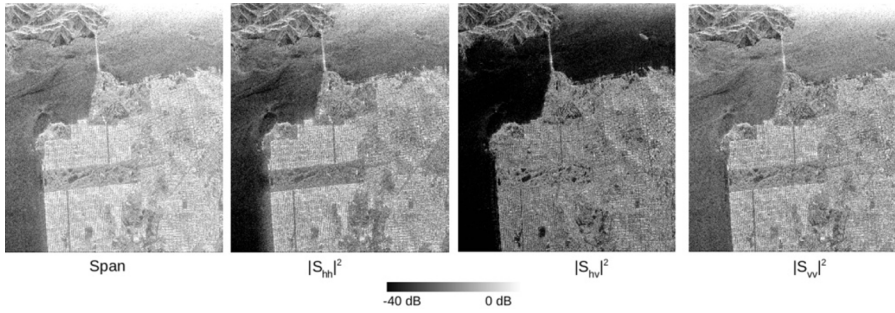

Figure 2.7. *Polarimetric images of the San Francisco Bay acquired in L-band by the JPL/AirSAR sensor*

Polarimetric target vector

If the scattering matrix contains, for a given configuration, all the polarimetric information of a target response, its representation under the form of a matrix (2×2) is not well adapted to the manipulations required by modern multi-dimensional signal processing. A formulation, called

target vector, whose two most used versions in practice are defined from the scattering matrix measured in the H–V basis, as [CLO 92, CLO 96]:

$$\mathbf{k} = \mathbf{k}_P = \frac{1}{\sqrt{2}}[S_{hh} + S_{vv} \quad S_{hh} - S_{vv} \quad 2\,S_{hv}]^T,$$
$$\mathbf{k}_L = \left[S_{hh} \quad \sqrt{2}S_{hv} \quad S_{vv}\right]^T \qquad [2.14]$$

The target vector $\boldsymbol{k}_L$ corresponds to the lexicographic sorting of the scattering matrix elements, whereas $\boldsymbol{k}_P$ results from a different linear combination, involving the matrix basis of the Pauli spinors. Those two target vectors are equivalent, as they are linked by a non-singular and unitary linear transformation, $\boldsymbol{k}_P = \boldsymbol{P}_{L\to P}\boldsymbol{k}_L$, so that $span(\boldsymbol{k}) = span(\boldsymbol{k}_L) = span(\boldsymbol{S})$, with here $span(\boldsymbol{x}) = \sum_i |x_i|^2$.

Change of polarimetric basis

We consider here a fully polarimetric acquisition carried out in the H–V basis, and the relationship [2.10] recalled here, $\boldsymbol{E}^s_{(\boldsymbol{u}_h,\boldsymbol{u}_v)} = \boldsymbol{S}_{(\boldsymbol{u}_h,\boldsymbol{u}_v)}\boldsymbol{E}^i_{(\boldsymbol{u}_h,\boldsymbol{u}_v)}$, that we wish to express in the basis $(\boldsymbol{u},\boldsymbol{u}_\perp)$, as $\boldsymbol{E}^s_{(\boldsymbol{u},\boldsymbol{u}_\perp)} = \boldsymbol{S}_{(\boldsymbol{u},\boldsymbol{u}_\perp)}\boldsymbol{E}^i_{(\boldsymbol{u},\boldsymbol{u}_\perp)}$. The expression of the Jones vector of the incident wave is, according to [2.8], $\boldsymbol{E}^i_{(\boldsymbol{u},\boldsymbol{u}_\perp)} = \boldsymbol{U}_{2_{(\boldsymbol{u}_h,\boldsymbol{u}_v)\to(\boldsymbol{u},\boldsymbol{u}_\perp)}}\boldsymbol{E}^i_{(\boldsymbol{u}_h,\boldsymbol{u}_v)}$, with $\boldsymbol{U}_{2_{(\boldsymbol{u}_h,\boldsymbol{u}_v)\to(\boldsymbol{u},\boldsymbol{u}_\perp)}} = \boldsymbol{U}_2^{-1}(\phi,\tau,\alpha)$, whose parameters are obtained by means of the expression of $\boldsymbol{u}$ in the $(\boldsymbol{u}_h,\boldsymbol{u}_v)$ basis. The application of the same reasoning for $\boldsymbol{E}^s_{(\boldsymbol{u},\boldsymbol{u}_\perp)}$ requires, because the incident wave and the scattered wave propagate in opposite directions, the application of a complex conjugate on the $SU(2)$ operator. By using the unitary matrix property, $\boldsymbol{U}_2\boldsymbol{U}_2^H = \boldsymbol{I}$, we can summarize the action of polarimetric basis change on the expression of the scattering matrix as:

$$\mathbf{S}_{(\mathbf{u},\mathbf{u}_\perp)} = \mathbf{U}^*_{2_{(\mathbf{u}_h,\mathbf{u}_v)\to(\boldsymbol{u},\boldsymbol{u}_\perp)}}\mathbf{S}_{(\mathbf{u}_h,\mathbf{u}_v)}\mathbf{U}^{-1}_{2_{(\mathbf{u}_h,\mathbf{u}_v)\to(\boldsymbol{u},\boldsymbol{u}_\perp)}} =$$
$$\boldsymbol{U}_2^T(\phi,\tau,\alpha)\mathbf{S}_{(\mathbf{u}_h,\mathbf{u}_v)}\mathbf{U}_2(\phi,\tau,\alpha) \qquad [2.15]$$

The transformation indicated in [2.15] is called consimilarity and can be extended to a change between any two polarization bases. The application of a basis change onto a target vector can easily be obtained from [2.15] and is expressed in the form of a special unitary (3×3) transformation:

$$\mathbf{k}_{(\mathbf{u},\mathbf{u}_\perp)} = \mathbf{U}_{3T}(2\phi,2\tau,2\alpha)\mathbf{k}_{(\mathbf{u}_h,\mathbf{u}_v)} \qquad [2.16]$$

where the $SU(3)$ matrix is formed from matrices with an action corresponding to the one of the different $SU(2)$ elements:

$$\boldsymbol{U}_{3T}(\phi) = \begin{bmatrix} 1 & 0 & 0 \\ 0 & cos\,2\phi & sin\,2\phi \\ 0 & -sin\,2\phi & cos\,2\phi \end{bmatrix}, \boldsymbol{U}_{3T}(\tau) = \begin{bmatrix} cos\,2\tau & 0 & j\,sin\,2\tau \\ 0 & 1 & 0 \\ j\,sin\,2\,\tau & 0 & cos\,2\tau \end{bmatrix}, \boldsymbol{U}_{3T}(\alpha) = \begin{bmatrix} cos\,2\alpha & j\,sin\,2\alpha & 0 \\ j\,sin\,2\alpha & cos\,2\alpha & 0 \\ 0 & 0 & 1 \end{bmatrix} \quad [2.17]$$

It may be noted here that, although the $SU(3)$ matrices detailed in [2.17] have an action similar to those of $SU(2)$ given in [2.6], there is no particular link between those two groups for numerous reasons [CLO 92, FER 00]. One of the consequences of the structure differences between $SU(2)$ and $SU(3)$ can be observed in [2.17] with an ambiguity brought by the factor 2 multiplying each angular variable.

2.2.1.2.3. Phenomenological interpretation

One of the main benefits of radar polarimetry lies in its capacity to discriminate and estimate some of the geophysical characteristics of environments through the analysis of scattering mechanisms. The values taken by polarimetric indicators, constructed from the elements of $\boldsymbol{S}$ or of $\boldsymbol{k}$, over simple targets, may be linked, through a phenomenological interpretation of canonical scattering mechanisms, to properties of the objects observed, like their shape, their orientation [HUY 70], etc.

Canonical scattering mechanisms

We consider here ideal metallic elementary targets illustrated in Figure 2.8, which are measured at a normal incidence and with a carrier frequency adapted to their size.

The simplified forms of the corresponding scattering matrices are summarized in Table 2.2.

We note in Table 2.2 that the fully polarimetric responses of the chosen targets may have specific forms or properties depending on the polarimetric basis used, which can be used to label a pixel of a polarimetric SAR image according to the canonical mechanism that is the closest to it. The studies carried out by [SIN 48, SIN 50, KEN 49, HUY 70], concern the interpretation of scattering mechanisms from $\boldsymbol{S}$ and define polarimetric

invariants or specific polarization states of a target in order to relate them with some of its physical characteristics. This type of approach can be very easily illustrated by means of the target vectors $\boldsymbol{k}$ and $\boldsymbol{k}_L$, which correspond to different linear combinations, so-called Pauli or lexicographic combinations, of the scattering matrix elements explained in [2.14]. Despite the fact that, as was shown before, those two vectorial representations, which match through a non-singular transformation, are strictly equivalent, $\boldsymbol{k}$ offers a more direct interpretation of the observed scattering mechanism nature, from the modulus of its elements. In fact, as can be noted in Table 2.2, canonical scattering mechanisms associated with a surface, characterized by a simple reflection of the wave, and those measured on a dihedral, leading to a double interaction between the wave and the target, only differ, in an extremely simplified configuration and for a null azimuthal orientation, by a phase shift between the copolar channels. Thus, for a wave–matter interaction of the simple reflection type, $|[\boldsymbol{k}]_1| \propto |S_{hh} + S_{vv}| \gg |[\boldsymbol{k}]_2|, |[\boldsymbol{k}]_3|$, for a double bounce $|[\boldsymbol{k}]_2| \propto |S_{hh} - S_{vv}| \gg |[\boldsymbol{k}]_1|, |[\boldsymbol{k}]_3|$ and for a scattering by orientated anisotropic particles, $|[\boldsymbol{k}]_3| \propto |S_{hv}| \neq 0$. This interpretation is illustrated in Figure 2.9. We note in Table 2.2 the influence of the azimutal orientation angle, ϕ, which can be estimated, in circular polarization, from phase terms.

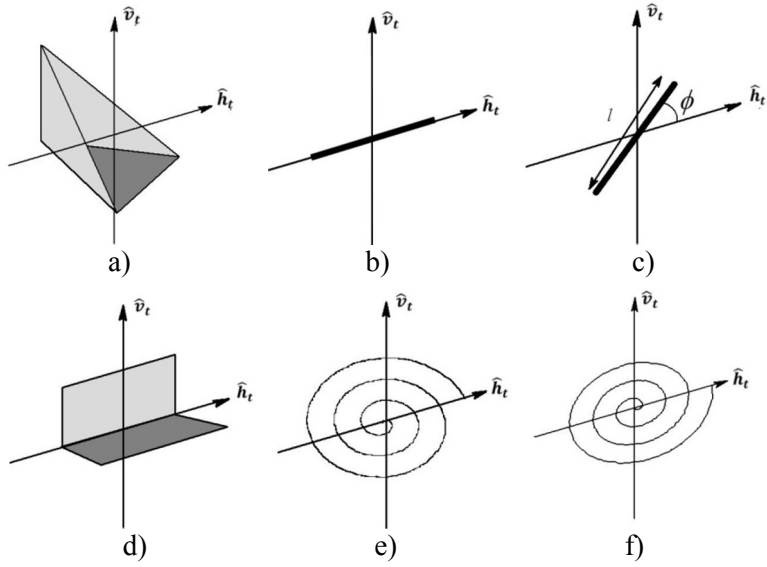

Figure 2.8. *Canonical targets: a) trihedral, b) horizontal dipole, c) orientated dipole, d) horizontal dihedral, e) left helix, f) right helix*

Target type	$\mathbf{S}_{(\mathbf{u}_h,\mathbf{u}_v)}$	$\mathbf{S}_{(\mathbf{u}_h,\mathbf{u}_v)}(\phi)$	$\mathbf{S}_{(\mathbf{u}_l,\mathbf{u}_{l_\perp})}(\phi)$
Sphere, plate, trihedral	$\mathbf{S}=\begin{bmatrix}1 & 0\\ 0 & 1\end{bmatrix}$	$\mathbf{S}=\begin{bmatrix}1 & 0\\ 0 & 1\end{bmatrix}$	$\mathbf{S}=\begin{bmatrix}0 & j\\ j & 0\end{bmatrix}$
Dipole	$\mathbf{S}=\begin{bmatrix}1 & 0\\ 0 & 0\end{bmatrix}$	$\mathbf{S}=\begin{bmatrix}cos^2\phi & \frac{1}{2}sin\,2\phi\\ \frac{1}{2}sin\,2\phi & sin^2\phi\end{bmatrix}$	$\mathbf{S}=\frac{1}{2}\begin{bmatrix}e^{j2\phi} & -j\\ -j & e^{-j2\phi}\end{bmatrix}$
Dihedral	$\mathbf{S}=\begin{bmatrix}1 & 0\\ 0 & -1\end{bmatrix}$	$\mathbf{S}=\begin{bmatrix}cos\,2\phi & sin\,2\phi\\ sin\,2\phi & -cos\,2\phi\end{bmatrix}$	$\mathbf{S}=\begin{bmatrix}e^{j2\phi} & 0\\ 0 & e^{-j2\phi}\end{bmatrix}$
Right helix	$\mathbf{S}=\frac{1}{2}\begin{bmatrix}1 & -j\\ -j & -1\end{bmatrix}$	$\mathbf{S}=\frac{e^{-j2\phi}}{2}\begin{bmatrix}1 & -j\\ -j & -1\end{bmatrix}$	$\mathbf{S}=\begin{bmatrix}0 & 0\\ 0 & -e^{-j2\phi}\end{bmatrix}$
Left helix	$\mathbf{S}=\frac{1}{2}\begin{bmatrix}1 & j\\ j & -1\end{bmatrix}$	$\mathbf{S}=\frac{e^{-j2\phi}}{2}\begin{bmatrix}1 & j\\ j & -1\end{bmatrix}$	$\mathbf{S}=\begin{bmatrix}e^{-j2\phi} & 0\\ 0 & 0\end{bmatrix}$

Table 2.2. *Scattering matrices of canonical targets, aligned with the horizontal, or oriented at an angle ϕ, in the H-V,$(\mathbf{u}_h,\mathbf{u}_v)$,and circular, $(\mathbf{u}_l,\mathbf{u}_{l_\perp})$ basis*

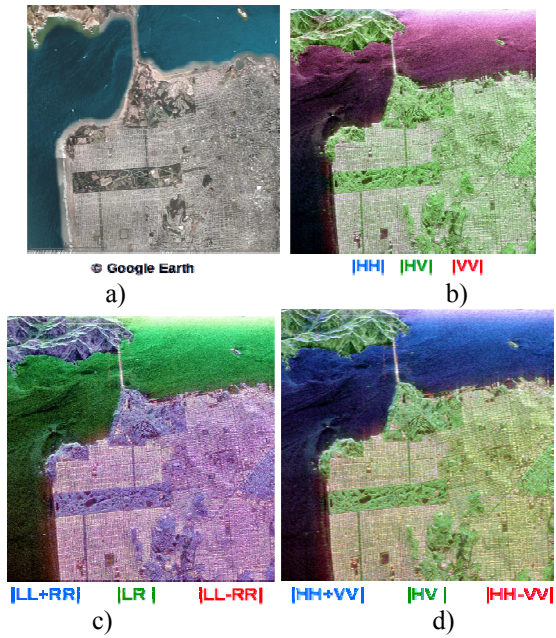

Figure 2.9. *a) Optical image of the San Francisco Bay. Polarimetric color-coded images from data acquired by the NASA/JPL/AirSAR sensor in L-band, in the b) lexicographic, c) circular, d) Pauli basis. For a color version of this figure, see www.iste.co.uk/baghdadi/2.zip*

2.2.2. *Characterization of the polarimetric response of environments: polarimetric decompositions*

2.2.2.1. *Polarimetric speckle filtering*

2.2.2.1.1. Multivariate speckle filtering using incoherent averaging: polarimetric covariance matrix

Statistics of polarimetric values

As laid out in Chapter 1 of this volume, SAR images are generally affected by the speckle effect due to the coherent integration of numerous independent contributions during the SAR imaging process, which gives them a random nature. Over homogeneous regions, this physical phenomenon can be modeled in the form of a product, $s(l) = \sqrt{I}\eta(l)$, where $s(l)$ is a realization of the SAR image, I represents the average intensity of the signal measured in the homogeneous region and $\eta(l)$ is a complex noise term, with independent real and imaginary parts, and which follows a centered Gaussian distribution with unit variance, $\eta \sim \mathcal{N}_{\mathbb{C}}(0,1)$. The significance of the speckle effect, that is the estimated reflectivity variance, can be particularly reduced by summing independent realizations of second order moments, selected in a more or less extended spatial neighborhood. If we consider a multivariate polarimetric measurement, $\boldsymbol{v} \in \mathbb{C}^q$, that can be assimilated in a Jones vector, $\boldsymbol{E}$ and $q = 2$, or to a target vector, $\boldsymbol{k}, \boldsymbol{k}_L$ and $q = 3$, then the marginal statistics, that is of a single channel v_i, or the joint statistics of the elements of the measured vector, are given, assuming a homogeneous region, by [GOO 76, LEE 94a]:

$$v_i \sim \mathcal{N}_{\mathbb{C}}(0, I_i),\ I_i = \mathrm{E}(|v_i|^2) \text{ and } \boldsymbol{v} \sim \mathcal{N}_{\mathbb{C}}(\boldsymbol{0}, \boldsymbol{\Sigma}) \text{ with } \boldsymbol{\Sigma} = \mathrm{E}(\boldsymbol{v}\boldsymbol{v}^H) \in \mathbb{C}^{q\times q} \quad [2.18]$$

where $[E(\boldsymbol{A})]_{ij} = E\left([\boldsymbol{A}]_{ij}\right)$, with $E(x)$, the expectation of the random variable x, and $\boldsymbol{\Sigma}$, the covariance matrix of $\boldsymbol{v}$, a centered random vector, with $[\boldsymbol{\Sigma}]_{ij} = E(v_i v_j^*)$. We generally represent the different types of polarimetric covariance matrix by means of specific names: $\boldsymbol{J} = E(\boldsymbol{E}\boldsymbol{E}^H)$ is called the wave coherence matrix, whereas $\boldsymbol{C} = E\left(\boldsymbol{k_L}\boldsymbol{k_L}^H\right)$ and $\boldsymbol{T} = E(\boldsymbol{k}\boldsymbol{k}^H)$ are, respectively, the covariance and coherence matrix. We can note here the arbitrary nature of these names, generated by the sometimes not so rigorous handling of signal processing tools and notions, given by the radar polarimetric community. In the remainder of this manuscript, we name each of those covariance matrix types by specifying the kind of vector that generated it.

Similarly, in case of scalar or single-channel SAR data, we consider the reduction of the speckle effect is obtained through the measurement of L independent realizations of a measured vector, $\{\boldsymbol{v}(l)\}_{l=1}^{L}$. The complex Gaussian distribution of a realization $\boldsymbol{v}(l)$ is given by:

$$f_{\boldsymbol{v}(l)}(\boldsymbol{v}(l)) = \frac{1}{\pi^q|\boldsymbol{\Sigma}|} e^{-\boldsymbol{v}^{\boldsymbol{H}}(l)\boldsymbol{\Sigma}^{-1}\boldsymbol{v}(l)} = \frac{1}{\pi^q|\boldsymbol{\Sigma}|} e^{-tr\left(\boldsymbol{\Sigma}^{-1}\boldsymbol{v}(l)\boldsymbol{v}^H(l)\right)} \quad [2.19]$$

with $\mathrm{tr}(\boldsymbol{A})$, the trace of $\boldsymbol{A}$. The joint law followed by the L realizations derived from the same distribution is then written:

$$f(\boldsymbol{v}(1), \cdots, \boldsymbol{v}(L)) = \prod_{l=1}^{L} f_{\boldsymbol{v}(l)}\left(\boldsymbol{v}(l)\right) = \frac{1}{\pi^{qL}|\boldsymbol{\Sigma}|^L} e^{-Ltr\left(\boldsymbol{\Sigma}^{-1}\widehat{\boldsymbol{\Sigma}}\right)} \quad [2.20]$$

with $\widehat{\boldsymbol{\Sigma}} = \frac{1}{\mathrm{L}}\sum_{\mathrm{l=1}}^{\mathrm{L}} \boldsymbol{v}(l)\boldsymbol{v}^{\mathrm{H}}(l)$

where $\widehat{\boldsymbol{\Sigma}}$, the L-view empirical covariance matrix, is also the optimal estimate in the sense of maximum likelihood (ML) of $\boldsymbol{\Sigma}$. By means of the variable change $\{\boldsymbol{v}(1), \cdots, \boldsymbol{v}(L)\} \rightarrow \widehat{\boldsymbol{\Sigma}} = \frac{1}{L}\sum_{l=1}^{L} \boldsymbol{v}(l)\boldsymbol{v}^H(l)$, may be obtained the Wishart law followed by $\widehat{\boldsymbol{\Sigma}}$:

$$f\left(\widehat{\boldsymbol{\Sigma}}\right) = \prod_{l=1}^{L} f_{\boldsymbol{v}(l)}\left(\boldsymbol{v}(l)\right) = \frac{L^{qL}\left|\widehat{\boldsymbol{\Sigma}}\right|^{L-q+1}}{\tilde{\Gamma}_{q-1}(L)|\boldsymbol{\Sigma}|^L} \mathrm{e}^{-L\mathrm{tr}\left(\boldsymbol{\Sigma}^{-1}\widehat{\boldsymbol{\Sigma}}\right)} \quad [2.21]$$

where $\tilde{\Gamma}_m(\alpha)$ represents the multivariate complex Gamma function [GOO 76, LEE 94a]. We notice here that the law, outlined in [2.21], is non-degenerated if $\left|\widehat{\boldsymbol{\Sigma}}\right| > 0$, which requires estimating $\widehat{\boldsymbol{\Sigma}}$ using a number $L \geq q$ of non-parallel samples $\boldsymbol{v}(l)$.

General properties of covariance matrices

Covariance matrices and their ML possess a hermitian symmetry $\boldsymbol{\Sigma} = \boldsymbol{\Sigma}^H$ and are semi-definite positive, $\boldsymbol{u}^H\boldsymbol{\Sigma}\boldsymbol{u} = E(|\boldsymbol{u}^H\boldsymbol{v}|^2) \geq 0, \forall \boldsymbol{u} \in \mathbb{C}^q$. From those two properties, we can deduce a general form of covariance matrices illustrated in the case $q = 3$ as:

$$\boldsymbol{\Sigma} = \begin{bmatrix} I_1 & I_{12} & I_{13} \\ I_{12}^* & I_2 & I_{23} \\ I_{13}^* & I_{23}^* & I_3 \end{bmatrix} = \begin{bmatrix} \sqrt{I_1} & 0 & 0 \\ 0 & \sqrt{I_2} & 0 \\ 0 & 0 & \sqrt{I_3} \end{bmatrix} \begin{bmatrix} 1 & \rho_{12} & \rho_{13} \\ \rho_{12}^* & 1 & \rho_{23} \\ \rho_{23}^* & \rho_{23}^* & 1 \end{bmatrix} \begin{bmatrix} \sqrt{I_1} & 0 & 0 \\ 0 & \sqrt{I_2} & 0 \\ 0 & 0 & \sqrt{I_3} \end{bmatrix} \quad [2.22]$$

where $I_i = E(|v_i|^2)$ represents the positive real intensity of the i^{th} polarization channel, and $I_{ij} = \mathrm{E}(v_i v_j^*)$, with $i \neq j$, is a complex cross-correlation term. The quantities $\rho_{ij} = \frac{I_{ij}}{\sqrt{I_i I_j}}$ are normalized correlation coefficients, whose modulus $|\rho_{ij}| \leq 1$ indicates the correlation level between the channels i and j, and whose argument gives information on the average phase shift between those two channels. The condition for the matrix to be defined as positive implies, in addition to the fact that $|\rho_{ij}| \leq 1$, cross-correlation conditions that can be intuitively illustrated as follows: if channels 1, 2 and 1, 3 are very correlated, that is $|\rho_{12}|, |\rho_{13}| \approx 1$, then channels 2, 3 cannot be uncorrelated, $|\rho_{23}| \not\approx 0$. We can see in [2.22] that a complex covariance matrix (3×3) can be completely defined by means of three real intensities and three complex intercorrelation coefficients, i.e. a set of nine real parameters. A general complex covariance matrix $(q \times q)$ can be parametered by means of q^2 real coefficients. In addition, we can characterize a covariance matrix through its decomposition into eigen-elements, which takes the following specific form:

$$\boldsymbol{\Sigma} = \mathbf{U}\boldsymbol{\Lambda}\boldsymbol{U}^H, \text{ with } \mathbf{U} = \left[\mathbf{u}_1, .., \mathbf{u}_\mathrm{q}\right] \text{ and } \boldsymbol{\Lambda} = \mathrm{diag}([\lambda_1, ..., \lambda_q]) \qquad [2.23]$$

where the operator diag() is such that $[\boldsymbol{\Lambda}]_{ij} = \lambda_i \delta_{i-j}$, and where we arbitrarily fix without losing generality, $\boldsymbol{u}_i^H \boldsymbol{u}_i = 1$ and $\lambda_i \geq \lambda_{i+1}$. The eigenvalues of the covariance matrix, λ_i, are the solutions of $|\boldsymbol{\Sigma} - \lambda_i \boldsymbol{I}| = 0$, and verify $tr(\boldsymbol{\Sigma}) = \sum_{i=1}^{q} \lambda_i$ and $|\boldsymbol{\Sigma}| = \prod_{i=1}^{q} \lambda_i$, whereas the eigenvectors remain unchanged by the linear transformation $\boldsymbol{\Sigma}$, in other words, $\boldsymbol{\Sigma}\boldsymbol{u}_i = \lambda_i \boldsymbol{u}_i$. It can be demonstrated that $\boldsymbol{U} \in SU(q)$, i.e. the eigenvectors of the covariance matrix are orthogonal to each other, $\boldsymbol{u}_i^H \boldsymbol{u}_j = \delta_{i-j}$, and that the eigenvalues of Σ are positive real, $\lambda_i \geq 0$. The set of eigenvectors defines a vectorial space, from which we can write a covariance matrix may be expressed by using q real coefficients, that are the eigenvalues, as:

$$\boldsymbol{\Sigma} = \mathrm{E}(\boldsymbol{v}\boldsymbol{v}^H) = \mathbf{U}\boldsymbol{\Lambda}\boldsymbol{U}^H = \sum_{i=1}^{q} \lambda_i \boldsymbol{u}_i \boldsymbol{u}_i^H \qquad [2.24]$$

The convention used to sort the eigenvalues, $\lambda_i \geq \lambda_{i+1}$, implies another interesting relationship:

$$\boldsymbol{u}_i = argmax_{\boldsymbol{u}_i^H \boldsymbol{u}_j = 0, j<i} \boldsymbol{u}^H \boldsymbol{\Sigma} \boldsymbol{u}, \lambda_\mathrm{i} = \boldsymbol{u}_i^H \boldsymbol{\Sigma} \mathbf{u}_i = E\left(\left|\mathbf{u}_\mathrm{i}^\mathrm{H} \mathbf{v}\right|^2\right) \qquad [2.25]$$

The expressions [2.24] and [2.25] are crucial for the interpretation of polarimetric data from their second order moment. The eigenvectors of a covariance matrix are homogeneous to data vectors, $\boldsymbol{v}$, that is to Jones or target vectors in the polarimetric case, for which they define a representation space which is not unique, but complete, i.e. any vector $\boldsymbol{v} \in \mathbb{C}^q$ can be written as $\boldsymbol{v} = \sum_{i=1}^{q} s_i \boldsymbol{u}_i$. The eigenvalue λ_i associated with an eigenvector $\boldsymbol{u}_i$ corresponds to the variance of the projection, $s_i = \boldsymbol{u}_i^H \boldsymbol{v}$, of the measured vectors, $\boldsymbol{v}$, on that eigenvector, and is of similar intensity, with $\lambda_i = E(|s_i|^2)$. An eigenvalue indicates that the measured vectors are very highly aligned with the concerned eigenvector, in other words: $\lambda_i = E\left(\left|\boldsymbol{u}_i^H \boldsymbol{v}\right|^2\right) \approx E(\boldsymbol{v}^H \boldsymbol{v})$. On the contrary, a low eigenvalue reflects the fact that the pointed direction, in a complex q-dimensional space, is represented very little in the measured data, that is $\left(\left|\boldsymbol{u}_i^H \boldsymbol{v}\right|^2\right) \approx 0$. We notice here a significant property of the decomposition into eigen-elements, widely used in polarimetry, which can be written as:

$$\mathbf{v} = \sum_{i=1}^{q} s_i \boldsymbol{u}_i \text{ et } \lambda_\mathrm{i} = E\left(\left|\mathbf{u}_\mathrm{i}^\mathrm{H} \boldsymbol{v}\right|^2\right) = E(|s_i|^2) \Rightarrow$$

$$\sum_{i=1}^{q} \lambda_i = E\left(\boldsymbol{v}^\mathrm{H} \boldsymbol{v}\right) = \mathrm{E}(\mathrm{span}(\boldsymbol{v})) \qquad [2.26]$$

where the span is taken according to its polarimetric definition, as the sum of the intensities received on each of the polarization channels. These various principles can be illustrated by means of an example using a reduced anthropometric vector data $\boldsymbol{m} = [w\ h]^T$, where w represents the mass of an individual and h its size. The covariance matrix of $\boldsymbol{m}$ is given by:

$$\mathbf{C} = \mathrm{E}(\boldsymbol{m}_c \mathbf{m}_c^T) = \begin{bmatrix} \sigma_w^2 & \sigma_w \sigma_h \rho_{wh} \\ \sigma_w \sigma_h \rho_{wh} & \sigma_h^2 \end{bmatrix} = [\boldsymbol{u}_1 \boldsymbol{u}_2] \begin{bmatrix} \lambda_1 & 0 \\ 0 & \lambda_2 \end{bmatrix} \begin{bmatrix} \boldsymbol{u}_1^T \\ \boldsymbol{u}_2^T \end{bmatrix} \qquad [2.27]$$

where $\boldsymbol{m}_c = \boldsymbol{m} - E(\boldsymbol{m})$, σ_x represents the standard deviation of x on the observed population and ρ_{wh} is the correlation coefficient between the height and mass of the individuals. Figure 2.10 offers a graphic interpretation in the case of a Gaussian statistic by representing the region for which $\boldsymbol{m}_c^T \boldsymbol{C}^{-1} \boldsymbol{m}_c \leq 1$.

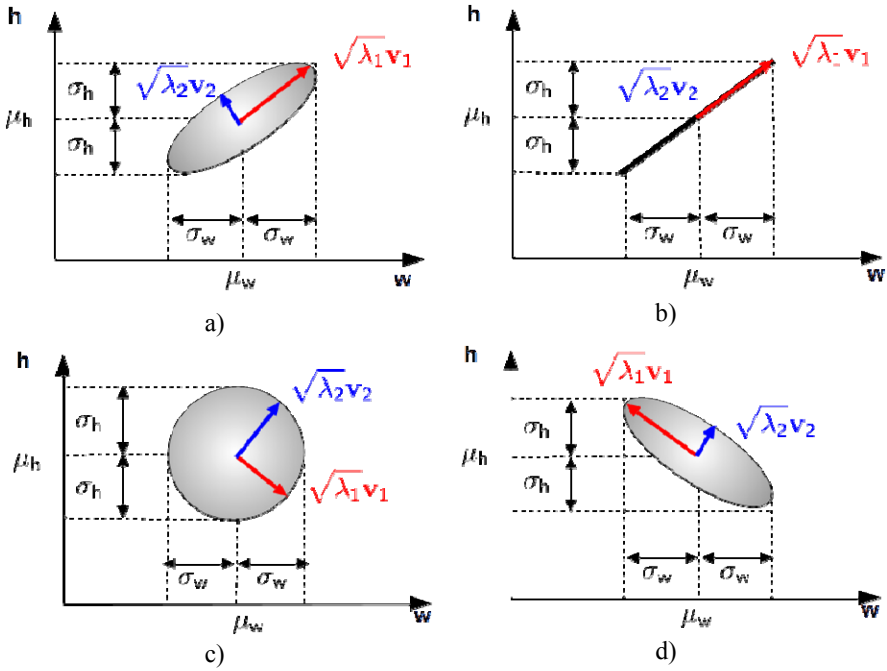

Figure 2.10. *Illustration of the joint distribution of the size, h, and the mass, w, of elements of a population, for unchanged marginal statistics. Population of the a) "normal", b) "clone", c) "anarchic", d) "unusual" type*

We note that if σ_w and σ_h indicate the extent of the data projection on the axes w and h respectively, the eigenvectors correspond to the axes of the ellipse described by the distribution, and the eigenvalues vary with the ellipse extent according to the specific direction considered. Four types of populations are represented and have similar marginal dispersions, $\sigma_{h,w}$. The "normal" population possesses a preferred direction in the measurement space, with relatively correlated sizes and masses, with $\rho_{wh} = 0.8$ and $\lambda_2 = \frac{\lambda_1}{5}$. The "clone" labeled population has a noticeable characteristic: even though they are randomly distributed, the size and mass of the individuals of that population are perfectly correlated, $\rho_{wh} = 1$ and $\lambda_2 = 0$, in other words, knowing one of the two values allows to determine the second without error. For the third population, qualified as "anarchic", knowing the size of an individual only gives very vague information on its mass. In that case, $\rho_{wh} = 0$ and $\lambda_2 = \lambda_1$, and the selection of a set of eigenvectors is arbitrary.

The last case offers an "unusual" population, which does show a preferred direction, but has a correlation coefficient with a negative sign resulting from the direction taken by $\boldsymbol{u}_1$, $\rho_{wh} = -0.8$, $\lambda_2 = \frac{\lambda_1}{5}$, which indicates that the tallest individuals are those with the lowest mass.

Properties of polarimetric covariance matrices

The most used fully polarimetric data covariance matrices are defined as:

$$\mathbf{T} = \mathrm{E}(\mathbf{k}\boldsymbol{k}^H) \text{ and } \mathbf{C} = \mathrm{E}(\boldsymbol{k}_L\mathbf{k}_L^H), \text{ with } \mathbf{T} = \mathbf{P}_{\mathrm{L}\to\mathrm{P}}\mathbf{C}\mathbf{P}_{\mathrm{L}\to\mathrm{P}}^{\mathrm{H}} \quad [2.28]$$

where $\boldsymbol{T}$ is the coherency matrix and $\boldsymbol{C}$ the covariance matrix. We notice that those two representations of second order statistics share the same eigenvalues, as their eigenvector's matrices are linked by the unitary transformation $\boldsymbol{P}_{L\to P}$, and that:

$$\mathrm{tr}(\mathbf{T}) = \mathrm{tr}(\mathbf{C}) = \mathrm{E}(\mathrm{span}(\mathbf{k})) \quad [2.29]$$

The developed and parameterized expressions of those matrices are given by:

$$\begin{aligned}\mathbf{T} &= \frac{1}{2}\mathrm{E}\left(\begin{bmatrix} |S_{hh}+S_{vv}|^2 & (S_{hh}+S_{vv})(S_{hh}-S_{vv})^* & 2(S_{hh}+S_{vv})S_{hv}^* \\ (S_{hh}-S_{vv})(S_{hh}+S_{vv})^* & |S_{hh}-S_{vv}|^2 & 2(S_{hh}-S_{vv})S_{hv}^* \\ 2S_{hv}(S_{hh}+S_{vv}) & 2S_{hv}(S_{hh}-S_{vv}) & 4|S_{hv}|^2 \end{bmatrix}\right) \\ &= \begin{bmatrix} 2\mathrm{A}_0 & \mathrm{C}-\mathrm{jD} & \mathrm{G}-\mathrm{jH} \\ \mathrm{C}+\mathrm{jD} & \mathrm{B}_0-\mathrm{B} & \mathrm{E}+\mathrm{jF} \\ \mathrm{G}+\mathrm{jH} & \mathrm{E}-\mathrm{jF} & \mathrm{B}_0+\mathrm{B} \end{bmatrix}\end{aligned} \quad [2.30]$$

where $A_0, B_0, B, C, D, E, F, G, H \in \mathbb{R}$, are the nine Huynen parameters [HUY 70, LEE 08], which completely describe a fully polarimetric covariance matrix in its most general form, and to which were linked some physical parameters of targets and environments by studies conducted by Huynen [HUY 70].

$$\begin{aligned}\mathbf{C} &= \mathrm{E}\left(\begin{bmatrix} |S_{hh}|^2 & \sqrt{2}S_{hh}S_{hv}^* & S_{hh}S_{vv}^* \\ \sqrt{2}S_{hv}S_{hh}^* & 2|S_{hv}|^2 & \sqrt{2}S_{hv}S_{vv}^* \\ S_{vv}S_{hh}^* & \sqrt{2}S_{vv}S_{hv}^* & |S_{vv}|^2 \end{bmatrix}\right) \\ &= \sigma\begin{bmatrix} 1 & \beta\sqrt{\delta} & \rho\sqrt{\gamma} \\ \beta^*\sqrt{\delta} & \delta & \epsilon\sqrt{\gamma\delta} \\ \rho^*\sqrt{\gamma} & \epsilon^*\sqrt{\gamma\delta} & \gamma \end{bmatrix}\end{aligned} \quad [2.31]$$

with $\sigma, \delta, \gamma \in \mathbb{R}$ and $\beta, \rho, \epsilon \in \mathbb{C}$.

By applying a basis change to the target vectors used to form a covariance matrix, $\boldsymbol{k}_{(\boldsymbol{u},\boldsymbol{u}_\perp)} = \boldsymbol{U}_{3T}(2\phi, 2\tau, 2\alpha)\boldsymbol{k}_{(\boldsymbol{u}_h,\boldsymbol{u}_v)}$, we can express $\boldsymbol{T}$ or $\boldsymbol{C}$ in any polarization basis such as:

$$\mathbf{T}_{(\mathbf{u},\mathbf{u}_\perp)} = \mathrm{E}\left(\boldsymbol{k}_{(\boldsymbol{u},\boldsymbol{u}_\perp)}\boldsymbol{k}^H_{(\boldsymbol{u},\boldsymbol{u}_\perp)}\right) = \mathbf{U}_{3T}(2\phi, 2\tau, 2\alpha)\mathbf{T}_{(\mathbf{u}_h,\mathbf{u}_v)}\boldsymbol{U}^H_{3T}(2\phi, 2\tau, 2\alpha) \quad [2.32]$$

The polarimetric second order representations verify the general properties of covariance matrices: in particular with a "dimension" of $q^2 = 9$, the statistics outlined in [2.20] and [2.21], as well as the interpretation of their decomposition into eigen-elements. Polarimetric data covariance matrices measured for environments showing some symmetry properties, illustrated in Figure 2.11, assume specific structures [NGH 92, YUE 94]:

– reflection symmetry: an environment, composed of symmetrically distributed reflectors on either side of the radar incidence plane, has a polarmetric response with reflection symmetry, which is characterized by a decorrelation of co- and cross-polar channels, i.e. $E(S_{hh}S^*_{hv}) = E(S_{vv}S^*_{hv}) = 0$. This type of response is characteristic of horizontal natural environments and has a coherency matrix with the following form:

$$\mathbf{T} = \begin{bmatrix} a & b & 0 \\ b^* & c & 0 \\ 0 & 0 & d \end{bmatrix} \quad [2.33]$$

– rotation symmetry: an environment rotation symmetry environment has a covariance matrix that remains rotationally invariant around the radar line of sight axis, that is $\boldsymbol{T} = \boldsymbol{U}_{3T}(2\phi)\boldsymbol{T}\boldsymbol{U}^{-1}_{3T}(2\phi)$:

$$\mathbf{T} = \begin{bmatrix} a & 0 & 0 \\ 0 & b & jc \\ 0 & jc & b \end{bmatrix} \text{ with } c \in \mathbb{R} \quad [2.34]$$

– azimuthal symmetry: the environment has both reflection and rotation symmetry properties. This type of response is specific to dense volumetric environments and has a covariance matrix given by:

$$\mathbf{T} = \begin{bmatrix} a & 0 & 0 \\ 0 & b & 0 \\ 0 & 0 & b \end{bmatrix} \quad [2.35]$$

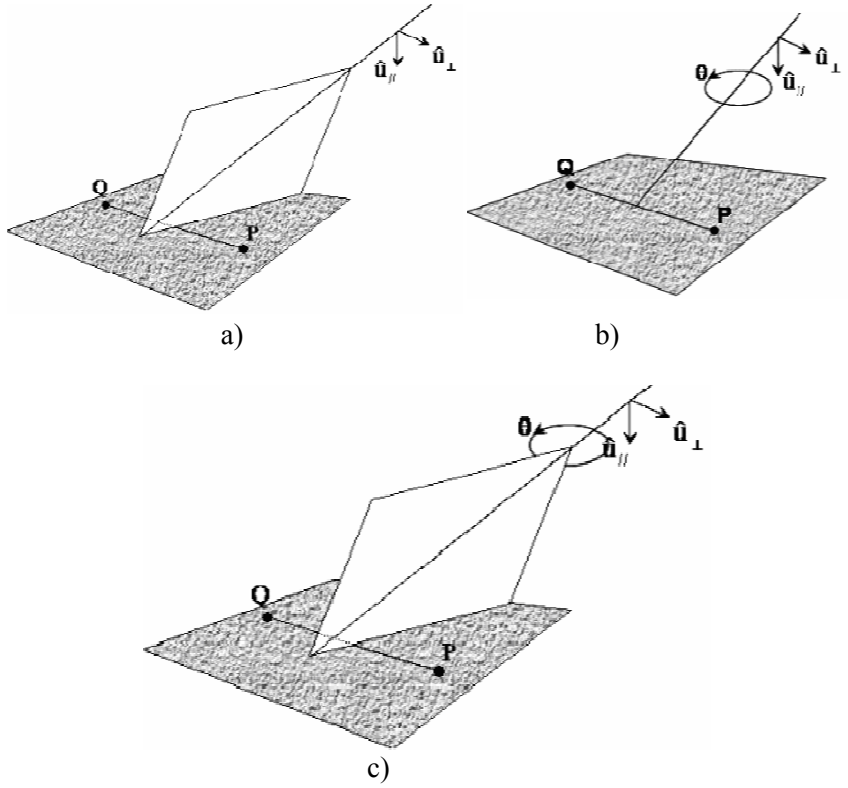

Figure 2.11. *Geometrical configuration of an environment whose response has a: a) reflection, b) rotation, c) azimuthal symmetry*

2.2.2.1.2. Speckle filtering techniques for polarimetric data

As for scalar data, the speckle filtering of polarimetric data is based on the use of independent realizations to reduce the variance of the different covariance matrix elements, which can generally be represented by nine real coefficients. In case of polarimetrically homogeneous data, which follow the multivariate complex Gaussian distribution of [2.20], the optimal estimate of a covariance matrix is given, for L independent views and in the sense of the maximum likelihood, by $\hat{\boldsymbol{T}} = \frac{1}{L}\sum_{l=1}^{L} \boldsymbol{k}(l)\boldsymbol{k}^{H}(l)$ [LEE 94a, LEE 94b, LEE 06, TOU 02].

Filtering forms

Some studies [LOP 92, LOP 97] proposed adaptive polarimetric filtering, i.e techniques that adapt to the shape of the covariance matrix and which process polarimetric channels differently according to their local statistics. Due to the risk of significant modifications to the matrix structure brought by an adaptive approach based on a limited number of views, this type of technique was then replaced by a scalar filtering of matrix-valued qualities, inspired by the single-channel case, which can be represented with an extension of the Lee filter as [LEE 94a, LEE 94b, LEE 06]:

$$\mathbf{T} = \widehat{\mathbf{T}} + b\,(\boldsymbol{T}_0 - \widehat{\mathbf{T}}) \qquad [2.36]$$

where $\boldsymbol{T}_0$ represents the covariance matrix of the pixel studied before filtering, whose number of equivalent views N_{eq_0} can be equal to 1 for initial mono-view data, or greater when using pre-filtered data. $\widehat{\boldsymbol{T}}$ is an estimate of the polarimetric second order statistics, generally obtained through a weighted linear filtering of the form $\widehat{\boldsymbol{T}} = \frac{1}{L}\sum_{l=1}^{L} w_i \boldsymbol{k}(l)\boldsymbol{k}^H(l)$. The scalar coefficient, $0 \leq b \leq 1$, regulates the filtering strength, according to the homogeneity of the L views used for the filtering. This coefficient is calculated from the $span\,(\boldsymbol{k}(l))$ statistics, as in the case of data acquired from a single polarization channel.

Filtering techniques

As in the scalar case, the main differences between filtering techniques, concern the selection of samples, $\boldsymbol{k}(l)$, during the estimation of the span local statistics. The three approaches mentioned in the single-channel case, the refined Lee filter [LEE 99], the *Intensity-Driven Adaptive-Neighborhood* (IDAN) filter [VAS 06], and the non-local filter [DEL 15], discussed in Chapter 1 of this volume, are illustrated in Figure 2.12. Some versions of these filtering methods use similarity measurements between local estimates of covariance matrices. Such an approach generally requires the use of a sufficient number of samples for the compared estimates to be actually representative of the local multivariate statistics. It is easy to see here the dilemma between the statistical accuracy and the spatial localization which is confronted by a multi-variate filter, which is partially bypassed using the span, to estimate the homogeneity of a series of samples and select its

most representative elements. The scalar information associated with the span shows converging statistics for a lower number of samples than in the case of a covariance matrix. However, the span is partial polarimetric information, whose values may not faithfully represent the variations of the total polarimetric response.

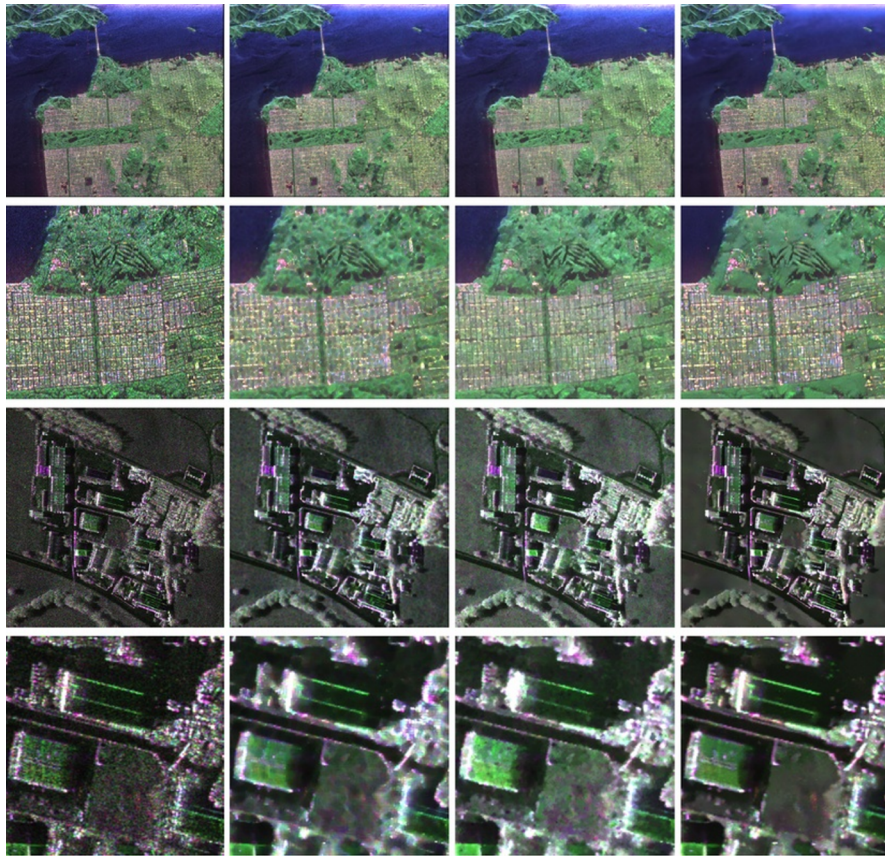

Figure 2.12. *Comparison of speckle filters for polarimetric data, given in [DEL 15], on a NASA/JPL/AirSAR image in L-band ($f_c = 1.3\,GHz$) of San Francisco (the two first lines: full image and detail) and on a DLR/FSAR image in S-band ($f_c = 3.25\,GHz$) of Kaufbeuren in Germany (the two last lines: full image and detail): a) initial two view image for San Francisco and one view for Kaufbeuren, b) refined Lee [LEE 99], c) IDAN [VAS 06], d) non-local [DEL 15]. For a color version of this figure, see www.iste.co.uk/baghdadi/2.zip*

2.2.2.2. *Incoherent polarimetric decomposition techniques*

2.2.2.2.1. Necessity of polarimetric decomposition

Deterministic and stochastic polarimetric responses

As previously presented, the polarimetric response of an object can be analyzed by comparing its relative scattering matrix, $\boldsymbol{S}_{rel}$, with that of the canonical targets, such as a sphere, a dihedral… The use of 2nd order statistics does not represent in itself a limitation to this type of interpretation, since a relative scattering matrix can be rebuilt from the hermitian product of a target vector, that is $\equiv \boldsymbol{k} \Rightarrow \boldsymbol{S}_{rel} \equiv \boldsymbol{k}\boldsymbol{k}^H$. However, the incoherent average operation associated with speckle filtering significantly disturbs this type of interpretation. In fact, the only configuration for which it is possible to unambiguously associate a relative scattering matrix with a coherence matrix represents a very specific case of statistical distribution, which is very unlikely in practice, with:

$$\mathbf{k}(l) = a(l)\boldsymbol{k}_0 \Rightarrow \quad \mathbf{T} = \mathrm{E}(\boldsymbol{k}\boldsymbol{k}^H) = A\boldsymbol{k}_0\boldsymbol{k}_0^H \equiv \boldsymbol{S}_{rel_0} \qquad [2.37]$$

In such a case, the speckle effect similarly affects the different polarimetric channels through the scalar quantity $a(l)$, the relative amplitudes and phases of the different channels remain constant, and the polarimetric response is said to be deterministic. Other more realistic configurations consider the polarimetric response as composed of a large number of independent contributions, N_s, which are superimposed within the same resolution cell, and homogeneously in a neighborhood within which samples are selected:

$$\left.\begin{array}{c} \boldsymbol{k}(l) = \sum_{n=1}^{N_s} \boldsymbol{k}_n(l) \\ E\left(\boldsymbol{k}_n(l)\boldsymbol{k}_m^H(l)\right) = \boldsymbol{T}_n\delta_{n-m} \end{array}\right\} \Rightarrow \quad \mathbf{T} = \mathrm{E}(\boldsymbol{k}\boldsymbol{k}^H) = \sum_{n=1}^{N_s} \boldsymbol{T}_n \not\equiv \boldsymbol{S}_{rel} \qquad [2.38]$$

In this case, very often encountered in practice, a covariance matrix cannot be linked without ambiguity to a relative scattering matrix.

Distributed target concept

A target is said to be distributed if its polarimetric response cannot be represented by a single relative scattering matrix $\boldsymbol{S}_{rel}$, as was shown in [2.38]. This property can be illustrated in a number of different ways, in particular through the decomposition of the polarimetric covariance matrix into eigen-elements, $\boldsymbol{T} = \boldsymbol{U}\boldsymbol{\Lambda}\boldsymbol{U}^H = \sum_{i=1}^{3} \lambda_i \boldsymbol{u}_i \boldsymbol{u}_i^H$. For a deterministic

response such as the one described in [2.37], we obtain $\boldsymbol{u}_1 = \boldsymbol{k}_0 / \sqrt{\boldsymbol{k}_0^H \boldsymbol{k}_0}$, $\lambda_1 = A\boldsymbol{k}_0^H \boldsymbol{k}_0$, $\lambda_2 = \lambda_3 = 0$, whereas for the general case of [2.38], we have $\lambda_i > 0, \forall i$ and the response energy is "distributed" over several orthogonal scattering mechanisms, $\boldsymbol{u}_i$. We can also use the concept of degrees of freedom (DoF), which is easily highlighted through the following covariance matrix factorization:

$$\mathbf{T} = \begin{bmatrix} \sqrt{T_{11}} & 0 & 0 \\ 0 & \sqrt{T_{22}} & 0 \\ 0 & 0 & \sqrt{T_{33}} \end{bmatrix} \begin{bmatrix} 1 & \rho_{12} & \rho_{13} \\ \rho_{12}^* & 1 & \rho_{23} \\ \rho_{23}^* & \rho_{23}^* & 1 \end{bmatrix} \begin{bmatrix} \sqrt{T_{11}} & 0 & 0 \\ 0 & \sqrt{T_{22}} & 0 \\ 0 & 0 & \sqrt{T_{33}} \end{bmatrix} \quad [2.39]$$

For a deterministic polarimetric response, sometimes called "pure", we have $\boldsymbol{T} = \lambda_1 \boldsymbol{u}_1 \boldsymbol{u}_1^H$ and so $|\rho_{ij}| = 1, \rho_{23} = \rho_{12}^* \rho_{13}$. The covariance matrix is then fully defined by five real values, $\boldsymbol{T} \equiv \{T_{11}, T_{22}, T_{33}, arg(\rho_{12}), arg\,(\rho_{13})\}$, and $DoF(\boldsymbol{T}) = DoF(\boldsymbol{S}_{rel}) = 5$. It is then possible to interpret the polarimetric scattering phenomenon through a more or less advanced comparison of the five DoF polarimetric representations with those obtained for canonical targets, and to deduce from it some physical properties of the objects measured. For a distributed matrix, $\boldsymbol{T} = \sum_{i=1}^{3} \lambda_i \boldsymbol{u}_i \boldsymbol{u}_i^H$, $\boldsymbol{T} \equiv \{T_{11}, T_{22}, T_{33}, |\rho_{12}|, |\rho_{13}|, |\rho_{23}|, arg(\rho_{12}), arg(\rho_{13}), arg\,(\rho_{23})\}$, and we find $DoF(\boldsymbol{T}) = 9 > DoF(\boldsymbol{S}_{rel}) = 5$. That profusion of DoF does not allow a direct interpretation of the link between the characteristics of the observed medium and those of the wave scattered by it. We then employ decomposition techniques [HUY 70, CLO 96, CLO 97].

Objectives of the polarimetric decomposition techniques

The main objective of the polarimetric decomposition techniques is to characterize a polarimetric response by means of one or several scattering mechanisms. Four approaches are generally identified:

– coherent decompositions, which express a scattering matrix, $\boldsymbol{S}$ as the linear combination of matrices associated with canonical scattering mechanisms. That type of approach is suitable for analyzing deterministic features and loses its appeal for the study of distributed responses;

– decomposition techniques based on dichotomy, whose objective is to represent a covariance matrix under the form of a pure term, that is to rank one covariance matrix, $\boldsymbol{T}_0$, and a residue, $\boldsymbol{T}_{rem}$: $\boldsymbol{T} = \boldsymbol{T}_0 + \boldsymbol{T}_{rem}$. Dichotomy is usually performed according to physical considerations;

– approaches using the decomposition into eigen-elements of the covariance matrix;

– approaches based on a scattering model associating the covariance matrix with a series of arbitrary rank components.

2.2.2.2.2. A few methods based on orthogonal scattering mechanisms

Those approaches are based on the decomposition into eigen-elements of the covariance matrix $\boldsymbol{T} = \boldsymbol{U}\boldsymbol{\Lambda}\boldsymbol{U}^H = \sum_{i=1}^{3} \lambda_i \boldsymbol{u}_i \boldsymbol{u}_i^H$, with $\lambda_i \geq \lambda_{i+1}$ and $\boldsymbol{u}_j^H \boldsymbol{u}_i = \delta_{i-j}$. As was previously shown, the analysis of $\boldsymbol{T}$ when $\lambda_2 > 0$, that is to say in the presence of a polarimetrically distributed response, faces a profusion of DoF that is hard to interpret. Approaches aiming at extracting a representative mechanism from eigen-elements to the covariance matrix were proposed to address this issue.

Dominant or average scattering mechanism

The first approach, suggested by Cloude [CLO 86b], considers the dominant mechanism, i.e. the mechanism with the highest associated intensity. This decomposition is similar to a 1st order principal component analysis, from which a relative scattering matrix can be extracted:

$$\mathbf{S}_{rel} \equiv \sqrt{\lambda_1}\boldsymbol{v}_1 = \mathbf{k}_1 \qquad [2.40]$$

The reconstructed principal target vector can be expressed up to an arbitrary phase term, as a function of the $\boldsymbol{S}_{rel}$ elements, the Huynen parameters of a pure target or angular variables, as:

$$\mathbf{k}_1 = \frac{1}{\sqrt{2}}\begin{bmatrix} S_{hh} + S_{vv} \\ S_{hh} - S_{vv} \\ 2S_{hv} \end{bmatrix} = \begin{bmatrix} \sqrt{2A_0} \\ \sqrt{B_0 + B}\, e^{jarg(C+jD)} \\ \sqrt{B_0 - B}\, e^{jarg(G+jH)} \end{bmatrix}$$
$$= \boldsymbol{k}_1^H \mathbf{k}_1 \begin{bmatrix} cos\,\alpha \\ sin\,\alpha\, cos\,\beta\, e^{j\delta} \\ sin\,\alpha\, sin\,\beta\, e^{j\gamma} \end{bmatrix} \qquad [2.41]$$

The scattering mechanism associated with $\boldsymbol{k}_1$ can be characterized by means of various tools, including the Huynen generating parameters. The mechanism is called a simple reflection if $A_0 >> B_0 + B$ and $B_0 - B$, a double reflection if $B_0 + B >> A_0$ and $B_0 - B$, or otherwise scattering by an anisotropic particle. An example application of that decomposition on the AirSAR image of San Francisco Bay is given in Figure 2.13, by means of color coded images which demonstrate that this approach helps to capture the main polarimetric features of the observed scene. In this case, the drastic size reduction associated with the selection of the single first eigenvector, necessary to interpret the scattering mechanisms, does not excessively affect the representativeness of the decomposed data.

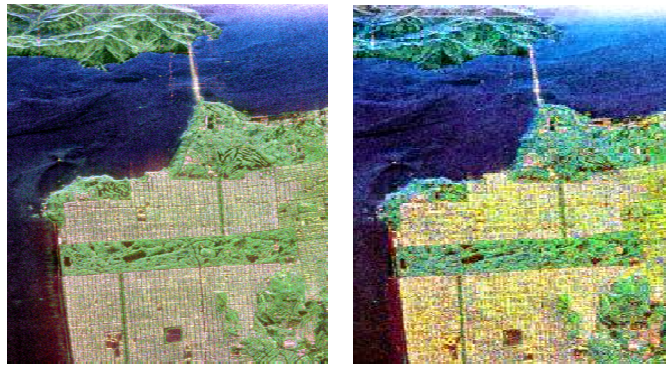

Figure 2.13. *Comparison of polarimetric color coded images in the Pauli basis of the San Francisco Bay: a) original image, b) image rebuilt from the dominant scattering mechanism, $\boldsymbol{k}_1 = \sqrt{\lambda_1}\boldsymbol{v}_1$. For a color version of this figure, see www.iste.co.uk/baghdadi/2.zip*

This very simple decomposition approach is only based on part of the polarimetric information, associated with the first eigenvector, whose predominance can be measured with $0 \leq \frac{\lambda_1}{span} \leq 1$. To take into account the significance of each of the eigen-elements of the covariance matrix, we define their pseudo-probability, p_i, as [CLO 95, CLO 96]:

$$\boldsymbol{T} = \mathbf{U}\boldsymbol{\Lambda}\mathbf{U}^H = span \sum_{i=1}^{3} p_i \boldsymbol{u}_i \boldsymbol{u}_i^H = span \sum_{i=1}^{3} p_i \boldsymbol{T}_i$$

$$\text{with } p_i = \frac{\lambda_i}{span} \text{ and } \sum_{i=1}^{3} p_i = 1 \qquad [2.42]$$

where $\boldsymbol{T}_i$ represents a unitary rank matrix. Those pseudo-probabilities are used to rebuild a target vector representing the average scattering mechanism, from each of the parameterized eigenvectors:

$$\mathbf{u}_i = \begin{bmatrix} cos\,\alpha_i \\ sin\,\alpha_i\,cos\,\beta_i\,e^{j\delta_i} \\ sin\,\alpha_i\,sin\,\beta_i\,e^{j\gamma_i} \end{bmatrix} \Rightarrow \bar{\mathbf{u}} = \begin{bmatrix} cos\,\bar{\alpha} \\ sin\,\bar{\alpha}\,cos\,\bar{\beta}\,e^{j\bar{\delta}} \\ sin\,\bar{\alpha}\,sin\,\bar{\beta}\,e^{j\bar{\gamma}} \end{bmatrix} \text{ where } \bar{x} = \sum_{i=1}^{3} p_i\,x_i \quad [2.43]$$

We note that despite the fact that the averaging presented in [2.43] depends on the formalism used to parameterize a target vector and does not take into account the orthogonality of the different eigen-elements, it ensures the adaptive consideration of the eigenvalue distribution of $\boldsymbol{T}$, with $\bar{\boldsymbol{u}} = \boldsymbol{u_1}$ for a deterministic response and $\bar{\boldsymbol{u}} = f(\boldsymbol{u_1}, \boldsymbol{u_2}, \boldsymbol{u_3})$ for distributed responses. The representativity of this eigenanalysis can be evaluated by means of two parameters describing the eigenvalue distribution, the entropy, H, and the anisotropy, A, defined as [CLO 95, CLO 96]:

$$H = -\sum_{i=1}^{3} p_i\ log_3\,p_i \text{ and } A = \frac{p_3 - p_2}{p_3 + p_2} \text{ with } 0 \leq H, A \leq 1 \quad [2.44]$$

where the entropy, borrowed from information theory, is an indicator of the random nature of the polarimetric scattering phenomenon, with $H = 0$ for a deterministic scattering, and $H = 1$ for a fully distributed scattering with $\lambda_i = \frac{1}{3}, \forall i$. The entropy can be understood as a measure of the reconstituted dominant or average mechanism representativity, or an indicator of the complexity of the imaged environments. The anisotropy indicates the significance of the third eigen-element relative to that of the second element. As they are expressed from the set of the relative eigenvalues of the covariance matrix, H and A are invariant through any transformation of the type $\boldsymbol{T'} = \boldsymbol{QTQ}^H$, $|\boldsymbol{Q}| \neq 0$, which takes into account any change of polarimetric basis, $\boldsymbol{Q} = \boldsymbol{U}(\phi, \tau)$, or of the covariance matrix representation, $\boldsymbol{Q} = \boldsymbol{P}_{\boldsymbol{T}\rightarrow\boldsymbol{C}}$. The two key parameters of that decomposition are the entropy (H), and $\bar{\alpha}$, the indicator of the average scattering mechanism nature, $0° \leq \bar{\alpha} \leq 90°$, that can be interpreted by means of the scattering matrices given in Table 2.2. Thus, we have $\bar{\alpha} = \alpha_{trihedral} = 0°$ for a sphere or a plate, $\bar{\alpha} = \alpha_{dipole\_45} = 45°$ for randomly orientated anisotropic particles, and $\bar{\alpha} = \alpha_{dihedral} = 90°$ for a canonical dihedral. The parameters α_i and $\bar{\alpha}$ are invariant by rotation around the radar line of sight, that is for

$\boldsymbol{T'} = \boldsymbol{U}(\phi)\boldsymbol{T}\boldsymbol{U}^H(\phi)$. The color coded images of Figure 2.14 show that the average mechanism estimated according to [2.43] may be used to reconstruct polarimetric information with more contrast than the one estimated by means of the only dominant mechanism, due to the lack of representativity of the latter for areas with high entropy values, i.e. where several eigen-elements are required to analyze a covariance matrix.

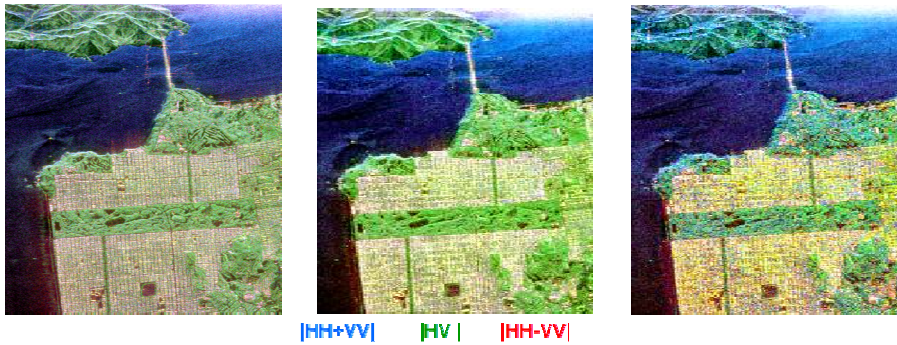

Figure 2.14. *Comparison of color coded polarimetric images in the Pauli basis of the San Francisco Bay: a) original image, b) image reconstructed from the dominant scattering mechanism* $\boldsymbol{k}_1 = \sqrt{\lambda_1}\boldsymbol{u}_1$, *c) image reconstructed from the average scattering mechanism* $\bar{\boldsymbol{k}} = \sqrt{span}\bar{\boldsymbol{u}}$. *For a color version of this figure, see www.iste.co.uk/baghdadi/2.zip*

The potential of interpretation of the wave scattering over various environments can be assessed in Figure 2.15. The entropy has low values in environments with a low complexity, such as the ocean, associated in the L-band with a slightly rough surface, and reaches high values over volumetric over volumetric environments, in particular those covered by vegetation, whose covariance matrix takes a form close to the diagonal. Urban areas, at such a resolution, present responses mixing two dominant contributions: the highly energetic ground-wall double bounce, linked to a specular reflection phenomenon, and a surface response, originating from the ground and the roofs of the buildings. Anisotropy proves to be highly complementary to entropy on the parts of the image characterized by two dominant mechanisms, like urban areas and coastal oceanic surfaces. The parameter $\bar{\alpha}$ allows us to qualify the type of wave–matter interaction and represents a good indicator of the type of environment measured.

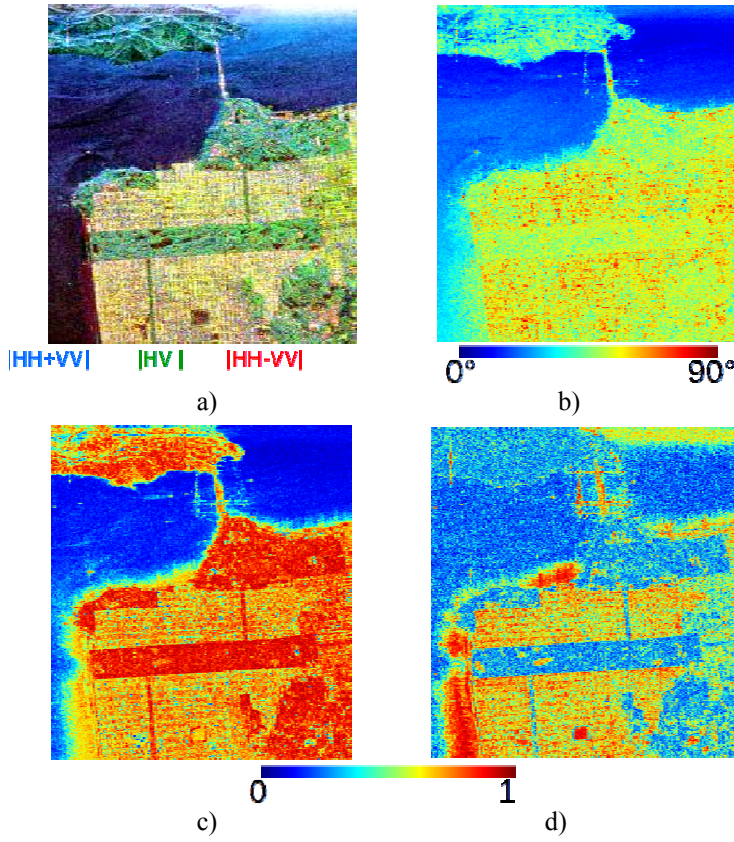

Figure 2.15. *Result of the eigen-decomposition over the San Francisco Bay: a) Pauli image, b) $\bar{\alpha}$, c) H, d) A. For a color version of this figure, see www.iste.co.uk/baghdadi/2.zip*

The complementary nature of parameters H and A can be assessed in Figure 2.16, which shows various combinations whose sum is unitary. A value $x(1-y)$ close to 1 means, for $0 \leq x, y \leq 1$, that $x, (1-y) \approx 1$ and so that $x \approx 1$ and $y \approx 0$.

The parameters $H, A, \bar{\alpha}$ can be used to classify the different pixels of an image and identify different types of imaged environments, as shown in Figure 2.17. A set of thresholds, arbitrarily defined in a 3D space, is used to label each pixel according to a typical scattering behavior.

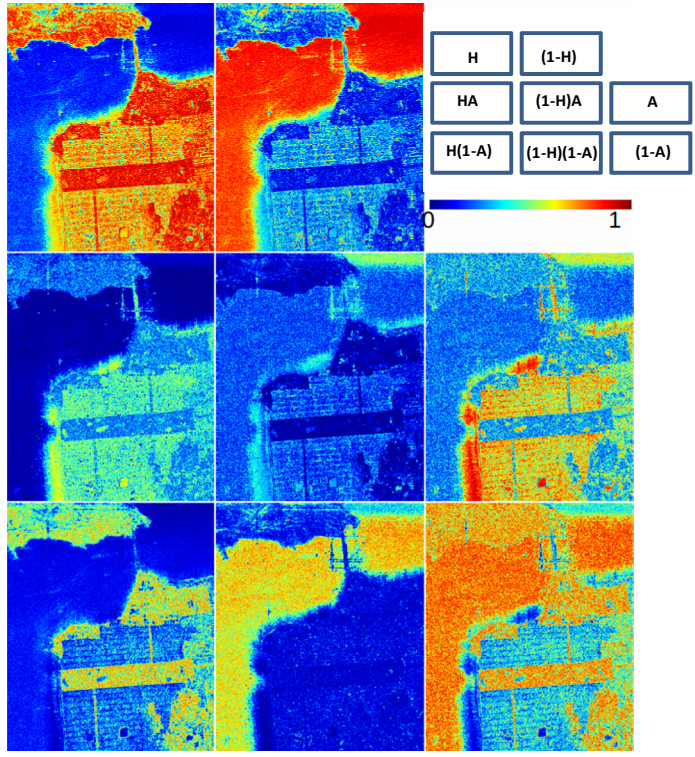

Figure 2.16. *Different combinations of the H and A parameters (San Francisco Bay). For a color version of this figure, see www.iste.co.uk/baghdadi/2.zip*

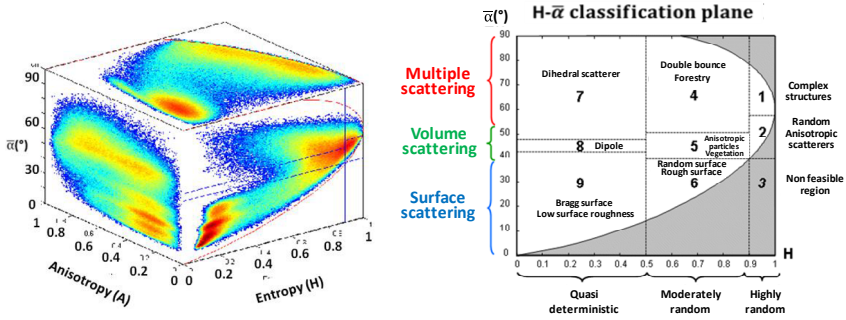

a) b)

Figure 2.17. *a) Density resulting from the projection of the pizels of the San Francisco Bay in the $(H, A, \bar{\alpha})$ domain, b) plane $(H, \bar{\alpha})$ segmented in regions associated with typical scattering mechanisms. For a color version of this figure, see www.iste.co.uk/baghdadi/2.zip*

The classification results of Figure 2.18 show an image labeled according to the arbitrary division of the plane $H - \bar{\alpha}$ shown in Figure 2.17. The interpretation and/or the borders of the different classes defined in this plane are likely to change significantly according to the measurement conditions, in particular the carrier frequency used.

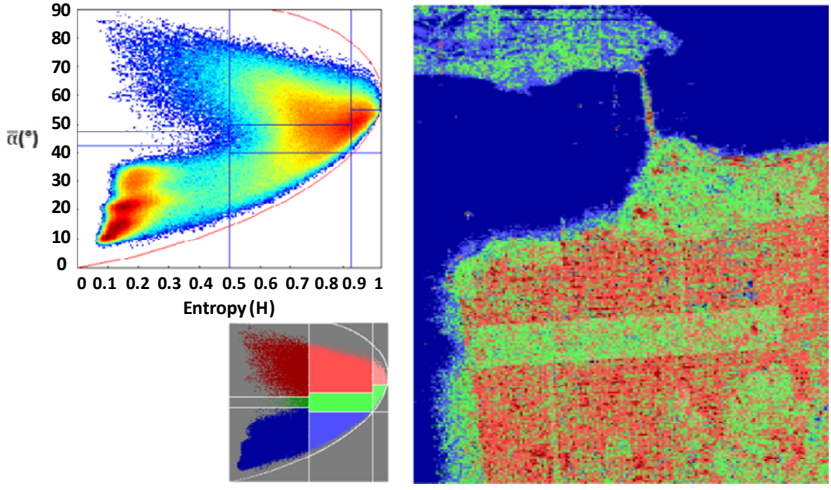

a) b)

Figure 2.18. *$H - \bar{\alpha}$ classification of the San Francisco Bay image: a) density of the image pixel projection in the $(H, \bar{\alpha})$ domain and color coding, b) classified image. For a color version of this figure, see www.iste.co.uk/baghdadi/2.zip*

2.2.2.2.3. Decompositions into canonical scattering mechanisms

Those techniques model the polarimetric response within each pixel corresponding to an environment under the form $\boldsymbol{S} = \sum_i \boldsymbol{S}_{mod_i}$, where $\boldsymbol{S}_{mod_i}$ represents the response of a specific scattering mechanism. As the different components of the global response represent different mechanisms within the medium observed, we generally consider that they are affected by independent speckle realizations, and so are not correlated. The global polarimetric covariance matrix can then be written under the form $\boldsymbol{C} = \sum_i \boldsymbol{C}_i(\boldsymbol{\theta}_i)$, where $\boldsymbol{\theta}_i$ represents a set of parameters describing the associated contribution. The estimation of the different parameters, especially of the power of each term, makes it possible to detect and identify some characteristic components of complex environments. The Freeman–Durden approach [FRE 98] decomposes a polarimetric covariance matrix

under the form of three contributions associated with the canonical responses of simple reflection, double reflection and volume scattering. The volume component is modeled under the form of a sum of scattering contributions from anisotropic particles, represented by a randomly oriented lexicographic target vector or $\boldsymbol{k}_{part} = [a, 0, b]^T$, as:

$$\boldsymbol{C}_v = lim_{b\to 0} \int_0^{2\pi} \boldsymbol{U}_C(\phi)\, \boldsymbol{k}_{part} \boldsymbol{k}_{part}^H \boldsymbol{U}_C^H(\phi)\, \mathrm{d}\phi = \frac{f_v}{8} \begin{bmatrix} 3 & 0 & 1 \\ 0 & 2 & 0 \\ 1 & 0 & 3 \end{bmatrix} \quad [2.45]$$

whereas the simple and double reflection mechanisms are associated with pure polarimetric, that is rank 1 responses:

$$\boldsymbol{C}_s = f_s \begin{bmatrix} |\alpha|^2 & 0 & \alpha \\ 0 & 0 & 0 \\ \alpha^* & 0 & 1 \end{bmatrix} \text{ and } \boldsymbol{C}_d = f_d \begin{bmatrix} |\beta|^2 & 0 & \beta \\ 0 & 0 & 0 \\ \beta^* & 0 & 1 \end{bmatrix} \quad [2.46]$$

The terms f_x in [2.45] and [2.46] correspond to coefficients modulating the intensity of volume canonical scattering mechanisms, simple or double reflections, signaled by their respective index, $x = v, s$ or d. The global model of polarimetric response is given by:

$$\boldsymbol{C} = \boldsymbol{C}_s + \boldsymbol{C}_d + \boldsymbol{C}_v = \begin{bmatrix} f_s|\alpha|^2 + f_d|\beta|^2 + \frac{3f_v}{8} & 0 & f_s\alpha + f_d\beta + \frac{f_v}{8} \\ 0 & \frac{f_v}{4} & 0 \\ f_s\alpha^* + f_d\beta^* + \frac{f_v}{8} & 0 & f_s + f_d + \frac{3f_v}{8} \end{bmatrix} \quad [2.47]$$

with $span(\boldsymbol{C}) = P_s + P_d + P_v$ and $P_s = f_s(1 + |\alpha|^2)$, $P_d = f_d(1 + |\beta|^2)$, $P_v = f_v$. Estimation parameter of this decomposition requires us to determine five parameters from only four equations. It is suggested in [FRE 98] to replace $\boldsymbol{C}_s$ or $\boldsymbol{C}_d$ by a canonical expression according to the argument of $E(S_{hh}S_{vv}^*)$. If $\mathcal{R}\big(E(S_{hh}S_{vv}^*)\big) > 0$, then this correlation term is dominated by the simple reflection contribution, and we set $\beta = -1$, or otherwise we impose $\alpha = 1$. This decomposition technique implies that the environment response has a reflection symmetry property, that is $E\big(S_{pp}S_{pq}^*\big) = 0$, with $p, q = h$ or v, which may not be verified in practice. In addition, the estimation of the different model parameters from [2.47] can lead to outliers resulting in negative powers, or in non postitive semi-definite

compounds. The Freeman–Durden decomposition results are shown in Figure 2.19.

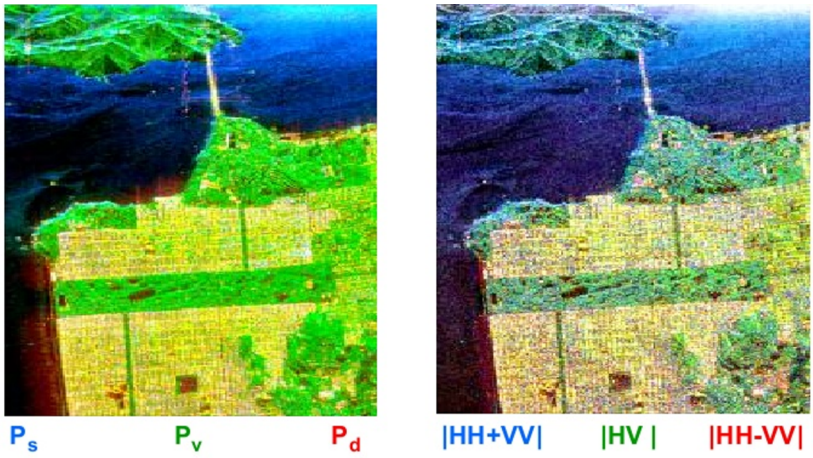

Figure 2.19. *Comparison of color coded polarimetric images in the Pauli basis of the San Francisco Bay: a) image reconstructed from the intensity of canonical scattering mechanism of the Freeman–Durden decomposition, b) original color coded image (not decomposed). For a color version of this figure, see www.iste.co.uk/baghdadi/2.zip*

We notice that this decomposition tends to overestimate the volume component, and is, by definition, not adapted to environments presenting correlations between co- and cross-polar channels; i.e. orientated environments or environments with artificial structures.

2.2.3. *A few applications using polarimetric SAR images*

2.2.3.1. *Advanced decomposition techniques*

2.2.3.1.1. Approaches based on a scattering model

Two-term Freeman decomposition

This approach models the response of a terrain with 2 compounds. A rank 1 ground covariance which represents simple or double reflections, where a full rank term, $\boldsymbol{C}_v$, is associated with volume scattering [FRE 07]. The total covariance matrix is written:

$$\boldsymbol{C} = \boldsymbol{C}_g + \boldsymbol{C}_v = f_g \begin{bmatrix} |\alpha|^2 & 0 & \alpha \\ 0 & 0 & 0 \\ \alpha^* & 0 & 1 \end{bmatrix} + f_v \begin{bmatrix} 1 & 0 & \rho \\ 0 & 1-\rho & 0 \\ \rho & 0 & 1 \end{bmatrix} \quad [2.48]$$

This approach, illustrated in Figure 2.20, proves to be more robust than the approach using three components, as it does not result in an underdimensioned system and allocates to the volume component an additional degree of freedom, helping to better condition the parameter elimination parameters, as mentioned above.

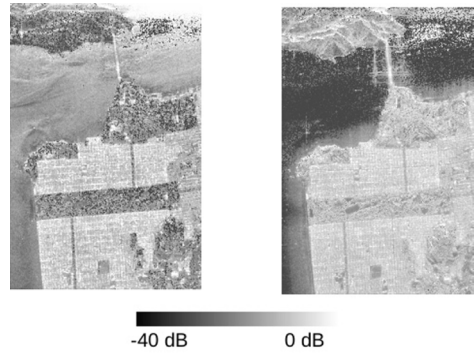

Figure 2.20. *Images of the intensity of the compounds of the of the two-element Freeman decomposition for the San Francisco Bay: a) ground component, b) volume component*

Four-term Yamaguchi decomposition

Polarimetric responses measured over complex environments, containing in particular artificial structures like urban areas, may not verify the reflection symmetry property on which are based the decomposition techniques suggested by Freeman–Durden and Freeman. The application of those methods with no previous modification can result in a significant loss of information. To address this limitation, the approach developed by Yamaguchi *et al.* [YAM 05] suggests to add to the three component model a fourth rank 1 component associated with the response of a left or right helix:

$$\mathbf{C}_{lh,rh} = f_h \begin{bmatrix} 1 & \mp j\sqrt{2} & -1 \\ \pm j\sqrt{2} & 2 & \mp j\sqrt{2} \\ -1 & \pm j\sqrt{2} & 1 \end{bmatrix} \quad [2.49]$$

The volume contribution is also modified to take into account a more adapted particle distributions. Thus, the volume covariance matrix is obtained through the disorientation of $\boldsymbol{k}_{part} = [a, 0, b]^T$, as:

$$\boldsymbol{C}_{v_{ab}} = \int_0^{2\pi} \boldsymbol{U}_C(2\phi)\, \boldsymbol{k}_{part} \boldsymbol{k}_{part}^H \boldsymbol{U}_C^H(2\phi) f_\phi(\phi) \mathrm{d}\phi$$

$$\text{with } f_\phi(\phi) = \frac{1}{2} cos\ \phi \text{rect}\left(\frac{\phi}{\pi}\right) \qquad [2.50]$$

where $\text{rect}(x) = 1, \forall |x| < \frac{1}{2}$ and is nowhere else. Two cases are then considered, depending on whether the particles composing the volume are orientated around the vertical, $\boldsymbol{C}_{v_v}$, or horizontal, $\boldsymbol{C}_{v_h}$, direction:

$$\boldsymbol{C}_{v_v} = \lim_{a \to 0} \boldsymbol{C}_{v_{ab}} = \frac{f_v}{15} \begin{bmatrix} 8 & 0 & 2 \\ 0 & 4 & 0 \\ 2 & 0 & 3 \end{bmatrix} \text{ and } \boldsymbol{C}_{v_h} = \lim_{b \to 0} \boldsymbol{C}_{v_{ab}} = \frac{f_v}{15} \begin{bmatrix} 3 & 0 & 2 \\ 0 & 4 & 0 \\ 2 & 0 & 8 \end{bmatrix} \qquad [2.51]$$

The expression of the global model is given by $\boldsymbol{C} = \boldsymbol{C}_s + \boldsymbol{C}_d + \boldsymbol{C}_h + \boldsymbol{C}_v$ and its estimation, more complex than the one of the Freeman–Durden approach, requires the selection of the most adapted helix, $\boldsymbol{C}_h = \boldsymbol{C}_{lh}$ or $\boldsymbol{C}_{rh}$, and volume responses (Figure 2.21).

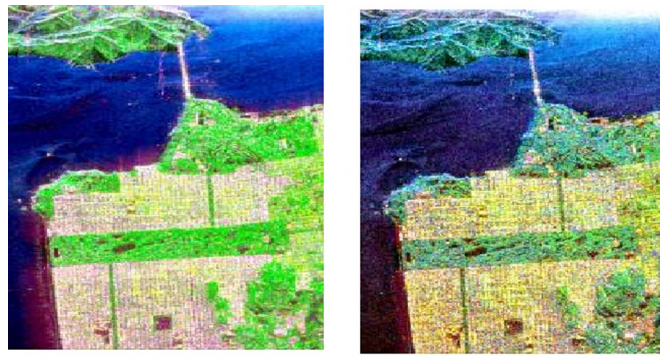

Figure 2.21. *Comparison of color coded polarimetric images in the Pauli basis of the San Francisco Bay: a) image reconstructed from canonical mechanism intensities s,d,v of the Yamaguchi decomposition, b) original image. For a color version of this figure, see www.iste.co.uk/baghdadi/2.zip*

Neumann decomposition with an advanced description of the volume contribution

This approach [NEU 09] considers a volume composed of lexicographic target vector particles $\boldsymbol{k}_{part} = [a, 0, b]^T = A[1 + \delta^*, 0, 1 - \delta^*]^T$, oriented according to a truncated normal law, whose dispersion, τ, is parametric:

$$f_\phi(\phi) = \frac{cos(2(\phi - \bar{\phi}))}{\pi\tau} \text{ with } \tau = I_0(\kappa)e^{-\kappa} \qquad [2.52]$$

where $\bar{\phi}$ represents the average orientation of particles and κ is the degree of concentration of the distribution, similar to the reverse of the standard deviation of $f_\phi(\phi)$. The different types of particles simulated by means of the parameters δ and τ are described in Figure 2.22. The global covariance matrix is given by a ground component and a volume component, through $T = f_g\boldsymbol{T}_g + f_v\boldsymbol{T}_v$, with:

$$\boldsymbol{T}_v = \boldsymbol{U}_{3T}(\bar{\phi}) \begin{bmatrix} 1 & g_c\delta & 0 \\ g_c\delta^* & \frac{1+g}{2}|\delta|^2 & 0 \\ 0 & 0 & \frac{1-g}{2}|\delta|^2 \end{bmatrix} \boldsymbol{U}_{3T}^H(\bar{\phi})$$

$$\text{and } \boldsymbol{T}_g = \begin{bmatrix} 1 & \beta & 0 \\ \beta^* & \beta_{22} & 0 \\ 0 & 0 & \beta_{33} \end{bmatrix} \qquad [2.53]$$

where $g = I_2(\kappa)/I_0(\kappa)$ and $g_c = I_1(\kappa)/I_0(\kappa)$ and with a full rank ground contribution. This decomposition technique models, with a reduced number of parameters, the response of a very realistic volume, allocating a high number of degrees of freedom to the ground contribution. The estimation of the different parameters can be adaptively conducted using the *Non Negative Eigenvalue Decomposition* (NNED) approach [VAN 11] presented below. Figure 2.22 illustrates the relevance of that approach by comparing its definition domain with those of the Freeman and Yamaguchi approaches.

Another adaptive method and NNED estimation

Similarly to the previous approach, this technique models a volume as a cloud of anisotropic particles, randomly orientated according to the following law:

$$f_{\phi}(\phi) = \frac{cos^{2n}(\phi - \bar{\phi})}{\int_0^{2\pi} cos^{2n}(\phi - \bar{\phi})} \quad [2.54]$$

where n represents the distribution order that sets the dispersion τ [ARI 10, ARI 11]. This type of law helps to generate a quasi-deterministic distribution, when $n \to +\infty$, up to a uniform distribution, for $n = 0$, as shown in Figure 2.23. The global polarimetric covariance model is given by:

$$\mathbf{C} = \boldsymbol{C}_s + \boldsymbol{C}_d + f_v \boldsymbol{C}_v(\bar{\phi}, n) + \boldsymbol{C}_{rem} \quad [2.55]$$

where $\boldsymbol{C}_{rem}$ represents the estimation residue, that is the part of $\boldsymbol{C}$ that cannot be explained by the suggested model. The NNED estimation approach, or positive semi-definite estimation, is then applied to find the optimal volume parameters, that verify:

$$(f_v, \bar{\phi}, n)_{opt} = arg\, min_{(f_v, \bar{\phi}, n)}\, tr(\boldsymbol{C}'_{rem}) \text{ with}$$
$$\boldsymbol{C}'_{rem} = \mathbf{C} - f_v \boldsymbol{C}_v(\bar{\phi}, n) \text{ and } \boldsymbol{C}'_{rem} \geq \mathbf{0} \quad [2.56]$$

with $tr(\boldsymbol{C}'_{rem})$, the span of residual term from which are estimated the contributions $\boldsymbol{C}_s$ and $\boldsymbol{C}_d$, whose constraint $\boldsymbol{C}'_{rem} \geq \mathbf{0}$ ensures the semi- an adequate parameterization. The performances of that approach can be assessed in Figure 2.23.

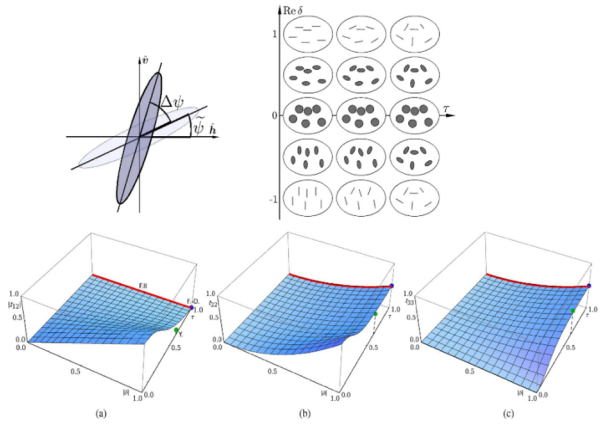

Figure 2.22. *Illustration of the Neumann adaptive decomposition. Top: example of particles modeled by means of parameters $\tau, \delta, \phi = \psi$; bottom: illustration of $\tau, |\delta|$ domains covered by the Freeman–Durden decompositions (blue), Freeman II (red), Yamaguchi (green) for a) $|T_{12}|$, b) T_{22} and c) T_{33}. For a color version of this figure, see www.iste.co.uk/baghdadi/2.zip*

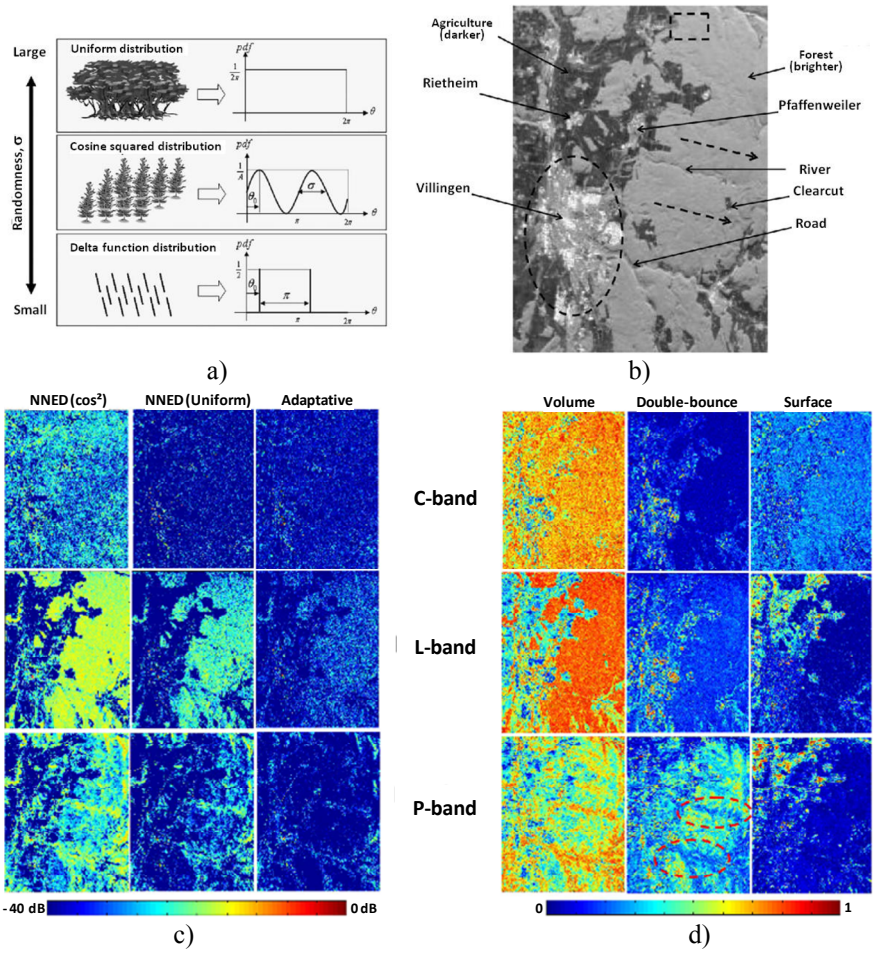

Figure 2.23. *Results of the polarimetric decomposition approach based on an adaptive model [ARI 11], applied to the polarimetric image measured in the L-band by the JPL/AirSAR sensor over the Black Forest, Germany: a) orientation distributions used, b) $span(C)$ in C-band, c) $span(C_{rem})/span(C)$, d) $P_i/span$ for each identified component. For a color version of this figure, see www.iste.co.uk/baghdadi/2.zip*

2.2.3.1.2. Generalization of the approach based on an eigen-decomposition

Among the various polarimetric decomposition approaches based on the eigen-elements of the covariance matrix, we can quote the method developed in Paladini *et al.* [PAL 12], which aims at improving two aspects linked to

the estimation of the dominant or average mechanism presented in [2.43] and [2.44]:

– among the four angular variables used to parameterize a target vector in [2.43], only α is rotationally invariant around the radar line of sight;

– the definition of an average mechanism by means of the different angular variables on the different eigen-elements [2.43] can result in a significant bias and a potentially erroneous interpretation of the scattering mechanism.

The invariance improvement is provided by redefining the parametrization of a target vector in the circular basis. The application of a rotation on the target vector in the basis $(l, l_\perp)$ can be written as:

$$\boldsymbol{k}_{(l,l_\perp)}(\phi) = \mathbf{R}(\phi)\boldsymbol{k}_{(l,l_\perp)}, \text{ with } \boldsymbol{k}_{(l,l_\perp)} = \frac{1}{2}\begin{bmatrix} S_{hh} - S_{vv} + j2S_{hv} \\ j\sqrt{2}(S_{hh} + S_{vv}) \\ S_{vv} - S_{hh} + j2S_{hv} \end{bmatrix},$$

$$\mathbf{R}(\phi) = \begin{bmatrix} e^{-j2\phi} & 0 & 0 \\ 0 & 0 & 0 \\ 0 & 0 & e^{j2\phi} \end{bmatrix} \quad [2.57]$$

This relationship shows that contrary to what happens in the Pauli basis, an azimuthal rotation may be summarized, in the circular polarization basis, by a symmetric phase term. A unit target vector may be parameterized under the following form:

$$\boldsymbol{k}_{(l,l_\perp)}(\phi) = \mathbf{R}(\phi)\mathbf{R}(\Upsilon)\mathbf{R}(\beta_c)\mathbf{R}(\alpha)\begin{bmatrix}1\\0\\0\end{bmatrix} = \begin{bmatrix} \sin\alpha\cos\beta_c e^{-j(\frac{4}{3}\Upsilon+2\phi)} \\ \cos\alpha e^{j(\frac{8}{3}\Upsilon)} \\ -\sin\alpha\sin\beta_c e^{-j(\frac{4}{3}\Upsilon-2\phi)} \end{bmatrix} \quad [2.58]$$

where the various parameters can be interpreted as follows:

– ϕ represents the target vector orientation around the line of sight, which may be close to the one of the imaged object;

– Υ is an indicator of the anisotropic nature of the polarimetric response, i.e., of its sensitivity to the polarization state used for the transmission and reception of the SAR signal;

– α is identical to the Cloude–Pottier decomposition parameter and indicates the nature of the scattering mechanism;

– β_c represents the contribution of the helix type scattering mechanism in the polarimetric response.

In the same way as the approach suggested in [2.42], the covariance matrix expressed in the circular basis can be decomposed into eigen-elements, by:

$$\boldsymbol{T}_{(l,l_\perp)} = \mathbf{U}\boldsymbol{\Lambda}\mathbf{U}^H, \text{ with } \boldsymbol{u}_i = \begin{bmatrix} sin\,\alpha_i\, cos\,\beta_{c_i} e^{-j(\frac{4}{3}\Upsilon_i + 2\phi_i)} \\ cos\,\alpha_i e^{j(\frac{8}{3}\Upsilon_i)} \\ -sin\,\alpha_i\, sin\,\beta_{c_i} e^{-j(\frac{4}{3}\Upsilon_i - 2\phi_i)} \end{bmatrix} \quad [2.59]$$

The potential bias provided by an average characterization of the type $\bar{x} = \sum_{i=1}^{3} p_i x_i$ can be avoided by rigorously taking into account the orthogonality relationship between the different eigenvectors. In fact:

$$\boldsymbol{u}_1 = \mathbf{R}\left(\phi_1, \Upsilon_1, \beta_{c_1}, \alpha_1\right) \begin{bmatrix} 1 \\ 0 \\ 0 \end{bmatrix} \text{ and } \boldsymbol{u}_1^H \boldsymbol{u}_2 = 0 \Rightarrow$$

$$\mathbf{R^{-1}}\left(\phi_1, \Upsilon_1, \beta_{c_1}, \alpha_1\right)\boldsymbol{u}_2 = \begin{bmatrix} 0 \\ a \\ b \end{bmatrix} = \mathbf{R}(\xi, \epsilon) \begin{bmatrix} 0 \\ 1 \\ 0 \end{bmatrix} \quad [2.60]$$

and, of course, $\boldsymbol{R^{-1}}(\xi, \epsilon)\boldsymbol{R^{-1}}\left(\phi_1, \Upsilon_1, \beta_{c_1}, \alpha_1\right)\boldsymbol{u}_3 = [0\ 0\ 1]^T$, which shows that the third eigenvector, orthogonal to the first two, does not provide any information. The parameter ϵ measures the predictability of the second eigenvector scattering mechanism from the first one and ξ is a mutual orientation parameter. We can illustrate ϵ by noting that in case of an environment with a reflection symmetry, we have by definition $\alpha_2 = \frac{\pi}{2} - \alpha_1$, and in that case $\epsilon = 0$. This decomposition approach is suitable as its parameters are rotationally invariant and the technique takes into account the orthogonality conditions of the eigenvectors, that is to say it only uses a minimum number of real parameters to describe the covariance matrix: four angular coefficients for the first eigenvector, two terms to describe the second eigenvector according to the first one, and three eigenvalues, so a set

of nine real parameters, equivalent to DoF($\boldsymbol{T}$). An application example of that technique is given in Figure 2.24.

Many polarimetric decomposition approaches, based on mathematical considerations or specific perspectives of physical interpretation, may be found in [LEE 08].

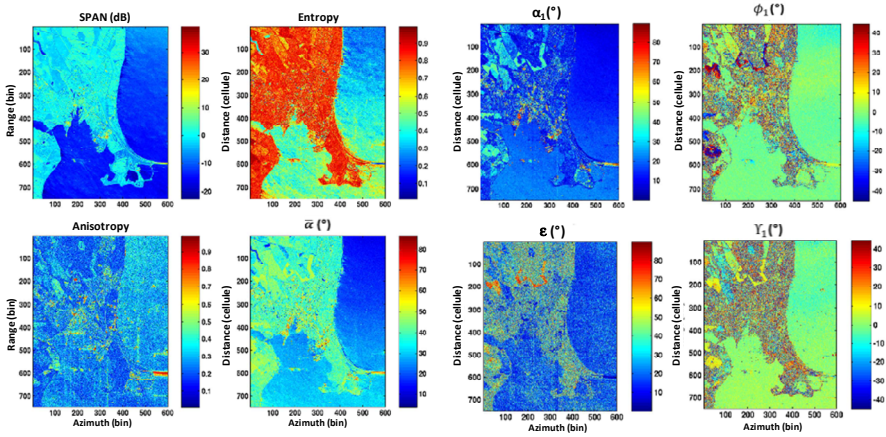

Figure 2.24. *Parameters of decompositions into "classic" and "generalized" eigen-elements on a polarimetric image acquired in the C-band by the DDRE/EmiSAR sensor in the Nyborg port area (Denmark)*

2.2.3.2. *Statistical classification of the polarimetric SAR images*

Though based on the analysis of 2nd order multivariate moments through the covariance matrix, the polarimetric characterization approaches presented so far do not explicitly use the statistical laws of polarimetric quantities. The consideration of that type of information can be extremely useful, in particular to gather image pixels with a similar polarimetric behavior. This allows us to better estimate or classify underlying scattering mechanisms, or to jointly use the polarimetric information, based on the study of the relative amplitudes and phases of the various channels, and the one linked to radiometry, through span, which plays a leading role in differentiating various environments.

2.2.3.2.1. Iterative ML polarimetric classification

The segmentation of a polarimetric SAR image into a set of statistically homogeneous groups aims at assigning, according to a given optimality criterion, the SAR image pixel, p, to one of the possible M groups or segments $\{C_1, \ldots, C_m\}$ according to the polarimetric response $\boldsymbol{k}$ measured for the pixel p. A solution to this optimization problem, which minimizes the error probability, is given by the decision called the *maximum a posteriori* (MAP):

$$\text{Decide } p \in C_i \text{ if } P(C_i|\boldsymbol{k}) > P\left(C_j\middle|\boldsymbol{k}\right)\forall j \neq i \qquad [2.61]$$

where $P(C_i|\boldsymbol{k})$ is the *a posteriori* probability, that is after measuring $\boldsymbol{k}$, of the segment C_i. A pixel is then allocated to the most likely segment after measuring its polarimetric response. As the *a posteriori* probabilities mentioned in [2.61] generally have expressions which are hard to determine, we use the Bayes rule, which when coupled with the assumption of the *a priori* equiprobable segment, i.e. $P(C_i) = \frac{1}{M}\ \forall\, i$, leads to the so-called maximum likelihood (ML) decision rate:

$$\text{Decide } p \in C_i \text{ if } f_{\boldsymbol{k}}(\mathbf{k}|C_i) > f_{\boldsymbol{k}}(\mathbf{k}|C_j)\forall j \neq i \qquad [2.62]$$

where $f_{\boldsymbol{k}}(\boldsymbol{k}|C_i)$ is called the likelihood, whose estimation requires us to estimate the statistics of the members of the segment C_i. Thus, the optimal ML classification solution consists in finding the distribution of the different image pixels on the M segments, which maximizes a global likelihood criterion formed from the likelihoods of the different measurements. Rigorously solving this combinatorial optimization problem requires significant computing power, suboptimal techniques such as the *k-means* algorithm [FER 01b, LEE 99, LEE 01, LEE 04] are generally preferred. This aims at iteratively optimizing the global likelihood, and may be summarized, in the polarimetric case, as follows. We suppose that we have, at the n^{th} iteration of the algorithm, a segmentation map temporarily allocating each image pixel to one of the M segments $\{C_1^n, \ldots, C_m^n\}$. Assuming responses are affected by the speckle effect, the likelihood of L realizations of the pixel p response, $f\left(\boldsymbol{k}_p(1), \ldots, \boldsymbol{k}_p(L)\middle|C_i\right)$ or $f\left(\widehat{\boldsymbol{T}}_p\middle|C_i\right)$ with $\widehat{\boldsymbol{T}}_p = \frac{1}{L}\sum_{l=1}^{L} \boldsymbol{k}_p(l)\boldsymbol{k}_p^H(l)$ can be obtained from [2.21] as:

$$f\left(\widehat{\boldsymbol{T}}_p\middle|C_i^n\right) \approx f\left(\widehat{\boldsymbol{T}}_p\middle|\widehat{\boldsymbol{\Sigma}}_{i_n}\right) = \frac{L^{qL}\left|\widehat{\boldsymbol{T}}_p\right|^{L-q+1}}{\tilde{\Gamma}_{q-1}(L)\left|\widehat{\boldsymbol{\Sigma}}_{i_n}\right|^{L}} e^{-Ltr\left(\widehat{\boldsymbol{\Sigma}}_{i_n}{}^{-1}\widehat{\boldsymbol{T}}_p\right)}$$

$$\text{with } \widehat{\boldsymbol{\Sigma}}_{i_n} = \frac{1}{N_{p_i}}\sum_{p\in C_i^n} \widehat{\boldsymbol{T}}_p \qquad [2.63]$$

where $\widehat{\boldsymbol{\Sigma}}_{i_n}$ represents the centre of class C_i at the n^{th} iteration; i.e. the covariance matrix barycentre of the filtered matrices $\widehat{\boldsymbol{T}}_p$ of the pixels $p \in C_i^n$. By using log-likelihoods and by ignoring terms not involved in the decision process, we obtain the following decision ML rule:

$$\text{Deciding } p \in C_i^{n+1} \text{ if } \mathcal{L}\left(\widehat{\boldsymbol{\Sigma}}_{i_n}, \widehat{\boldsymbol{T}}_p\right) < L\left(\widehat{\boldsymbol{\Sigma}}_{j_n}, \widehat{\boldsymbol{T}}_p\right)$$

$$\text{with } \mathcal{L}\left(\widehat{\boldsymbol{\Sigma}}_{i_n}, \widehat{\boldsymbol{T}}_p\right) = log\,|\widehat{\boldsymbol{\Sigma}}_{i_n}| + \text{tr}(\widehat{\boldsymbol{\Sigma}}_{i_n}^{-1}\widehat{\boldsymbol{T}}_p) \qquad [2.64]$$

where $\mathcal{L}\left(\widehat{\boldsymbol{\Sigma}}_{i_n}, \widehat{\boldsymbol{T}}_p\right)$ represents a concentrated log-likelihood, i.e. within which elements not dependent on $\widehat{\boldsymbol{\Sigma}}_{i_n}$ are removed. The synoptics of the k-means segmentation algorithm adapted to polarimetric data is given in Figure 2.25.

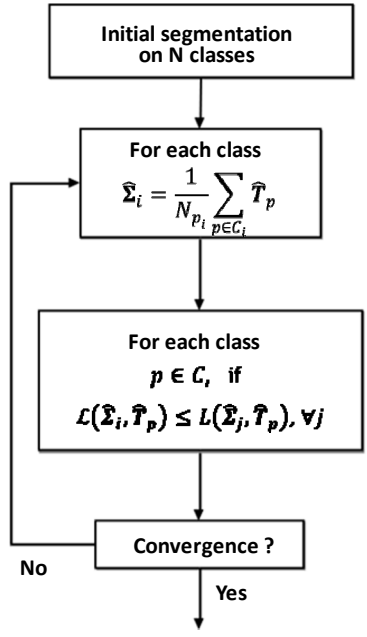

Figure 2.25. *Synopsis of the ML classification of multi-look polarimetric data, based on the k-means technique*

The results shown in Figure 2.26 confirm the relevance of the classification approach to separate the specific scattering mechanisms.

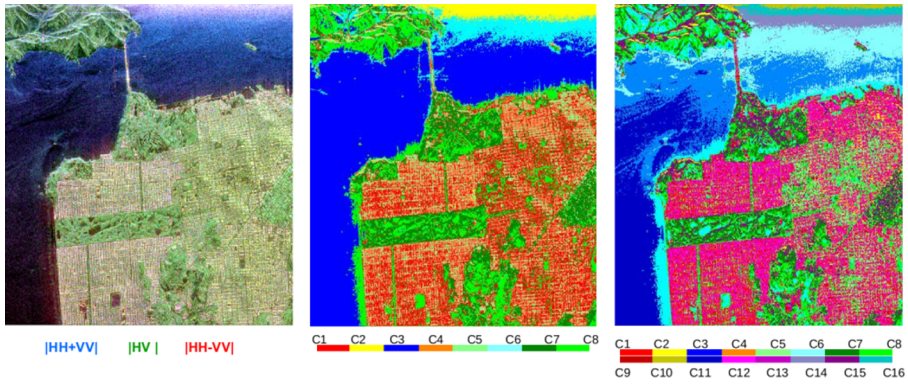

Figure 2.26. *Unsupervised polarimetric segmentation results for the image of the San Francisco Bay using 8 or 16 classes. For a color version of this figure, see www.iste.co.uk/baghdadi/2.zip*

2.2.3.2.2. ML polarimetric classification respecting the nature of scattering mechanism

This is a variant of the iterative k-means algorithm, which has been known to give an excessive importance to the radiometric aspect of the polarimetric response, through the span; which plays a leading role in the decision rate of [2.64]. As a consequence, pixels with different scattering mechanisms, but with similar radiometry, may fall within the same segment. To place a greater emphasis on polarimetric information in the classification process, it was suggested in [LEE 02a] to split the image, before the statistical segmentation, into three classes by means of the Freeman–Durden decomposition. Each class is then separately segmented, through k-means procedures, thus avoiding mixing the different polarimetric behaviors during the iterative process. A classification example is given in Figure 2.27.

2.2.3.3. *Advanced characterization of scattering mechanisms*

2.2.3.3.1. Estimation of rough surface geophysical properties

Estimation of a scene azimuthal topography

The orientation of an imaged object around the radar line of sight plays a significant role in radar polarimetry. It is indeed possible to measure the azimuthal orientation of environments whose polarimetric response shows a moderate entropy, satisfying the reflection symmetry conditions for an

orientation parallel to the horizontal, as was shown in [LEE 02b]. The covariance matrix expressed in the circular basis, after an azimuthal rotation is given by [2.57] as:

$$\boldsymbol{C}_{rl}(\phi) = \boldsymbol{U}_{C_{rl}}(\phi)\boldsymbol{C}_{rl}\boldsymbol{U}_{C_{rl}}(\phi) = \begin{bmatrix} \boldsymbol{C}_{rl}(1,1) & \boldsymbol{C}_{rl}(1,2)\mathrm{e}^{-j2\phi} & \boldsymbol{C}_{rl}(1,3)\mathrm{e}^{-j4\phi} \\ \boldsymbol{C}_{rl}(2,1)\mathrm{e}^{+j2\phi} & \boldsymbol{C}_{rl}(2,2) & \boldsymbol{C}_{rl}(2,3)\mathrm{e}^{-j2\phi} \\ \boldsymbol{C}_{rl}(3,1)\mathrm{e}^{+j4\phi} & \boldsymbol{C}_{rl}(3,2)\mathrm{e}^{+j2\phi} & \boldsymbol{C}_{rl}(3,3) \end{bmatrix} \quad [2.65]$$

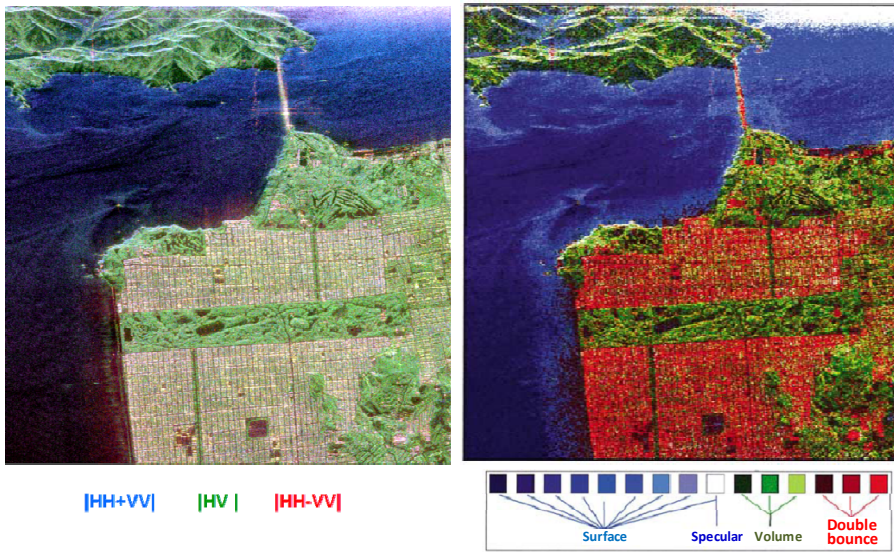

Figure 2.27. *Illustration of the polarimetric segmentation preserving the scattering mechanism nature on the AirSAR image of San Francisco*

This expression shows that the azimuthal orientation modifies the argument of the three intercorrelation coefficients, i.e. the off-diagonal elements, it can in practice only be estimated from a single one, as $\boldsymbol{C}_{rl}(1,2)$ and $\boldsymbol{C}_{rl}(2,3)$ generally have complex values, whereas, in case of a horizontal natural environment, we have $\left(S_{pp}S_{pq}^{*}\right) = 0 \Rightarrow \boldsymbol{C}_{rl}(1,3) \in \mathbb{R}$, which makes it possible to easily estimate ϕ from $\boldsymbol{C}_{rl}(\phi)(1,3)$. Examples of estimation of azimuthal slopes are given in Figure 2.28 for surfaces not covered by vegetation, observed in the L-band or oceanic scenes measured in the P-band. The comparison of continental azimuthal slopes obtained with

a digital elevation model (DEM), shows that the polarimetric approach allows us to estimate the main land relief characteristics, when the polarimetric response is not dominated by the volume component. However, this topographical characterization approach cannot be compared with dedicated means or techniques, like LiDAR and SAR interferometry. In fact, the polarimetric estimates are generally affected by significant noise and ambiguities, and do not provide sufficient information to reconstruct an elevation profile, even mono-dimensional, without any assumption as to the scene range topography. The second result indicated in Figure 2.28 shows the potential of polarimetric SAR processing for measuring marine currents, an application for which very few remote sensing means can be considered as really adapted.

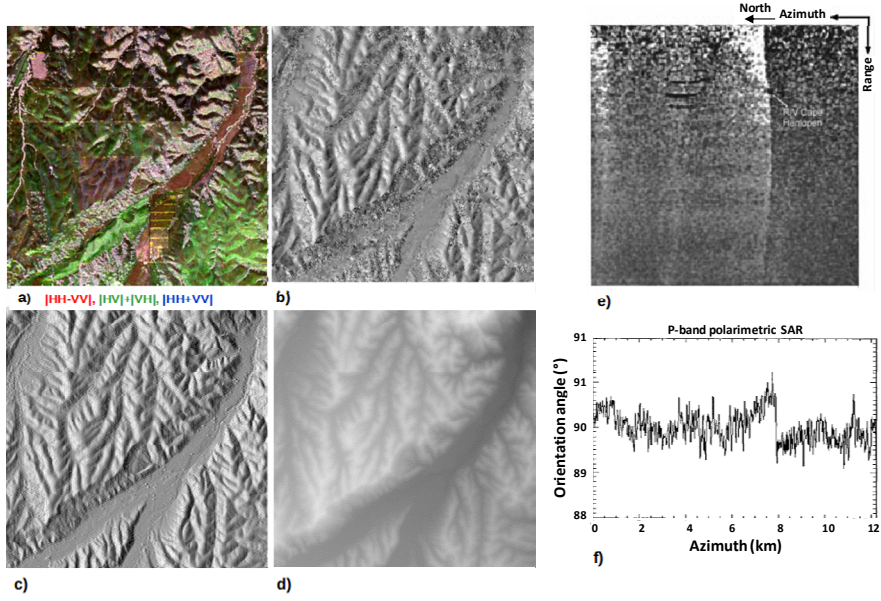

Figure 2.28. *Estimation of azimuthal slopes by means of the polarimetric azimuthal orientation angle, ϕ. a) Polarimetric image of the Camp Roberts site acquired in the L-band by the JPL/AirSAR sensor, b) estimated values of ϕ, c) values of ϕ simulated from a DEM estimated in the C-band, d) a DEM estimated in the C-band [LEE 02b], e) values of ϕ estimated by the same sensor in the P-band, of the Gulf Stream oceanic current, f) orientation angle profile [LEE 98]. For a color version of this figure, see www.iste.co.uk/baghdadi/2.zip*

Soil characterization by means of the $H, A, \bar{\alpha}$ parameters and of the SPM model

Due to the close link between the polarimetric response of soils and some of its geophysical properties, SAR polarimetry has often been used to estimate, on a large scale, the roughness and moisture of natural surfaces. Among the various approaches mentioned in the literature, the one developed in [HAJ 03], directly uses the parameters $H, A, \bar{\alpha}$, derived from the eigen-decomposition technique of [CLO 97], as well as the small perturbation model (SPM) EM scattering model [FUN 94]. This 1st order model makes it possible to very easily simulate the polarimetric response of a moderately rough surface, as:

$$\mathbf{T}_{SPM}(\kappa_c\sigma, W, \theta, \epsilon_r) = m_s^2(\kappa_c\sigma, W)\boldsymbol{T}_0(\theta, \epsilon_r) \qquad [2.66]$$

where $\kappa_c = \frac{2\pi}{\lambda_c}$ is the wave number of the carrier used, σ is the standard deviation of the soil surface heights, modeled here under the form of a random process, whose power spectral density, W, is given by the Fourier transform of its autocorrelation function. The incidence angle, in range, is denoted by θ and ϵ_r represents the soil relative dielectric permittivity. This 1st order modeling technique offers a formulation that separates the influences of the soil roughness and moisture from the global response. Roughness modulates, through the scalar function $m_s^2(\kappa_c\sigma, W)$, the overall response, and does not modify polarimetric characteristics, whereas moisture is considered through ϵ_r, which intervenes in $\boldsymbol{T}_0(\theta, \epsilon_r)$. The global covariance matrix has a zero intensity cross-polarization term, $\boldsymbol{T}_{SPM}(3,3) = 0$, and perfectly correlated co-polarized channels, which provides a unit rank and a zero entropy, very different from the values generally observed on real data, in the L- and C-bands. A solution to that limitation is suggested in [HAJ 03], which consists in introducing some degree of depolarization in the SPM model through a rotation of $\boldsymbol{T}_{SPM}$ around the radar viewing axis:

$$\mathbf{T}(\Delta\psi) = \int_{-\frac{\pi}{2}}^{\frac{\pi}{2}} \mathbf{U}_{3T}(\phi)\mathbf{T}_{SPM}(\kappa_c\sigma, W, \theta, \epsilon_r)\boldsymbol{U}_{3T}^H(\phi) f_\psi(\phi)\, \mathrm{d}\phi \qquad [2.67]$$

with $f_\psi(\phi)$, a uniform probability density centered around 0 and with a width $\Delta\psi$. The aforementioned eigen-decomposition is then applied to $\boldsymbol{T}(\Delta\psi)$, to produce $H(\Delta\psi), \bar{\alpha}(\Delta\psi), A(\Delta\psi)$, whose simulated values, shown in Figure 2.29, indicate that ϵ_r can be estimated from $H(\Delta\psi)$ and $\alpha(\Delta\psi)$,

whereas the simulated anisotropy, $A(\Delta\psi)$, is not at all correlated with $\bar{\alpha}(\Delta\psi)$.

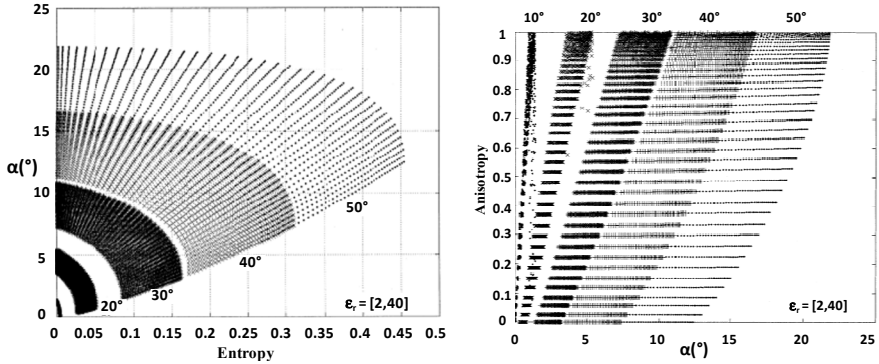

Figure 2.29. *Geometrical locations covered by the polarimetric parameters of $\boldsymbol{T}(\Delta\psi)$, simulated according to Hajnsek et al. [HAJ 03] for $\theta = (10,20,30,40,50)[deg]$ and $\epsilon_r \in [2,40]$, in the a) $H(\Delta\psi) - \bar{\alpha}(\Delta\psi)$, b) $A(\Delta\psi) - \bar{\alpha}(\Delta\psi)$ planes*

In their studies, Hajnsek *et al.* [HAJ 03] linked the measured anisotropy with a roughness characteristic, through the empirical relationship $A = 1 - \kappa_c\sigma$. Soil moisture indicators, like the volume water content, can then be estimated from ϵ_r.

Soil characterization by means of the IEM model, taking into account the reflection symmetry

Another technique, introduced in [ALL 04, ALL 05a], suggests an alternative approach which does not require an arbitrary azimuthal disorientation and uses the integral equation model (IEM) [FUN 94, CHE 03]. In the case, always verified over rough surfaces, of a polarimetric response showing a reflection symmetry, we can give a simple analytical expression of the unsorted eigenvalues of the covariance matrix [ALL 05b] may be given:

$$\begin{aligned}
\lambda_{1_{nos}} &= \frac{E(|S_{hh}|^2+|S_{vv}|^2)+\sqrt{E(|S_{hh}|^2+|S_{vv}|^2)^2+4E(|S_{hh}|^2)}}{2} \\
\lambda_{2_{nos}} &= \frac{E(|S_{hh}|^2+|S_{vv}|^2)-\sqrt{E(|S_{hh}|^2+|S_{vv}|^2)^2+4E(|S_{hh}|^2)}}{2} \\
\lambda_{3_{nos}} &= E(|S_{hv}|^2)
\end{aligned} \qquad [2.68]$$

The eigenvalues given in [2.68] are not sorted, even if $\lambda_{1_{nos}} \geq \lambda_{2_{nos}}$, and that they can be defined exactly through the span and two real parameters, for example, the relative differences of the simple (SERD) and double (DERD) reflections, defined in [ALL 05b]. The reflection symmetry property, implies that, the eigenvectors associated with $\lambda_{1_{nos}}$ and $\lambda_{2_{nos}}$ only contain reduced information of the associated scattering mechanisms, with $\alpha_2 = \frac{\pi}{2} - \alpha_1$. In fact, when the assumption of the symmetry reflection is verified, a fully polarimetric covariance matrix can be defined with the help of $\lambda_{i_{nos}}$ and a two-complex element unit vector, sufficient to construct $\boldsymbol{v}_1$, orthogonal to $\boldsymbol{v}_2$. That information redundancy gives the average parameters defined by [CLO 96], and to $\bar{\alpha}$ in particular, a highly biased nature, which can undermine the estimation of physical parameters and even the identification of scattering mechanisms [FER 03]. The approach of [ALL 05b] uses a reduced set of parameters, composed of α_S, SERD and DERD, defined as:

$$SERD = \frac{\lambda_S - \lambda_{3nos}}{\lambda_S + \lambda_{3nos}} \text{ and } DERD = \frac{\lambda_D - \lambda_{3nos}}{\lambda_D + \lambda_{3nos}} \quad [2.69]$$

where $\lambda_{S,D} = \lambda_{i,j}$ with i such as $\alpha_i \leq \frac{\pi}{4}$, $i = 1$ or 2 and $j = 3 - i$. Due to their dented range of variation and the possibilities of interpretation given by their analytical expression, SERD and DERD cover a domain more significant than the anisotropy, with $-1 \leq SERD, DERD \leq 1$. The DERD parameter can be compared with the anisotropy, whereas the SERD proves to be particularly useful in case of a high entropy. The method to characterize the soils introduced in [ALL 04, ALL 05b] uses the IEM for higher orders, which generally takes into account the depolarization phenomenon and allows us to obtain a covariance matrix revealing a reflection symmetry. In Figure 2.30, the anisotropy and DERD obtained by means of the IEM for different soil configurations are compared.

If the link between the anisotropy and some roughness descriptors is verified by the IEM, the use of identified rather than sorted eigenvalues helps to free the anisotropy of its significant ambiguity, by giving the DERD parameter a more extended and non-ambiguous definition domain. Similar conclusions were obtained from measurements taken at the European laboratory JRC of Ispra, in Italy, whose results are shown in Figure 2.31.

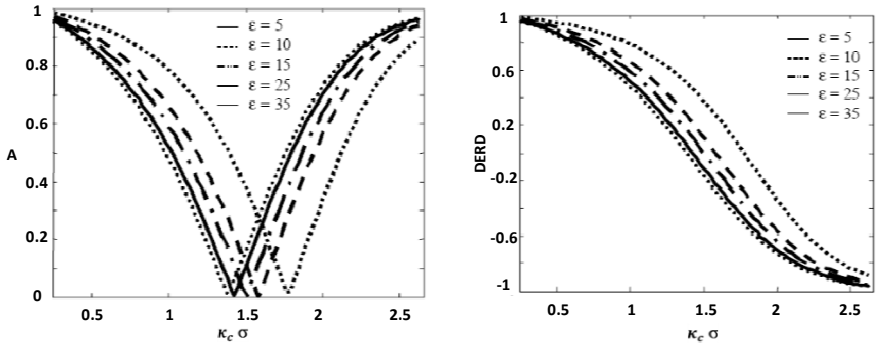

Figure 2.30. *Simulation result of the EM response over rough soil by means of the IEM model, for different field conditions and as a function of $k\sigma$: a) anisotropy (A); b) DERD*

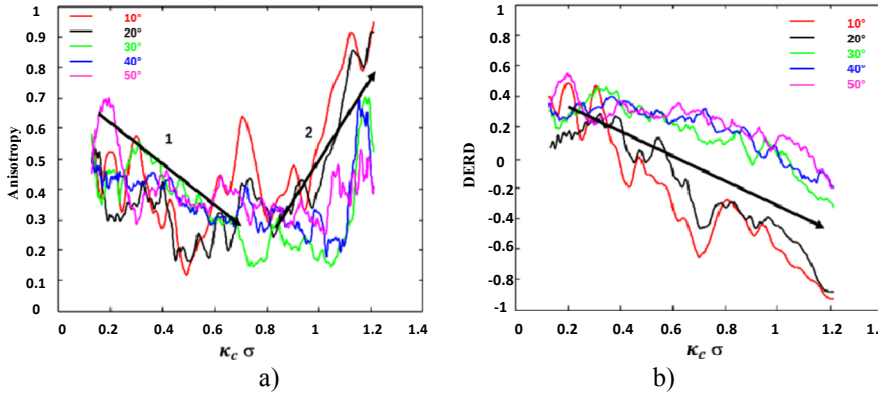

Figure 2.31. *Polarimetric parameter values derived from measurement taken at the European laboratory JRC, as a function of $k\sigma$: a) anisotropy; b) DERD. For a color version of this figure, see www.iste.co.uk/baghdadi/2.zip*

The use of the α_S parameter instead of $\bar{\alpha}$ to estimate ϵ_r allows us to avoid a significant bias, which cannot be avoided by the joint use of $\bar{\alpha}$ and H. The results obtained using data measured by an airborne SAR sensor are shown in Figure 2.32.

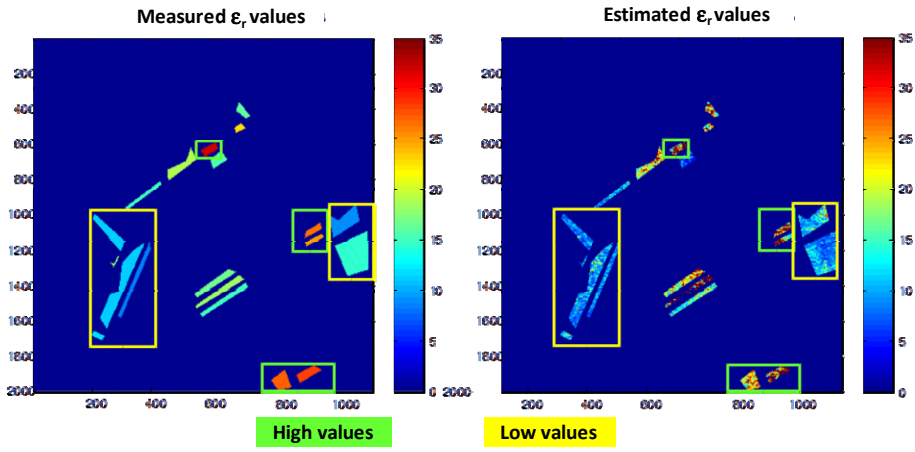

Figure 2.32. *Dielectric permittivity estimation over agricultural fields from polarimetric data acquired in L-band by the ESAR sensor of the DLR and the technique proposed in [ALL 05b]. For a color version of this figure, see www.iste.co.uk/baghdadi/2.zip*

2.3. An introduction to SAR interferometry and tomography

2.3.1. *Principle of topography measurement through the SAR interferometry*

SAR imaging uses spectral and spatial diversity, to focus a 2D image of an environment EM response, which can be expressed as:

$$s(x,r) = \int_{-\infty}^{+\infty}\int_{-\infty}^{+\infty} a_c(x',r')\, e^{-jk_c r'} h_{ar}(x-x', r-r')\mathrm{d}x'\mathrm{d}r' \quad [2.70]$$

where $h_{ar}(x-x', r-r')$ represents the focused response of a punctual scatterer with coordinates (x', r'), and $a_c(x', r')$ is the projection of the 3D reflectivity density of an environment in the range-azimuth domain. As was shown in Figure 2.33, the reduction of the representation domain to two dimensions leads to a cylindrical ambiguity: for a given position in azimuth x_0, there is an infinity of coordinates y, z leading to the same focusing position in range $r_1 = \sqrt{(H-z)^2 + y^2}$.

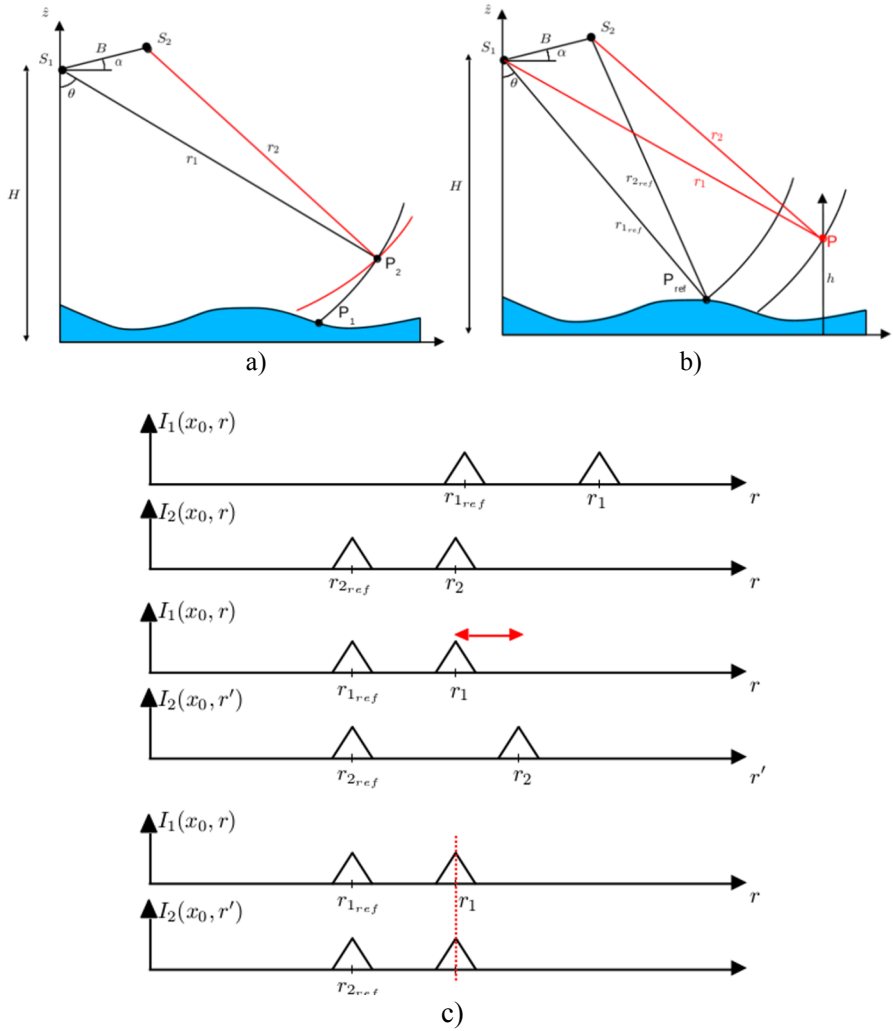

Figure 2.33. *Principle of the estimation of a scatterer position in elevation using coherent spatial diversity: a) the location P is the only intersection solution for circles with r_1 and r_2; b) representation of the signals acquired by each sensor before and after co-registration in relation to a reference point P_{ref}*

Spatial diversity is set up with a second measurement taken from a slightly different position, parameterized by a distance, the baseline *B*, and

an orientation angle α. The imaged scatterer position y_0, z_0 is then given by the intersection of two circles, whose radiuses, r_1 and r_2, must be measured with high accuracy. From the expression of the focused response of a point-like scatterer, given by:

$$s_i(x_0, r_i) = a_{c_i} e^{-jk_c r_i} h_{ar}(0, r_i - r_0) = |a_{c_i}| h_{ar}(0, r_i - r_0) e^{j(\xi_i - k_c r_i)} \quad [2.71]$$

with $\xi_i = \arg(a_{c_i})$

we note that the radiuses r_i can be incoherently measured, by radargrammetry using $|s_i(x_0, r_i)|$, or coherently measured by using $arg\,(s_i(x_0, r_i))$ through interferometry. As shown in Figure 2.34, the selection of a method depends on various factors and in particular on the amplitude of the shifts generated by the scene topography. These shifts may be measured by synchronizing the two images on an arbitrary geometry, during a "co-registration" phase: image 2, called "slave", is resampled so that each of its pixels corresponds, for a nominal scene geometry, to its equivalent in image 1, called "master". Once the images are synchronized, the appearance of a shift indicates that the real scene geometry is different from the one used to co-register the images. Radargrammetry, suitable for large shifts, estimates $\Delta r_{12} = r_1 - r_2$ with an accuracy similar to the range resolution δr, whereas interferometry, suitable for the estimation of small shifts, has an accuracy in the range of $\lambda_c \ll \delta r$. Assuming a perfect speckle correlation between the two SAR measurements, the interferometric phase difference, or interferogram, is given by:

$$\text{if } \xi_1 = \xi_2, \text{ then } \Delta\phi_{12} = arg(s_1 s_2^*) = -k_c \Delta r_{12} \quad [2.72]$$

As shown in Figure 2.34b, that phase term can be approximated, by a locally plane wave, if $r_1 \gg B$, by [BAM 98]; as:

$$\Delta\phi_{12} = -k_c \Delta r_{12} \approx -k_c B \sin(\theta - \alpha) = -k_c B_{\parallel} \quad [2.73]$$

We then see in [2.73] that $\Delta\phi_{12}$ is indeed linked to the scene topography, h, through $\theta = \text{acos}\left(\frac{H-h}{r_1}\right)$, but also depends on the considered range position r_1 (Figure 2.35).

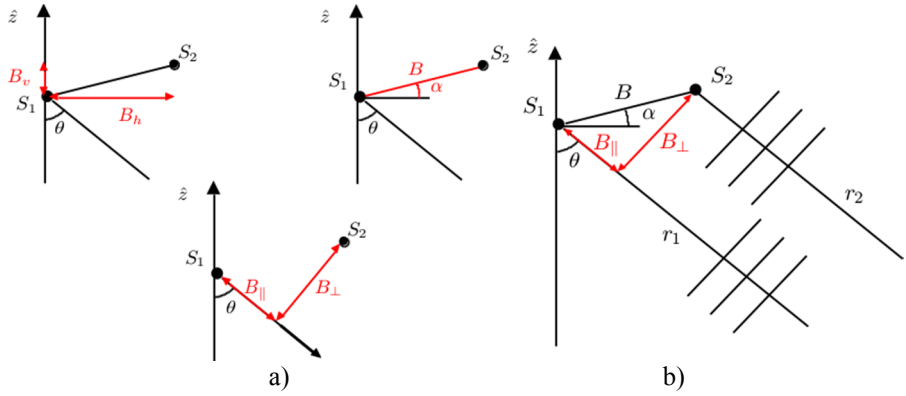

Figure 2.34. *a) Parameterization of the relative positions of measurements in InSAR configuration in a Cartesian (B_h, B_v), polar (B, α), or wave $(B_\parallel, B_\perp)$ coordinate system; b) illustration of a locally plane wave approximation*

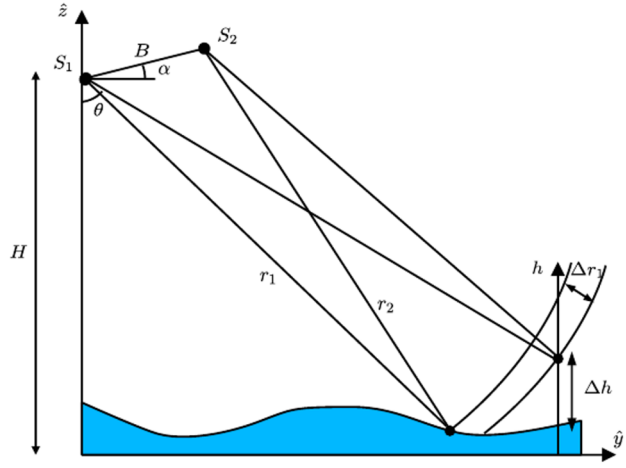

Figure 2.35. *Illustration of the dependence of Δr_{12} on a variation of the position in elevation Δh or in range Δr*

Those two behaviors can be separated by means of a linearization, valid in the neighborhood of a reference point with coordinate (r_{0_1}, z_0) [FER 07]:

$$\Delta\Delta\phi_{12} = \Delta\phi_{12} - \Delta\phi_{12_0} \approx \Delta\Delta\phi_{topo} + \Delta\Delta\phi_{fe} = k_{z_0} h_{rel} + k_{fe} r_{rel} \quad [2.74]$$

where $\Delta\Delta\phi_{topo}$ represents the increase of the topographic component of $\Delta\phi_{12}$, sensitive to an elevation variation $h_{rel} = z - z_0$ relative to the one of the reference point, and $\Delta\Delta\phi_{fe}$ is the "flat earth" component, which takes into account the variation of Δr_{12} with $r_{rel} = r_1 - r_{0_1}$ for a site with a flat topography. The height-to-phase conversion coefficients k_{z_0} and k_{fe} are determined by the acquisition geometry, as:

$$k_{z_0} = -k_c \frac{B_\perp}{r_{0_1} sin\theta_{0_1}} \text{ and } k_{fe} = -k_c \frac{B_\perp}{r_{0_1} tan\, \theta_{0_1}} \quad [2.75]$$

where θ_{0_1} and $B_\perp$, respectively, represent the incidence angle and the orthogonal baseline, in the image co-registration geometry, at the considered reference point. The relative topographic component of an interferogram can then be obtained through the simple compensation of the flat earth component. Before converting the phase measured in height using [2.74], the topographic phase, generally needs to be unwrapped, since $k_{z_0} h_{rel}$, can only be measured on a reduced domain, with $-\pi \leq \Delta\Delta\phi_{12} < \pi$. The elevation domain that can be measured without phase aliasing is called the ambiguous height or the height ambiguity, and is given by $h_{amb} = \frac{2\pi}{|k_z|} = \frac{2\pi r_{0_1} sin\theta_{0_1}}{k_c B_\perp}$. For relative elevations superior to h_{amb}, the estimation of the scene topography from the interferometric phase requires the developement of a phase unwrapping procedure, whose principle is illustrated in Figure 2.36 [FER 07].

An example of interferometric SAR data processing chain is given in Figure 2.37.

2.3.2. *Polarimetric SAR interferometry*

Similarly to the case of polarimetric data, the practical estimation of the interferometric phase information requires the use of second order moments through the covariance matrix that can be expressed from $\boldsymbol{s} = [s_1 s_2]^T$ as:

$$\mathbf{C} = \mathrm{E}(\boldsymbol{s}\boldsymbol{s}^H) = \begin{bmatrix} \sqrt{I_1} & 0 \\ 0 & \sqrt{I_2} \end{bmatrix} \begin{bmatrix} 1 & \gamma \\ \gamma^* & 1 \end{bmatrix} \begin{bmatrix} \sqrt{I_1} & 0 \\ 0 & \sqrt{I_2} \end{bmatrix} \text{ with } \gamma = |\gamma| e^{j\phi} \quad [2.76]$$

where γ is called the interferometric coherence and is a quality indicator of the interferometric phase. It may be shown this coherence can be written

under the form of a product of various components, associated with decorrelation sources, as:

$$\gamma = \gamma_{SNR}\gamma_{proc}\gamma_{temp}\gamma_{surf}\gamma_z \text{ with } |\gamma| \leq \min(|\gamma_i|) \quad [2.77]$$

where the different terms, respectively, represent the action of the signal/noise ratio (SNR), of the focusing processing errors, of the scene reflectivity density variations between the two measurements, of the scene geometry and, finally, of the reflectivity density distribution in the vertical direction. The interferometric coherence notion is illustrated in Figure 2.38.

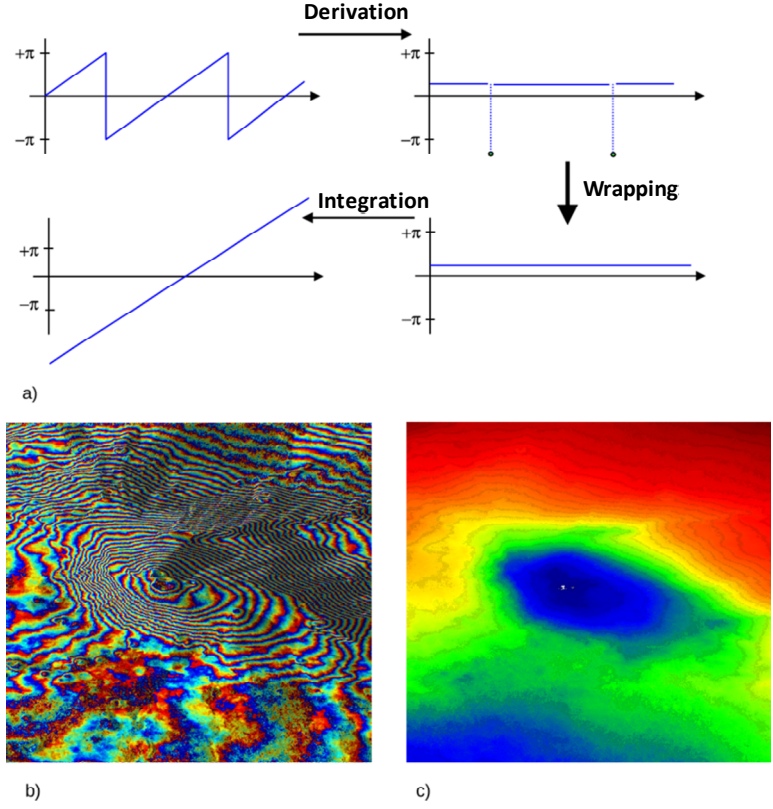

Figure 2.36. *a) Principle of interferometric phase unwrapping in 1D; b) wrapped interferometric phase measured during the SIR-C XSAR campaign, a color cycle corresponds to a phase cycle from $-\pi$ to $+\pi$; c) unwrapped phase. For a color version of this figure, see www.iste.co.uk/baghdadi/2.zip*

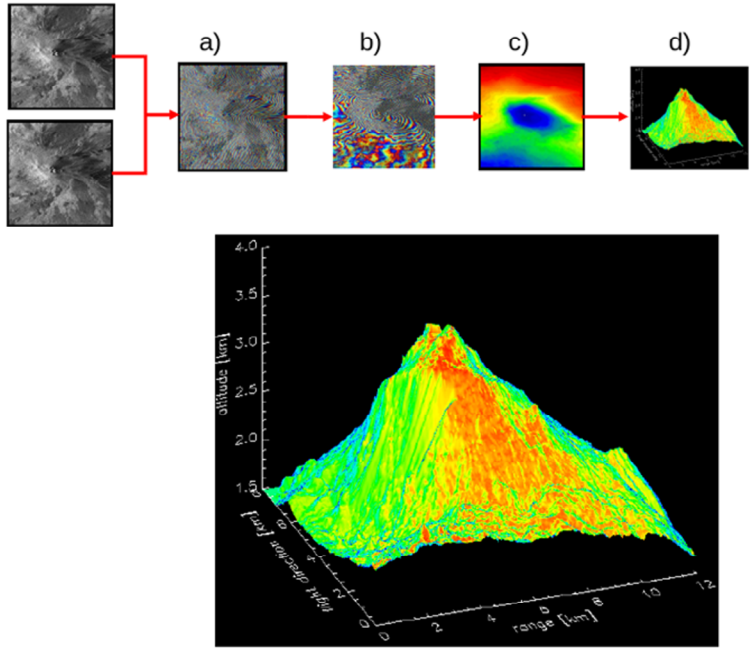

Figure 2.37. *Digital elevation model (DEM) generation of a SAR processing chain: a) formation of the interferogram; b) compensation of the flat earth phase; c) 2D phase unwrapping; d) phase to height conversion before geo-codification. For a color version of this figure, see www.iste.co.uk/baghdadi/2.zip*

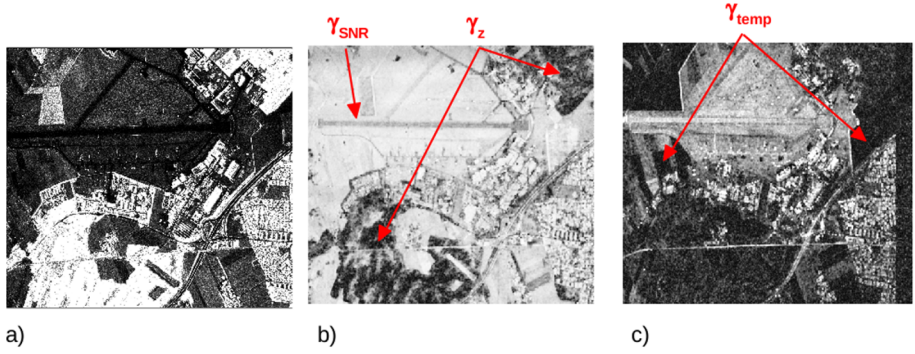

Figure 2.38. *Illustration of the interferometric coherence over the Oberpfaffenhofen site, observed at VV polarization and in L-band by the DLR/ESAR sensor, with indications of the dominant decorrelation phenomena: a) intensity image; b) $|\gamma|$ after 1 h and with $B = 20\ m$; c) $|\gamma|$ after 1 year and with $B = 0\ m$*

Assuming that the other components of γ listed in [2.77] can be compensated and coherence can be used to measure the geophysical properties of a volume, through the expression [BAM 98, TRE 99, TRE 00]:

$$\gamma_z = \frac{\int f(z) e^{jk_z z}\, dz}{\int f(z)\, dz} \qquad [2.78]$$

with $f(z) = \mathrm{E}(a_{c_1}(z) a^*_{c_2}(z))$, the elevation reflectivity density in elevation. Figure 2.39 shows a description of a canonical volume environment often used in radar, called Random Volume Over Ground (RVOG), composed of ground with a reflectivity density $f_g(z) = I_g \delta(z - z_g)$ and a semi-transparent volume with a reflectivity density $f_v(z)$, with $\int f_v(z)\, dz = I_v$.

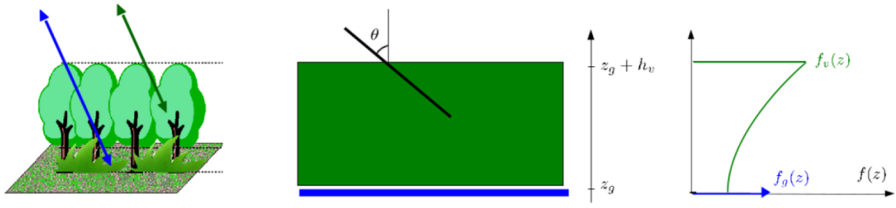

Figure 2.39. *Geometric configuration of the RVOG model and associated reflectivity distributions. For a color version of this figure, see www.iste.co.uk/baghdadi/2.zip*

Figure 2.40 shows the evolution of γ_v, the coherence of the volume term obtained by replacing $f(z)$ with $f_v(z)$ in [2.78], for different volume characteristics: in case of a constant extinction volume, it is possible, for a given extinction value (k_e), to estimate the vertical extent and the volume average elevation.

In practice, the reflectivity density is composed of the ground and volume responses, and the measured coherence is written [CLO 98, CLO 03, PAP 01]:

$$f(z) = f_g(z) + f_v(z) \Rightarrow \gamma_z = \frac{\gamma_v + \mu e^{jk_z z_g}}{1+\mu} \text{ with } \mu = \frac{I_g}{I_v} \qquad [2.79]$$

where μ, the intensity ratio of the ground and volume responses, or Ground to Volume Ratio, is *a priori* unknown, which prevents any reliable

estimation of the volume characteristics. By means of a formalism not presented here, it is possible using polarimetric measurements taken from slightly different positions, to synthesize an interferometric coherence for an arbitrary polarization state $\mathbf{w}$, $\gamma(\mathbf{w})$, which, assuming a volume with an extinction independent from the polarization state of the wave going through it, may be written as:

$$\gamma_z(\mathbf{w}) = \frac{\gamma_v + \mu(\mathbf{w})\, e^{jk_z z_g}}{1+\mu(\mathbf{w})} = (1 - L(\mathbf{w}))\gamma_v + L(\mathbf{w}) e^{jk_z z_g}$$

$$\text{with } L(\mathbf{w}) = \frac{\mu(\mathbf{w})}{1+\mu(\mathbf{w})} \qquad [2.80]$$

where only $\mu(\mathbf{w})$ or $L(\mathbf{w})$ depend on polarization [CLO 98, CLO 03, PAP 01]. We note from [2.80] that coherences obtained for different polarization states show varying phase and correlation values, which depend on the proportion of the ground and volume responses for the considered polarization state. There then is a polarization state close to the ground response for which $\mu(\mathbf{w})$ is maximum, and $\gamma_z(\mathbf{w}) \to \gamma_g = e^{jk_z z_g}$ and another one for which $\mu(\mathbf{w})$ is minimum and $\gamma_z(\mathbf{w}) \to \gamma_{vol}$. This type of relationship results in a coherence which describes, when it is calculated for arbitrary values of $\mathbf{w}$, a line segment in the complex plane, shown in Figure 2.41. Generally, despite the fact that $max_{\mathbf{w}}(\mu(\mathbf{w})) < +\infty$, z_g can still be estimated through the extrapolation of the line segment up to the unit radius circle, that is up to $\gamma_g = e^{jk_z z_g}$ [CLO 98, CLO 03, PAP 01]. As an example, a result obtained by PolinSAR is shown in Figure 2.42.

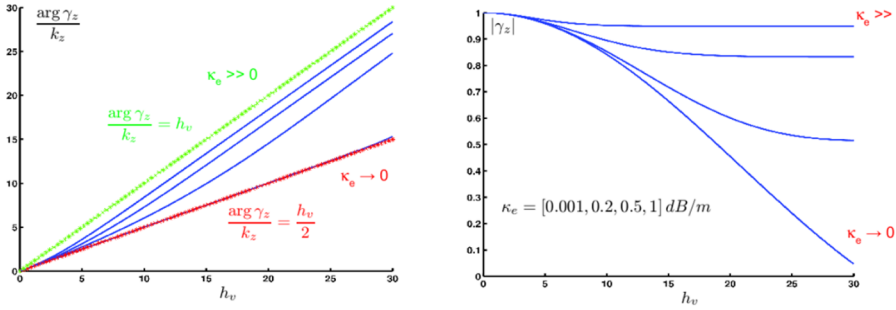

Figure 2.40. *Characteristics of the interferometric coherence for a nulll ground response, $\gamma_z = \gamma_{vol}, for\ k_z = 0.2$ and for a constant extinction volume. For a color version of this figure, see www.iste.co.uk/baghdadi/2.zip*

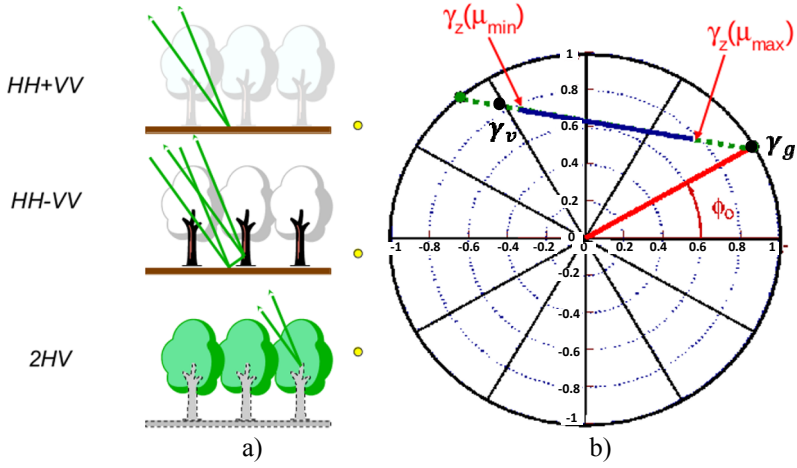

Figure 2.41. *a) Idealized representation of the phase centers obtained in an environment of the RVOG type for different polarization channels; b) geometric location followed by $\gamma_z(\boldsymbol{w})$, the segment extrapolation allows us to estimate $\phi_0 = \phi_g$ with $\mu(\boldsymbol{w}) < +\infty$*

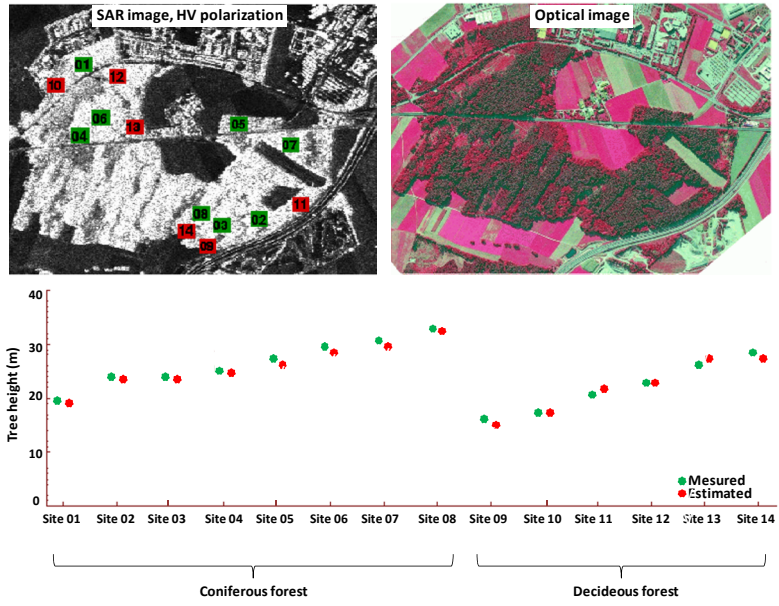

Figure 2.42. *Estimation of forest height results over the Oberpfaffenhofen site, measured in L-band by the DLR/ESAR sensor. Results derived from [PAP 01]. For a color version of this figure, see www.iste.co.uk/baghdadi/2.zip*

2.3.3. *Differential SAR interferometry*

The principle of differential SAR interferometry [FER 01a, GAB 89, MAS 93, ZEB 94], illustrated in Figure 2.43, is particularly simple: a displacement of the area observed occurring between the two SAR measurements of an interferometric pair, results in a phase anomaly, adding to the flat earth or topographic components, and which makes it possible to very accurately measure a topographic deformation. In fact, for a scatterer whose range position changes by Δr between the acquisitions, the interferometric phase is written, after compensating the flat earth term, as:

$$\Delta\Delta\phi_{12} = \Delta\Delta\phi_{topo} + \Delta\Delta\phi_{displ} = k_{z_0} h_{rel} + k_c \Delta r \qquad [2.81]$$

The phase measured can be compensated from its topographic component, through a differential approach using data previously measured or through simulation from a DEM, to isolate the term linked to the ground displacement, $\Delta\Delta\phi_{displ} = k_c \Delta r$.

On the one hand, we note the extreme accuracy of that type of measurement, whose ambiguous displacement is given by $\Delta r_{amb} = \frac{\lambda_c}{2}$, and on the other hand, the independence of that measurement with respect to the used baseline.

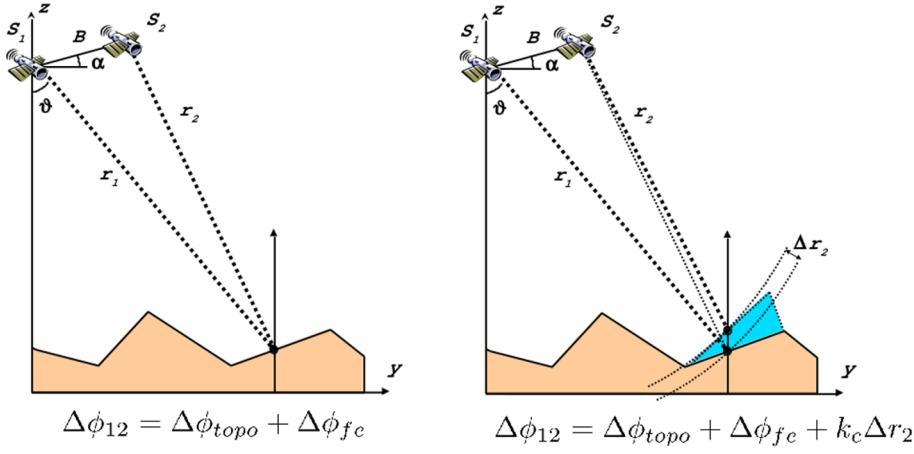

Figure 2.43. *Ground deformation measurement principle using differential SAR interferometry. For a color version of this figure, see www.iste.co.uk/baghdadi/2.zip*

The combination of this type of approach with the permanent scatterer technique allows us to measure displacements ranging from a few mm/year on very long periods, as shown in Figure 2.44.

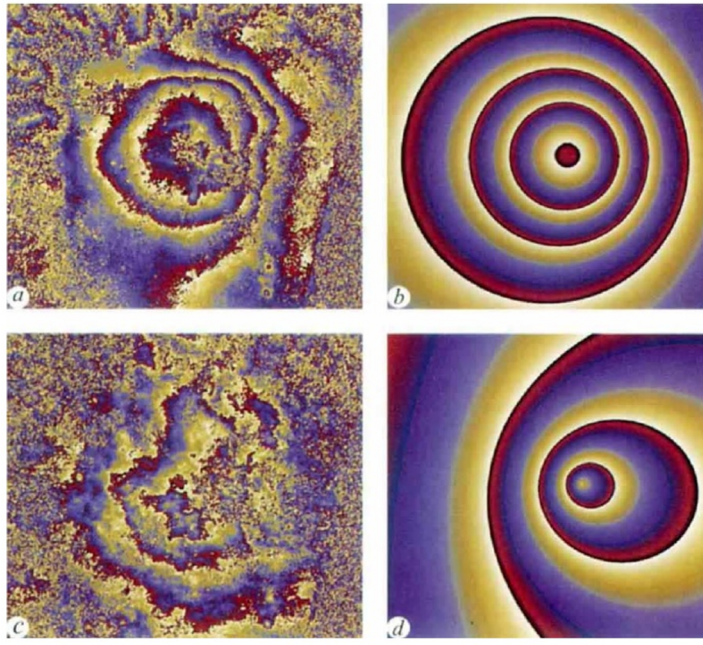

Figure 2.44. *Differential a) and c) measured interferograms; b) and d) modelized on Mount Etna, Italy, for a series of images acquired in C-band by ERS-1 [MAS 95]. For a color version of this figure, see www.iste.co.uk/baghdadi/2.zip*

Differential SAR interferometry is one of the most popular SAR imaging disciplines, due to its very close link with the physical evolution of an environment and its unique aptitude for mapping, on a large scale and at low price, ground movements with extreme accuracy. There are numerous applications of this technique, in particular in the geosciences and geophysics fields; two famous illustrations are shown in Figure 2.45.

The main limitations to the development of differential SAR interferometry concern the management of scene variations observed

and of the propagation conditions. Changes in the effective propagation speed of SAR signals in the atmosphere creates phase patterns, called phase screens, which can be wrongly interpreted as displacements. Scene variations over time create a reduction of the interferometric coherence, which, over the span of several years, can reach values for which the interferometric phase cannot be interpreted. A technique based on the characteristics of some point-like scatterers that remain coherent over time, *permanent scatterers* (PS), has made it possible to overcome those limitations on urban areas [FER 01a, FER 07], as illustrated in Figure 2.46.

a)

b)

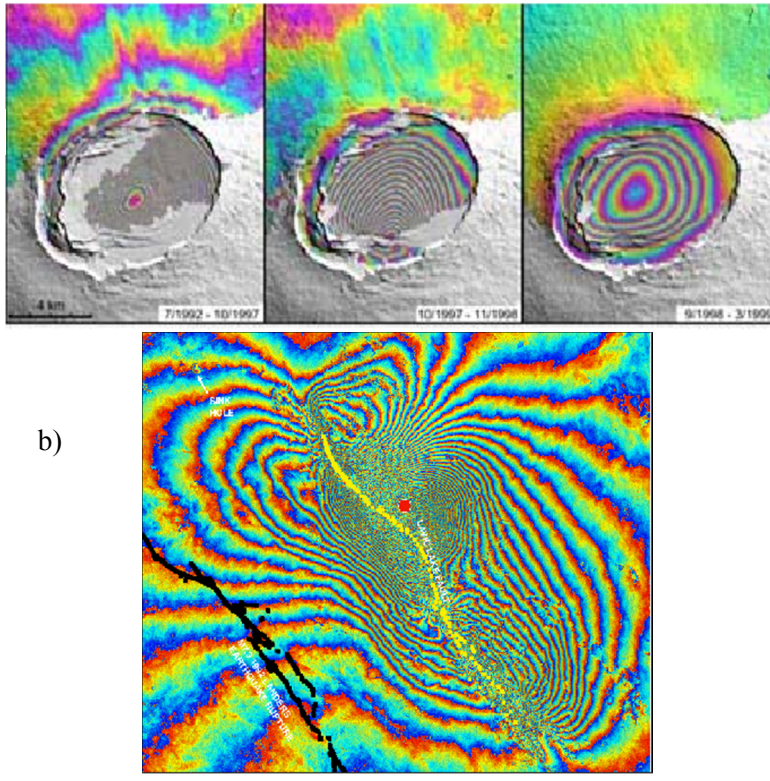

Figure 2.45. *Illustration of the application differential SAR interferometry in C-band in geophysics. a) "Breathing" time deformation visualization of the Galápagos island volcanoes, Equator (each fringe corresponds to a 5 cm radial displacement) [AME 00]; b) differential interferogram caused by the Hector mine earthquake, United States (each fringe corresponds to a 2.8 cm radial displacement) [ZEB 99]. For a color version of this figure, see www.iste.co.uk/baghdadi/2.zip*

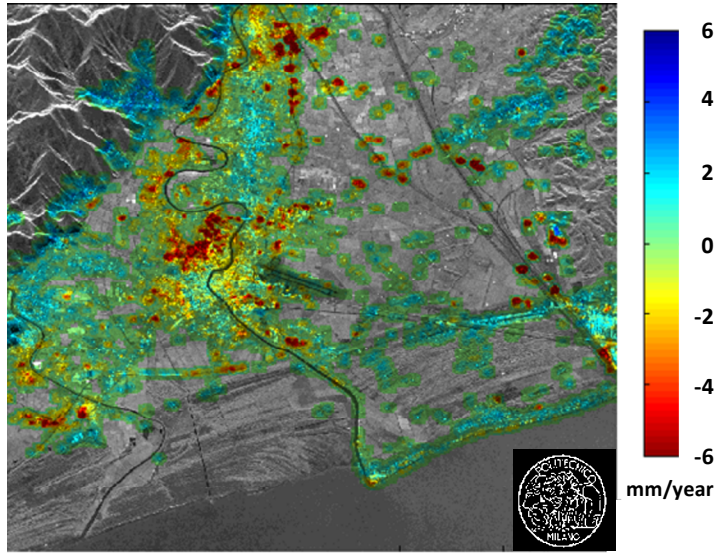

Figure 2.46. *Map of subsidence established over the city of Pisa, Italy, by means of 45 ERS images. Result made available by the SAR group of Politecnico di Milano, Italy. For a color version of this figure, see www.iste.co.uk/baghdadi/2.zip*

2.3.4. *SAR tomography*

SAR tomography is the generalization of SAR imaging to 3D focusing, which uses an azimuth and elevation bi-dimensional synthetic aperture combined with a 3D adapted filter. The configuration of a topographic measurement given in Figure 2.47 shows that, in practice, we use a set of N images, with $N \ll N_p$ and N_p the number of pulses acquired during a single measurement, measured in interferometric mode along parallel trajectories.

Those N images can also be coherently combined by means of the back-projection algorithm, for example, to synthesize an elevation aperture and to form a 3D image, whose elevation resolution is given, for a set of N images arranged as a uniform linear network, by $\delta z = \frac{h_{amb}}{N}$, with $h_{amb} = \frac{2\pi}{|dk_z|}$, and $dk_z = k_{z_{i+1}} - k_{z_i}$, proportional to the baseline difference of the two consecutive measurements of the elevation network. Since the vertical resolution is sometimes insufficient, techniques with better performances than the Fourier approach may be used, i.e. the adapted filter approach may

be used, in terms of resolution, at the expense of the SNR in general [GIN 05, GUI 05, HUA 11a, SAU 11]. For this, a covariance matrix $\mathbf{R} \in \mathbb{C}^{N\times N}$, is formed as $\mathbf{R}(i,j) = I\gamma_{ij}$, with:

$$\gamma_{ij} = \frac{\int f(z) e^{j(k_{z_j} - k_{z_i})z}\, dz}{\int f(z)\, dz} \qquad [2.82]$$

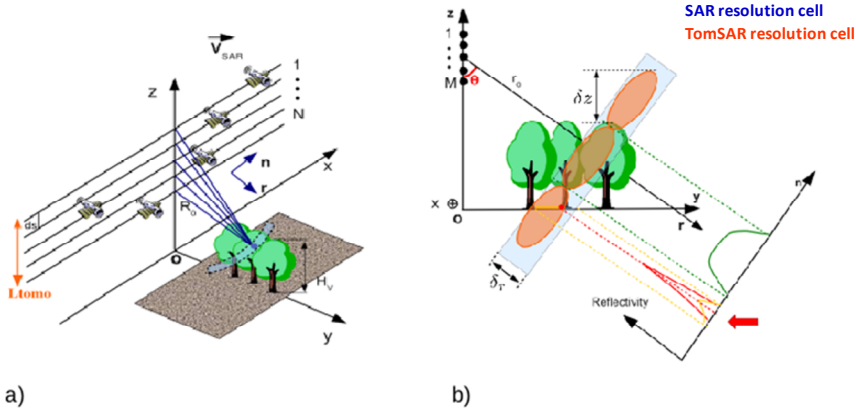

Figure 2.47. *a) Configuration of an N image tomographic SAR measurement; b) illustration of the resolving power over volume contributions in the vertical direction. For a color version of this figure, see www.iste.co.uk/baghdadi/2.zip*

The estimation of $f(z)$, the elevation reflectivity density, defined in [2.79], from $\mathbf{R}$ is similar to a spectral analysis problem for which there exists a large variety of solutions. A synopsis of the tomographic SAR processing chain is given in Figure 2.48.

The reflectivity profile estimated by tomography, $P(z) = \hat{f}(z)$, can then be used to estimate geophysical characteristics of the observed environments, directly or through 3D EM scattering models. Like in the case of interferometric data, that type of spatial approach can be combined with a polarization diversity, which allows us, as shown by the works in [TEB 09, TEB 10], to automatically separate the ground and volume responses, through the technique called Sum of Kronecker Products (SKP) decomposition. Following the pioneering work conducted in [REI 00], numerous SAR tomography applications were carried out, for which Figures 2.49–2.52 show arbitrarily sampled results.

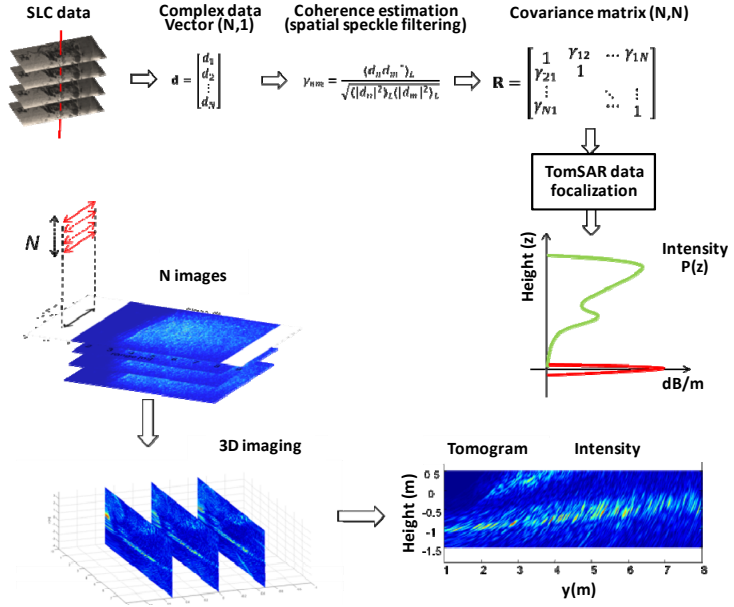

Figure 2.48. *Synopsis of the tomographic SAR processing chain using coherent N SAR images to estimate an elevation reflectivity profile P(z). Example of application on very high resolution tomographic SAR data of a snow cover. For a color version of this figure, see www.iste.co.uk/baghdadi/2.zip*

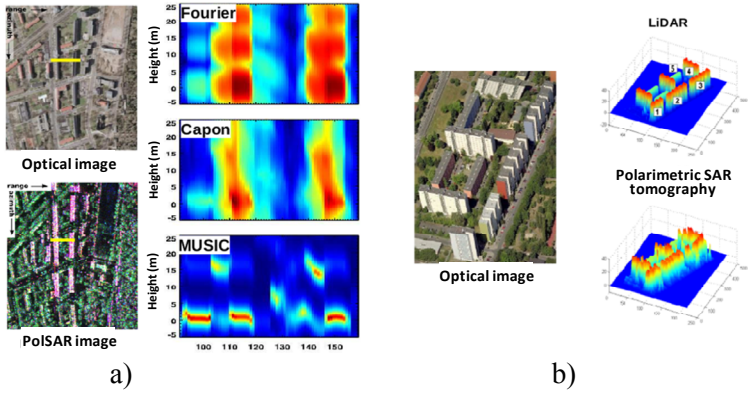

Figure 2.49. *3D reconstruction of the urban area of the city of Dresde, Germany, using intermediate resolution of the polarimetric SAR data in L-band for a minimum number of images (N=3) [HUA 09, FER 15]; a) illustration of the vertical resolution gain provided by some spectral analysis techniques; b) comparison of the results obtained on a group of buildings with a LiDAR profile. For a color version of this figure, see www.iste.co.uk/baghdadi/2.zip*

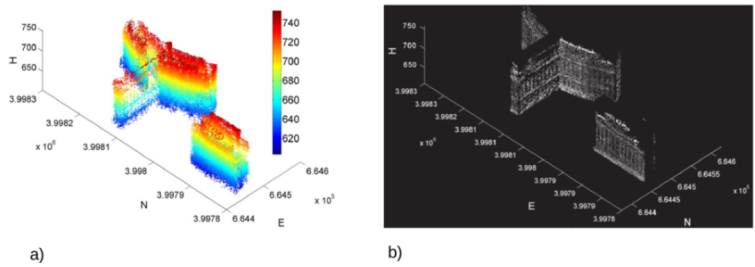

Figure 2.50. *Suggested 3D reconstruction [SHA 12] of a facade by means of two sets of very high resolution TerraSAR-X data each of 25 images: a) 3D position of the detected scatterers; b) 3D reconstruction of the intensity profile. For a color version of this figure, see www.iste.co.uk/baghdadi/2.zip*

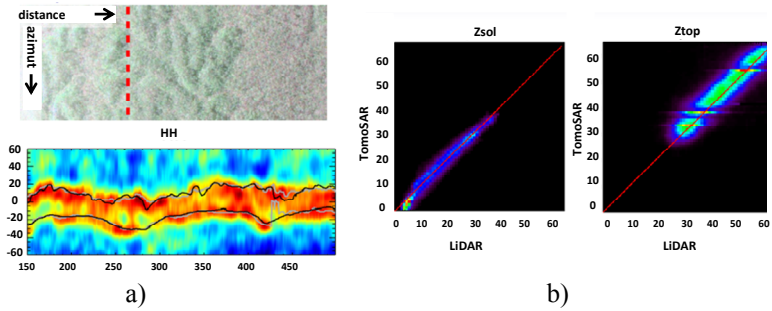

Figure 2.51. *Characterization of a tropical forest using polarimetric SAR tomography in P-band using ONERA/SETHI data [HUA 11b, FERRO 15]; a) PolSAR 2D image and tomographic profile reconstructed HH polarization; b) comparison of the tomographic and LiDAR estimates of the altitude of the tree tops (Ztop) and of the underlying ground height (Zground), on the whole site. For a color version of this figure, see www.iste.co.uk/baghdadi/2.zip*

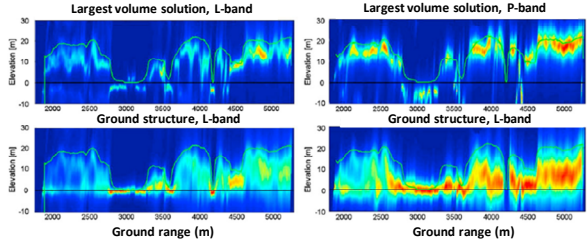

Figure 2.52. *Illustration of the SKP approximation capacity presented in [TEB 09, TEB 10, TEB 12] to separate the underlying ground and volume contributions through the analysis of PolTomSAR data. Case of an image of a boreal forest in the L and P-bands. Images made available by S. Tebaldini. For a color version of this figure, see www.iste.co.uk/baghdadi/2.zip*

2.4. Key points

The use of coherent diversity modes makes it possible to significantly increase the characterization capacities provided by classic SAR imaging. In fact, the 2D electromagnetic reflectivity of environments alone can seem limited to further characterize realistic objects with complex or volumetric structure. The two most used modes to improve SAR imaging performances implement a polarization diversity for the polarimetric mode, or a space diversity for interferometric imaging. Measuring the response of an object in a polarization basis gives information on some of its intrinsic geophysical properties, whereas interferometry allows us to measure the topography of environments, and its multi-acquisition version, or tomography, allows us to estimate the reflectivity of complex environments and to separate the contributions from scatterers located at different altitudes. The use of those diversity modes requires the extension of statistical representations and speckle filtering procedures to the case of N–D data, with $N = 2$ in inSAR, $N \geq 3$ for SAR tomography and $2 \leq N \leq 4$ for polarimetric measurements. The processing and the interpretation of those different types of data require signal processing procedures, specific to each mode, such as polarimetric decomposition, interferometric compensation or tomographic focusing techniques.

SAR polarimetry makes it possible to differentiate the environments observed according to their EM scattering mechanism, by estimating some of their key parameters, like their structure, orientation, moisture or roughness. Space borne SAR interferometry allows us to map the planet with a global accuracy never achieved before, and the use of a differential mode gives us access to the measurement of field displacements ranging from a few millimeters per year. SAR tomography aims to image semi-opaque complex volume environments and has resulted in significant progress in characterizing complex environments, whose study by means of 2D images is ill-conditioned. We note that those different diversity modes can be combined for a better characterization of environments, and that their implementation within the context of space borne measurement is either already operational, or under study for the tomographic mode.

2.5. Bibliography

[ALL 04] ALLAIN S., FERRO-FAMIL L., POTTIER E., "Two novel surface model based inversion algorithms using multi-frequency POLSAR data", *IEEE IGARSS '04,* vol. 2, pp. 823–826, 2004.

[ALL 05a] ALLAIN S., FERRO-FAMIL L., MARTINEZ C.L. *et al.*, "New eigenvalue-based parameter for natural media characterization", *Proceedings of the POLinSAR Workshop*, ESRIN, Frascati, Italy, ESA SP-586, 2005.

[ALL 05b] ALLAIN S., FERRO-FAMIL L., POTTIER E., "New eigenvalue-based parameters for natural media characterization", *European Radar Conference EuRAD*, Paris, France, 6–7 October 2005.

[AME 00] AMELUNG F., JONSSON S., ZEBKER H. *et al.*, "Widespread uplift and "trapdoor" faulting on Galapagos volcanoes observed with radar interferometry", *Nature*, vol. 407, pp. 993–996, 2000.

[ARI 10] ARII M., VAN ZYL J.J., KIM Y., "A general characterization for polarimetric scattering from vegetation canopies", *IEEE Transactions on Geoscience and Remote Sensing*, vol. 48, pp. 3349–3357, 2010.

[ARI 11] ARII M., VAN ZYL J.J., KIM Y., "Adaptive model-based decomposition of polarimetric SAR covariance matrices", *IEEE Transactions on Geoscience and Remote Sensing*, vol. 49, pp. 1104–1113, 2011.

[BAM 98] BAMLER R., HARTL P., "Synthetic aperture radar interferometry", *Inverse Problems*, vol. 14, pp. R1–R54, 1998.

[CHE 03] CHEN K.S., WU T.D., TSANG L. *et al.*, "Emission of rough surfaces calculated by the integral equation method with comparison to three-dimensional moment method simulations", *IEEE Transactions on Geoscience and Remote Sensing*, vol. 41, pp. 90–101, 2003.

[CLO 03] CLOUDE S.R., PAPATHANASSIOU K.P., "Three-stage inversion process for polarimetric SAR interferometry", *IEEE Proceedings of Radar Sonar Navigation*, vol. 150, no. 3, pp. 125–134, 2003.

[CLO 09] CLOUDE S.R., *Polarisation Applications in Remote Sensing*, Oxford University Press, 2009.

[CLO 86a] CLOUDE S.R., "Group theory and polarisation algebra", *OPTIK*, vol. 75, pp. 26–36, 1986.

[CLO 86b] CLOUDE S.R., Polarimetry: the characterization of polarization effects in EM scattering, PhD Thesis, University of Birmingham, 1986.

[CLO 92] CLOUDE S.R., "Lie groups in electromagnetic wave propagation and scattering", *Journal of Electromagnetic Waves and Applications*, vol. 6, no. 7, pp. 947–974, 1992.

[CLO 95] CLOUDE S.R., POTTIER E., "Concept of polarization entropy in optical scattering", *Optical Engineering*, vol. 34, pp. 1599–1610, 1995.

[CLO 96] CLOUDE S.R., POTTIER E., "A review of target decomposition theorems in radar polarimetry", *IEEE Transactions on Geoscience and Remote Sensing*, vol. 34, pp. 498–518, 1996.

[CLO 97] CLOUDE S.R., POTTIER E., "An entropy based classification scheme for land applications of polarimetric SAR", *IEEE Transactions on Geoscience and Remote Sensing*, vol. 35, pp. 68–78, 1997.

[CLO 98] CLOUDE S.R., PAPATHANASSIOU K.P., "Polarimetric SAR interferometry", *IEEE Transactions on Geoscience and Remote Sensing*, vol. 36, no. 5, pp. 1551–1565, 1998.

[DEL 15] DELEDALLE C.A., DENIS L., TUPIN F. *et al.*, "NL-SAR: a unified nonlocal framework for resolution-preserving (Pol)(In)SAR denoising", *IEEE Transactions on Geoscience and Remote Sensing*, vol. 53, pp. 2021–2038, 2015.

[DES 51] DESCHAMPS G.A., "Geometrical representation of the polarization of a plane electromagnetic wave", *Proceedings of IRE*, vol. 39, pp. 540–544, 1951.

[FER 00] FERRO-FAMIL L., POTTIER E., "Description of dual frequency polarimetric data using Gell-Mann parameter set", *Electronic Letters*, vol. 36, pp. 1646–1647, 2000.

[FER 01a] FERRETTI A., PRATI C., ROCCA F., "Permanent scatterers in SAR interferometry", *IEEE Transactions on Geoscience and Remote Sensing*, vol. 39, pp. 8–20, 2001.

[FER 01b] FERRO-FAMIL L., POTTIER E., LEE J.S., "Unsupervised classification of multifrequency and fully polarimetric SAR images based on the H/A/Alpha-Wishart classifier", *IEEE Transactions on Geoscience and Remote Sensing,* vol. 39, pp. 2332–2342, 2001.

[FER 03] FERRO-FAMIL L., POTTIER E., LEE J.S., "Unsupervised classification of natural scenes form polarimetric interferometric SAR data", in CHEN C.H. (ed.), *Frontiers of Remote Sensing Information Processing*, World Scientific Publishing, 2003.

[FER 07] FERRETTI A., MONTI-GUARNIERI A., PRATI C. *et al.*, "InSAR principles: guidelines for SAR interferometry processing and interpretation", Report, ESA Publications ESTEC, TM-19, 2007.

[FER 15] FERRO-FAMIL L., HUANG Y., POTTIER E., "Principles and Applications of Polarimetric SAR Tomography for the Characterization of Complex Environments", in SANSO F. (ed.), *International Association of Geodesy Symposia*, Springer-Verlag, 2015.

[FRE 07] FREEMAN A., "Fitting a two-component scattering model to polarimetric SAR data from forests", *IEEE Transactions on Geoscience and Remote Sensing,* vol. 45, pp. 2583–2592, 2007.

[FRE 98] FREEMAN A., DURDEN S.L., "A three-component scattering model for polarimetric SAR data", *IEEE Transactions on Geoscience and Remote Sensing,* vol. 36, pp. 963–973, 1998.

[FUN 94] FUNG A.K., "Microwave scattering and emission models and their applications", *Artech House Remote Sensing Library*, Artech House, 1994.

[GAB 89] GABRIEL A.K., GOLDSTEIN R.M., ZEBKER H.A., "Mapping small elevation changes over large areas: differential radar interferometry", *Journal of Geophysical Research*, vol. 94, pp. 9183–9191, 1989.

[GIN 05] GINI F., LOMBARDINI F., "Multibaseline cross-track SAR interferometry: a signal processing perspective", *IEEE Aerospace and Electronic System Magazine*, vol. 20, pp. 71–93, 2005.

[GOL 88] GOLDSTEIN R.M., ZEBKER H.A., WERNER C.L., "Satellite radar interferometry endash – Two-dimensional phase unwrapping", *Radio Science*, vol. 23, pp. 713–720, 1988.

[GOO 76] GOODMAN J.W., "Some fundamental properties of speckle", *Journal of Optical Society of America*, vol. 66, no. 11, pp. 1145–1150, 1976.

[GRA 74] GRAHAM L.C., "Synthetic interferometer radar for topographic mapping" *Proceedings of IEEE*, vol. 62, no. 6, pp. 763–768, 1974.

[GUI 05] GUILLASO S., FERRO-FAMIL L., REIGBER A. *et al.*, "Building characterization using L-band polarimetric interferometric SAR data", *IEEE Geoscience and Remote Sensing Letters*, vol. 2, pp. 347–351, 2005.

[HAJ 03] HAJNSEK I., POTTIER E., CLOUDE S.R., "Inversion of surface parameters from polarimetric SAR", *IEEE Transactions on Geoscience and Remote Sensing,* vol. 41, pp. 727–744, 2003.

[HUA 09] HUANG Y., FERRO-FAMIL L., "3D characterization of buildings in a dense urban environment using L-band POL-inSAR data with irregular baselines", *IEEE IGARSS '09,* vol. 3, pp. 111–129, 2009.

[HUA 11a] HUANG Y., FERRO-FAMIL L., REIGBER A., "Under-foliage object imaging using SAR tomography and polarimetric spectral estimators", *IEEE Transactions on Geoscience and Remote Sensing*, vol. 50, no. 6, pp. 2213–2225, 2011.

[HUA 11b] HUANG Y., FERRO-FAMIL L., LARDEUX C., "Polarimetric SAR tomography of tropical forest at P-band ", *Proceedings of IGARSS*, Vancouver, Canada, pp. 1373–1376, July 2011.

[HUY 70] HUYNEN J.R., Phenomenological theory of radar targets, PhD Thesis, Drukkerij Bronder-Offset N.V., Rotterdam, 1970.

[KEN 49] KENNAUGH E.M., "Effects of the Type of Polarization on Echo Characteristics", Report 381-1 to 394-24, Ohio State University, Antenna Laboratory, Columbus, OH, 1949.

[KNO 74] KNOTT E., SENIOR T., "The far field criterion", *Antennas and Propagation Society International Symposium*, pp. 92–93, 1974.

[KOS 86] KOSTINSKI A., BOERNER W., "On foundations of radar polarimetry", *IEEE Transactions on Antennas Propagation*, vol. 34, pp. 1395–1404, 1986.

[LEE 94a] LEE J.S., HOPPEL K.W., MANGO S.A. *et al.*, "Intensity and phase statistics of multilookpolarimetric and interferometric SAR imagery", *IEEE Transactions on Geoscience and Remote Sensing*, vol. 32, pp. 1017–1028, 1994.

[LEE 94b] LEE J.S., JURKEVICH L., DEWAELE P. *et al.*, "Speckle filtering of SAR images: a review", *Remote Sensing Reviews*, vol. 8, no.4, pp. 313–340, 1994.

[LEE 98] LEE J.S., JANSEN R.W., SCHULER D.L. *et al.*, "Polarimetric analysis and modeling of multifrequency SAR signatures from Gulf Stream fronts", *IEEE Journal of Oceanic Engineering*, vol. 23, pp. 322–333, 1998.

[LEE 99] LEE J.S., GRUNES M.R., DE GRANDI G., "Polarimetric SAR speckle filtering and its implication for classification", *IEEE Transactions on Geoscience and Remote Sensing,* vol. 37, pp. 2363–2373, 1999.

[LEE 01] LEE J.S., GRUNES M.R., POTTIER E.*et al.*, "Segmentation of polarimetric SAR images", *IEEE IGARSS '01*, pp. 414–416, 2001.

[LEE 02a] LEE J.S., GRUNES M.R., POTTIER E. *et al.*, "Segmentation of polarimetric SAR images that preserves scattering mechanisms", *4th European Conference on Synthetic Aperture Radar*, EUSAR 2002, Jun 2002, Köln, Germany, 2002.

[LEE 02b] LEE J.S., SCHULER D.L., AINSWORTH T.L. *et al.*, "On the estimation of radar polarization orientation shifts induced by terrain slopes", *IEEE Transactions on Geoscience and Remote Sensing*, vol. 40, pp. 30–41, 2002.

[LEE 04] LEE J.S., GRUNES M.R., POTTIER E. *et al.*, "Unsupervised terrain classification preserving polarimetric scattering characteristics", *IEEE Transactions on Geoscience and Remote Sensing*, vol. 42, pp. 722–731, 2004.

[LEE 06] LEE J.S., GRUNES M.R., SCHULER D.L. *et al.*, "Scattering-model-based speckle filtering of polarimetric SAR data", *IEEE Transactions on Geoscience and Remote Sensing*, vol. 44, pp. 176–187, 2006.

[LEE 08] LEE J.S., POTTIER E., *Polarimetric Radar Imaging: From Basics to Applications*, CRC Press, 2008.

[LOP 92] LOPES A., GOZE S., NEZRY E., "Polarimetric speckle filters for SAR data", *IEEE IGARSS '92*, pp. 80–82, 1992.

[LOP 97] LOPES A., SERY F., "Optimal speckle reduction for the product model in multilookpolarimetric SAR imagery and the Wishart distribution", *IEEE Transactions on Geoscience and Remote Sensing*, vol. 35, pp. 632–647, 1997.

[LUE 95] LUENEBURG E., "Principles of radar polarimetry", *Proceedings of the IEICE Transitions on the Electronic Theory*, vol. E78-C, no. 10, pp. 1339–1345, 1995.

[LUE 96] LUENEBURG E., "Polarimetry: a revision of basic concepts", in CLOUDE SR., SERBEST A.H. (eds), *Direct and Inverse Electromagnetic Scattering*, Longman Scientific and Technical, 1996.

[MAS 93] MASSONNET D., ROSSI M., CARMONA C. *et al.*, "The displacement field of the Landers Earthquake mapped by radar interferometry", *Nature*, vol. 364, pp. 138–142, 1993.

[MAS 95] MASSONNET D., BRIOLE P., ARNAUD A., "Deflation of Mount Etna monitored by spaceborne radar interferometry", *Nature*, vol. 375, pp. 567–570, 1995.

[NAN 09] NANNINI M., SCHEIBER R., MOREIRA A., "Estimation of the minimum number of tracks for SAR tomography", *IEEE Transactions on Geoscience and Remote Sensing*, vol. 47, no. 2, pp. 531–543, 2009.

[NEU 09] NEUMANN M., FERRO-FAMIL L., REIGBER A., "Estimation of forest structure, ground, and canopy layer characteristics from multibaseline polarimetric interferometric SAR data", *IEEE Transactions on Geoscience and Remote Sensing*, vol. 48, pp. 1086–1104, 2009.

[NGH 92] NGHIEM S.V., YUEH S.H., KWOK R. *et al.*, "Symmetry properties in polarimetric remote sensing", *Radio Science*, vol. 27, pp. 693–711, 1992.

[PAL 12] PALADINI R., FERRO-FAMIL L., POTTIER E. *et al.*, "Lossless and sufficient Psi-invariant decomposition of random reciprocal target", *IEEE Transactions on Geoscience and Remote Sensing*, vol. 50, no. 9, pp. 3487–3501, 2012.

[PAP 01] PAPATHANASSIOU K.P., CLOUDE S.R., "Single-baseline polarimetric SAR interferometry", *IEEE Transactions on Geoscience and Remote Sensing*, vol. 39, pp. 2352–2363, 2001.

[REI 00] REIGBER A., MOREIRA A., "First demonstration of airborne SAR tomography using multibaseline L-band data", *IEEE Transactions on Geoscience and Remote Sensing*, vol. 38, pp. 2142–2152, 2000.

[REI 01] REIGBER A., Airborne SAR Tomography, PhD Thesis, University of Stuttgart, Germany.

[SAU 11] SAUER S., FERRO-FAMIL L., REIGBER A. *et al.*, "Three-dimensional imaging and scattering mechanism estimation over urban scenes using dual-baseline polarimetricInSAR observations at L-Band", *IEEE Transactions on Geoscience and Remote Sensing*, vol. 49, pp. 4616–4629, 2011.

[SHA 12] SHAHZAD M., ZHU X., BAMLER R., "Façade structure reconstruction using spaceborne TomoSAR point clouds", *IGARSS*, Munich, Germany, July 2012.

[SIN 50] SINCLAIR G., "The transmission and reception of elliptically polarized waves", *Proceedings of IRE*, vol. 38, pp. 148–151, 1950.

[SIN 48] SINCLAIR G., Modification of the radar target equation for arbitrary targets and arbitrary polarization, Report 302-19, Antenna Laboratory, The Ohio State University Research Foundation, 1948.

[TEB 09] TEBALDINI S., "Algebraic synthesis of forest scenarios from multibaseline PolInSAR data", *IEEE Transactions on Geoscience and Remote Sensing,* vol. 47, pp. 4132 –4142, 2009.

[TEB 10] TEBALDINI S., "Single and multipolarimetric SAR tomography of forested areas: a parametric approach", *IEEE Transactions on Geoscience and Remote Sensing,* vol. 48, pp. 2375–2387, 2010.

[TEB 12] TEBALDINI S., ROCCA F., "Multibaseline Polarimetric SAR tomography of a Boreal forest at P- and L-bands", *IEEE Transactions on Geoscience and Remote Sensing*, vol. 50, pp. 232–246, 2012.

[TOU 02] TOUZI R., "A review of speckle filtering in the context of estimation theory", *IEEE Transactions on Geoscience and Remote Sensing*, vol. 40, pp. 2392–2404, 2002.

[TRE 00] TREUHAFT R.N., SIQUEIRA P.R., "Vertical structure of vegetated land surfaces from interferometric and polarimetric radar", *Radio Science*, vol. 35, pp. 141–178, 2000.

[TRE 99] TREUHAFT R.N., CLOUDE S.R., "The structure of oriented vegetation from polarimetric interferometry", *IEEE Transactions on Geoscience and Remote Sensing*, vol. 37, pp. 2620–2624, 1999.

[VAN 11] VAN ZYL J.J., ARII M., KIM Y., "Model-based decomposition of polarimetric SAR covariance matrices constrained for nonnegative Eigenvalues", *IEEE Transactions on Geoscience and Remote Sensing*, vol. 49, pp. 3452–3459, 2011.

[VAS 06] VASILE G., TROUVE E., LEE J.S. *et al.*, "Intensity-driven adaptive-neighborhood technique for polarimetric and interferometric SAR parameters estimation". *IEEE Transactions on Geoscience and Remote Sensing*, vol. 44, pp. 1609–1621, 2006.

[YAM 05] YAMAGUCHI Y., MORIYAMA T., ISHIDO M. *et al.*, "Four-component scattering model for polarimetric SAR image decomposition", *IEEE Transactions on Geoscience and Remote Sensing,* vol. 43, pp. 1699–1706, 2005.

[YUE 94] YUEH S.H., KWOK R., NGHIEM S.V., "Polarimetric scattering and emission properties of targets with reflection symmetry", *Radio Science,* vol. 29, pp. 1409–1420, 1994.

[ZEB 86] ZEBKER H.A., GOLDSTEIN R.M., "Topographic mapping from interferometric synthetic aperture radar observations", *Journal of Geophysical Research Solid Earth*, vol. 91, pp. 4993–4999, 1986.

[ZEB 94] ZEBKER H.A., ROSEN P.A., GOLDSTEIN R.M. *et al.*, "On the derivation of coseismic displacement fields using differential radar interferometry: The Landers earthquake", *Journal of Geophysical Research*, vol. 99, pp. 19617–19634, 1994.

[ZEB 99] ZEBKER H.A., SEGALL P., AMELUNG F. *et al.*, "Slip distribution of the Hector Mine earthquake inferred from interferometric radar", A*merican Geophysical Union (AGU) Fall Meeting*, San Francisco, December 13–17, 1999.